Silicon Electrolyte Interface Stabilization (SEISta)

Final Progress Report FY19

Anthony Burrell
National Renewable Energy Laboratory
15013 Denver West Parkway
Golden, CO 80401
Phone: (303) 384-6666
E-mail: anthony.burrell@nrel.gov

Brian Cunningham, DOE-EERE-VTO Program Manager
Hybrid Electric Systems, Battery R&D
Phone: (202) 586-8055
E-mail: brian.cunningham@ee.doe.gov

Table of Contents

Project Introduction

This report documents the Silicon Electrolyte Interface Stabilization team's approach in 1) characterizing the early-stage silicon solid-electrolyte interphase (SEI) including progress on identifying the specific reaction pathways present in the formation of the SEI layer, and 2) establishing a procedure for measuring SEI growth rate at fixed potentials and different cycling regimes.

Silicon is a viable alternative to graphitic carbon as an electrode in lithium-ion cells and can theoretically store >3,500 mAh/g. However, lifetime problems have been observed that severely limit its use in practical systems. The major issues appear to involve the stability of the electrolyte and the uncertainty associated with the formation of a stable SEI at the electrode. Recently, calendar-life studies have indicated that the SEI may not be stable even under conditions where the cell is supposedly static. Clearly, a more foundational understanding of the nature of the silicon/electrolyte interface is required if we are to solve these complex stability issues. A new multi-lab consortium has been formed to address a critical barrier in implementing a new class of materials used in lithium-ion batteries that will allow for smaller, cheaper, and better-performing batteries for electric-drive vehicles. This consortium, named the Silicon Electrolyte Interface Stabilization (SEISta) project, was formed to focus on overcoming the barrier to using such anode materials. Five national laboratories are involved: the National Renewable Energy Laboratory (NREL), Argonne National Laboratory (ANL), Lawrence Berkeley National Laboratory (LBNL), Oak Ridge National Laboratory (ORNL), and Sandia National Laboratories (SNL).

The SEISta project was specifically developed to tackle the foundational understanding of the formation and evolution of the solid-electrolyte interphase on silicon. This project will have as its primary goal an understanding of the reactivity of the silicon and lithiated silicon interface with the electrolyte in lithium-ion systems. It consists of researchers from NREL, ANL, LBNL, ORNL, and SNL working toward clear unified goals. The Silicon Deep-Dive team, which focuses on the science and technology barriers in functional electrodes, is a critical partner in this work. Many of the researchers are shared between both teams, and we hold joint meetings to ensure effective communication between the teams.

The current goals of SEISta are:

Quarter 1 Milestone: Have determined if the pristine surface of the silicon influences the composition and the function of the SEI after 1, 10, and 50 cycles (XPS, SIMS, IR, Raman, STEM, SSRM). (100% complete)

Quarter 2 Milestone: Have determined that the nature of the silicon surface can affect the composition, function, and thickness of the SEI. (100% complete)

Quarter 3 Milestone: Have determined how water concentration (as a function of water content up to 100 ppm) in the electrolyte affects SEI thickness and composition (electrochemistry, spectroscopy, impedance) of the SEI formed at 1.5, 1.0, 0.7, 0.4, 0.15, and 0.05 V vs Li/Li+. (100% complete)

Quarter 4 Milestone: Have determined the nature of the soluble SEI components that are formed over 10 cycles and that are soluble in the Gen 2 electrolyte. (100% complete)

Approach

The SEISta team works to ensure that protocols for sample preparation, experimental design, and implementation as well as data reporting are consistent across the whole team. Each laboratory is working toward the same set of quarterly milestones using its own specific talents and capabilities in a concerted effort with the other team members. This joint focus results in multiple researchers interacting to produce and analyze data to ensure that individual experimental variations will not lead to erroneous results. Critical to the success of this effort is the use of standard samples that can be shared by all parties. In addition to weekly whole-team video presentations, we have held on-site face-to-face meetings each quarter for all team members and other interested parties to brainstorm and sort out issues with existing experiments and jointly develop new experimental plans.

Objectives

The critical issues that SEISta is attempting to address are:

- What are the properties of the lithiated silicon/electrolyte interface?
- What is the silicon SEI actually made of and what reactions are contributing to it?
- How fast does the silicon SEI grow?

- Does it stop growing?
- Is it soluble?
- Can it be stabilized?

For FY19, the team continues to focus on three broad tasks:

Materials Standardization—This task is critical to developing and deploying standardized samples and experimental procedures across the team. We will continue to provide full characterization to any new sample that is to be used for SEI studies to ensure reproducibility and full understanding of the material. This quarter's work focused on developing new oxide coatings and methods to control the thickness and density of oxide samples. In addition, work on the silicon nanoparticles has made progress with the enhancement of the materials collection and handling system in the plasma reactor. *Although this work dominated the early part of the project and is still critical to its success, it is now only a minor part of the work, and this is reflected in the relative balance of this quarterly report.*

Model Materials Development and Characterization—The nature of the electrode-electrolyte interaction in silicon electrodes is at the heart of the formation and stability of the SEI. The synthesis of well-defined silicon nanoparticles and the different chemical markups of lithiated silicon surfaces is being probed by preparing model compounds and thin films that may/can exist in silicon anodes. Lithium silicides, silicates, and other inorganic material (LiF, Li_2O) are being prepared, and their reactivity with electrolytes is being determined. These materials also act as standard spectroscopy samples for the researchers who are looking at the formation of the SEI on different silicon materials.

SEI Characterization—The overall objective for SEISta is to understand the nature and evolution of the SEI on silicon anodes. The materials standardization and model compounds will enable the researchers to systematically investigate the formation of the solid-electrode interphase using a wide variety of spectroscopy techniques—from different optical, microscopy, and electrochemistry—to determine how the SEI forms based on the nature of the silicon surface, and how it evolves over time. This section of work will continue to grow in scope as we move beyond the sample-characterization phase of the project and toward understanding the nature and evolution of the SEI. *This part of the project now represents the bulk of the work and, as such, this quarterly report is largely reporting on work leading to this outcome.*

SEISta Milestones FY18: Silicon Electrolyte Interface Stabilization (SEISta)

SEISta Team

Background

The overall objective of the SEISta project is to better understand the formation and evolution of the solid-electrolyte interphase (SEI) on silicon anodes. Silicon is a viable alternative to graphitic carbon as an electrode in lithium-ion cells and can theoretically store >3,500 mAh/g. However, lifetime problems have been observed that severely limit its use in practical systems. The major issues appear to involve the stability of the electrolyte and the uncertainty associated with the formation of a stable SEI at the electrode. Recently, calendar-life studies have indicated that the SEI may not be stable even under conditions where the cell is supposedly static. Clearly, a more foundational understanding of the nature of the silicon/electrolyte interface is required if we are to solve these complex stability issues. A multi-lab consortium has been formed to address a critical barrier in implementing a new class of materials used in lithium-ion batteries that will allow for smaller, cheaper, and better performing batteries for electric-drive vehicles. This consortium—the Silicon Electrolyte Interface Stabilization (SEISta) project—was formed to focus on overcoming the barrier to using such anode materials. Five national laboratories, led by the National Renewable Energy Laboratory (NREL), are involved: NREL, as well as Argonne (ANL), Lawrence Berkeley (LBNL), Oak Ridge (ORNL), and Sandia National Laboratories (SNL).

Quarter 1 Milestone:

- Have determined if the pristine surface of the silicon influences the composition and the function of the SEI after 1, 10, and 50 cycles (XPS, SIMS, IR, Raman, STEM, SSRM). (100% complete)

Quarter 2 Milestone:

- Have determined that the nature of the silicon surface can affect the composition, function, and thickness of the SEI. (100% complete)

Quarter 3 Milestone:

- Have determined how water concentration (as a function of water content up to 100 ppm) in the electrolyte affects SEI thickness and composition (electrochemistry, spectroscopy, impedance) of the SEI formed at 1.5, 1.0, 0.7, 0.4, 0.15, and 0.05 V vs Li/Li+. (100% complete)

Quarter 4 Milestone

- Have determined the nature of the soluble SEI components that are formed over 10 cycles and that are soluble in the Gen 2 electrolyte. (100% complete)

Results

For FY19 all milestones are 100% complete.

Part 1: Studies of SiO_2 Interfaces

Kristin Persson (LBNL), Manuel Schnabel (NREL), Chunmei Ban (NREL), Steve Harvey (NREL), Glenn Teeter (NREL), Paul Stradins (NREL), Zhifei Li (NREL), Andriy Zakutayev (NREL), Jaclyn Coyle (NREL), Kyle Fenton (SNL), Josey McBrayer (SNL), Chris Apblett (SNL), Mike Carroll (NREL), Fernando Urias NREL), Greg Pach (NREL), Nathan Neale (NREL), Gabriel Veith (ORNL), Brenda Smith (ORNL), Rebecca McAuliffe (ORNL), Eric Allcorn (SNL), Jill Langendorf (SNL), Teal Harbour (SNL), Yeyoung Ha (NREL), Caleb Stetson (NREL), Andrew Norman (NREL), Bertrand Tremolet de Villers (NREL) Mowafak Al-Jassim (NREL), Sang-Don Han (NREL), Binghong Han (ANL), Baris Key (ANL), Jack Vaughey (ANL)

Background

A central objective of the SEISta project is to understand the what role the surface SiO_2 layers on silicon have on the electrochemical cycling properties of composite electrodes. This includes how the early- and late-stage SEI is affected by the presence of SiO_2. Oxygen is almost inevitable in the Si anode where the surface of Si forms a native oxide layer when it is exposed to air. In addition, different preparation processes of Si anodes may lead to different levels of oxygen content, not only on the surface but also through the bulk. Previously, the SEISta consortium has identified the native SiO_2 as playing a major role in the surface behavior and passivation of the silicon anode. Experiments have shown non-passivating behavior and corrosion current at high voltages, well above the predicted lithiation of SiO_2 and Si.

We consider three different types of surfaces in our studies of SiO_2 on Si. First, polished silicon wafers, either directly or as a substrate for physically deposited thin films of Si, provide the most controlled silicon material with which to study the fundamental processes occurring during the lithiation of silicon from an electrolyte. In addition, they can be oxidized, resulting in dense SiO_2 layers of varying thickness whose effect on lithiation and battery electrochemistry can be studied as a model system. This includes simulations targeted at the stability of the SEI and the amorphous SiO_2 native oxide layer, and they elucidate the impact of the confining effects of a film, versus the bulk, on the lithiation behavior of the native oxide.

Second, entirely air-free routes for producing Si nanoparticles (NP) allows for the jump from the flat-surface model system to something more akin to a three-dimensional coated electrode that would ultimately be the basis for a new anode. These include synthesized particles of Si and SiO_x, because different levels of oxygen in the Si anode could affect the surface SEI formation, reversible capacity, and overall electrochemical performance. So far, most of the studies regarding the impacts of oxygen on the Si anode have focused on either the native oxide layer or the thermally grown thin SiO_2. Particles are synthesized from the gas phase, allowing the tuning of the composition of the surface from SiH_X-terminated to SiO_2-terminated, as well as particle size. Alternatively, a route to oxygen-free particle synthesis was studied by using an inert grinding method to produce particles from ingots of oxygen-free starting material. Finally, because of the recognition of the role of oxygen during either the synthesis or subsequent exposure, a series of SiO_x anodes with different oxygen levels were investigated to understand the impacts of oxygen on the SEI formation and overall electrochemical performance of the obtained SiO_x anodes.

Because of the existence of surface oxides and their role in changing the electronic density of states within the Si structure, there is concern that SEI formation will ultimately always be affected by the presence of oxygen and that oxygen can never truly be removed. One possible way to mitigate this effect of oxygen is by the addition of another species during the lithiation that can lead to formation of stabilizing phases within the SEI formation cycle. Recently, Key et al. demonstrated that adding 0.1 M $M(TFSI)_x$ (M = Mg, Zn, Al, and Ca) as an additive salt into the Gen2 electrolyte (1.2 M $LiPF_6$ in ethylene carbonate (EC):ethyl methyl carbonate (EMC) (3:7, wt%) + 10 wt% fluorinated ethylene carbonate (FEC)) stabilizes the Si anode chemistry through the *in situ* formation of Li−M−Si ternary phases during the charging process (lithiation into the Si anode) [1]. Such ternary Zintl phases, which are presumably formed on the Si surface, are more stable than the lithiated Si species, and hence, they demonstrate improved electrochemical performance with the possibly stabilized SEI. This program has characterized the formed SEI ternary Zintl phases, using a variety of analytical techniques (e.g., XPS, FTIR/Raman, STEM-EDS, and AFM/SSRM) to better understand the voltage- and time-dependent formation and the chemical and physical nature of the Li-Mg-Si ternary phase incorporated into the silicon anode.

As in any electrochemical system, the impact of the electrolyte and its interplay with the surface introduces complexity into the understanding of the formation of interface. This is particularly true in Si/ SiO_2 interfaces, where SEISta has previously shown that decomposition products from the electrolyte may generate species that attack the SEI at various points in the lithiation/delithiation process. Removing the impact of the liquid phase from the study requires a vacuum-phase lithium source to study the impact of just the introduction of Li to the SiO_2/Si interface without any intervening solvent or salt species. We continued the development of this virtual-electrode (VE) approach [2] for studying fundamental interfacial processes during silicon lithiation. Experiments were performed on 5-nm SiO_2/Si(001) wafer model-system anode samples to address key questions relating to how (electro)chemical evolution of inorganic phases in the solid-electrolyte interphase (SEI) affects the lithiation overpotential. Specifically, experiments were performed to determine how overpotential evolves as surface silicon oxides are converted to silicate phases according to $SiO_x + yLi^+ + ye^- \rightarrow Li_ySiO_x$.

To probe these phenomena, we developed a VE technique analogous to the galvanostatic intermittent titration technique (GITT). In the VE approach to GITT, a square-wave pulse is applied to the low-energy Li+ ion gun during *in situ* lithiation, while composition and chemical states are monitored with X-ray photoelectron spectroscopy (XPS). The *in situ* lithiation XPS measurements were performed using a Phi 5600 instrument equipped with a low-energy Li+ ion gun. For these experiments, the Li+ incident energy was set to 10 eV, and typical beam current densities were set in the range ~50–200 nA/cm^2.

Taken together, these studies of virtual electrode, model electrode, and particle electrode studies, combined with electrochemical, spectroscopic, and computational analysis, increases our understanding of the phenomena that are occurring during the initial SEI formation phases of Si anode. And they suggest pathways, such as the Zintl phase formation, that may help to stem the worst of these effects.

Results

Simulations of Stability Studies on Li Insertion into SiO_2

Previous work in SEISta investigated the thermodynamics of the Li-Si-O chemical system, finding that lithiation of bulk SiO_2 is thermodynamically preferred. This lithiation was found to occur at a potential of ~1.5V vs Li/Li+. Based on this result, the program started investigating the lithiation of SiO_2 films because the introduction of surface, interfacial, and confinement effects can impact the relative stability of various silicates and silicides. First, we studied the relative stability of the amorphous (herein denoted "a-") SiO_2 on crystalline (denoted as "c-") Si (a-SiO_2/c-Si) and c-SiO_2/c-Si film interfaces. Within the c-SiO_2/c-Si system, we identified two possible low-strain epitaxial matches between SiO_2 and Si: i) SiO_2 (001) and Si (111), and ii) SiO_2 (110) and Si(100). Epitaxial matches were found using the algorithm described by Zur et al. [3]. Using our recently developed interface builder tool in pymatgen, we constructed SiO_2/Si interfaces of varying oxide thickness for density functional theory (DFT) calculations. When building the epitaxial interfaces, both the film and substrate lattices were equally distorted to accommodate the lattice mismatch. We note, however, that for a real system, where the substrate is much thicker than the film, the strain is likely to be localized to the film. Figure 1 shows the energy per atom as a function of the thickness for both low-strain epitaxial matches. We find that the lowest-energy interface is the SiO_2(001) and Si(111), a reassuring result, given that the Si(111) surface is the most stable facet.

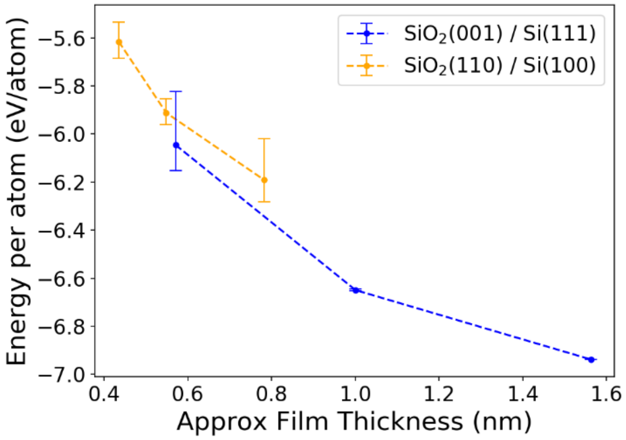

Figure 1. Energy per atom of two relaxed crystalline interfaces between i) SiO_2 (001) and Si (111), and ii) SiO_2 (110) and Si (100) as a function of SiO_2 film thickness.

Given that the native SiO_2 is well known to be amorphous, we also generate amorphous SiO_2 films and amorphous SiO_2/Si interfaces with varying SiO_2 film thicknesses and compare the energies with the crystalline films. Similar to the results found by Aykol et al. [4], we find an amorphous film to be preferred for thin films, with a crystalline film preferred when > 0.3 nm, as seen in Figure 2. Most native SiO_2 is amorphous for thicknesses much greater than 0.3 nm; thus, we conclude that the formation of a crystalline native oxide is a kinetically hindered process. However, we assert that the choice to divide the strain between the film and substrate will decrease the stability of the crystalline film, likely increasing the 0.3-nm value, although this is currently being reinvestigated.

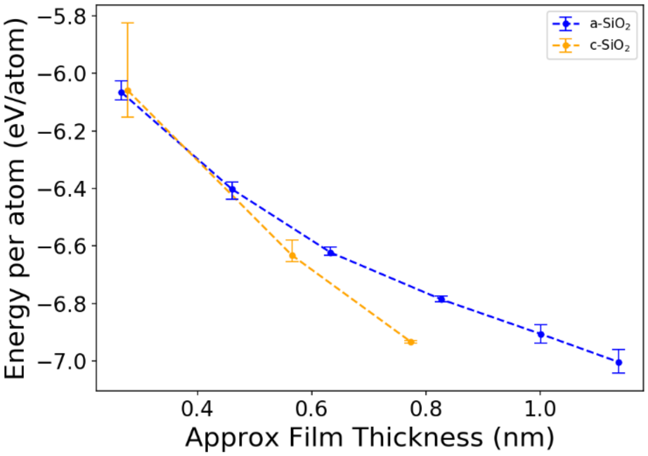

Figure 2. Energy per atom of interfaces between i) amorphous SiO_2 and ii) crystalline SiO_2 (001) with Si (111).

We have also investigated the thermodynamics for lithiation of a SiO_2 film toward understanding the role of the SiO_2 layer. We looked at the generation of lithium silicate/silicon interfaces through epitaxial matches. The crystalline lithium silicates, however, due to the complexity and large unit cells, form limited epitaxial matches with Si, with existing matches having surface areas of > 500 Å. Such an interface would require in excess of

500 atoms and is not reasonably simulated by DFT. An amorphous interface is, however, accessible through current computational methods and is our current research direction.

As a precursor to the much more expensive amorphous interface calculations, we first studied a-Li_xSi and a-Li_xSiO_y slabs independently to eliminate interfacial effects, focusing on only the energy change due to confinement and presence of a surface. We generate amorphous slabs by adding 20 Å of vacuum sputter material to the bulk amorphous structures previously obtained through a melt-quench method. The slabs are then annealed at 500 K with ab initio molecular dynamics (AIMD) for 2 ps to allow for surface relaxation and reconstruction. Energies are calculated following a DFT-based conjugate-gradient structure optimization. Thinner films are obtained by removal of an integer multiple of the film stoichiometry. Five samples of each film are obtained using five different starting amorphous structures.

As shown in Figure 3, the films are found to be greater in energy than their bulk counterparts, with energy decreasing as thickness increases, approaching the bulk value. The largest effects on the film energies are observed for small thicknesses, where the number of surface atoms dominates over the internal atoms. The film energies are found to follow the equation below:

$$E_{slab}(x) = E_{bulk} + \frac{2\sigma}{\rho x}$$

where E_{slab} and E_{bulk} are the energy per atom in the slab and bulk, respectively. x is the thickness of the film in Å, σ is the surface energy in units of $eV/\text{Å}^2$, and ρ is the atomic density in units of $atoms/\text{Å}^3$.

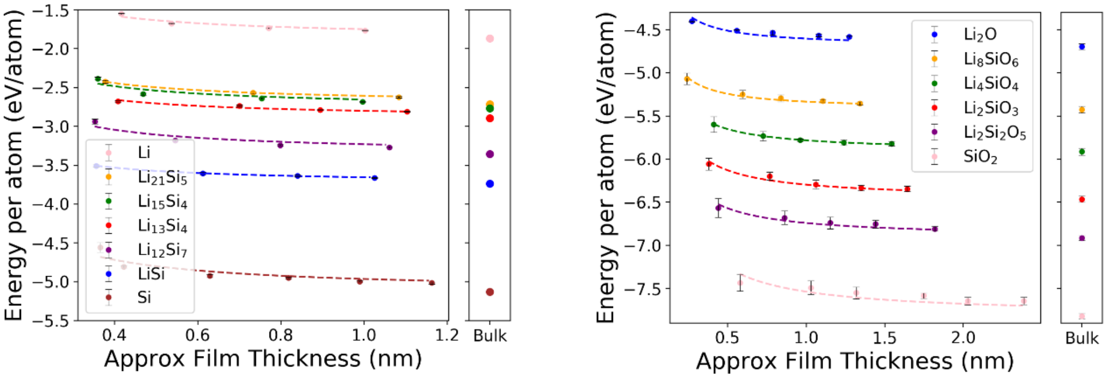

Figure 3. Energy per atom of slabs of a) Li_xSi and b) Li_xSiO_y as a function of thickness, with the bulk energies shown to the right. Error bars shown represent 1 standard deviation among five sample slabs. The dotted lines show the regression for energy vs thickness.

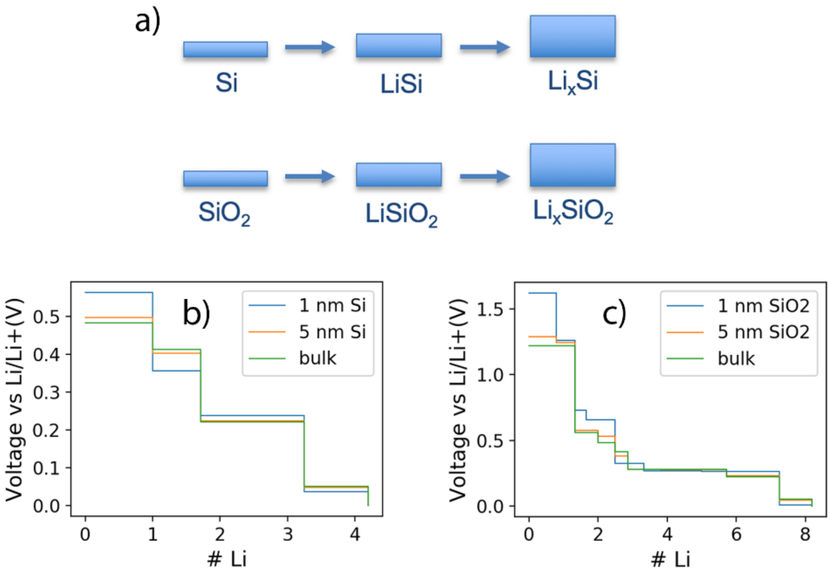

Figure 4. a) Schematic of film expansion during lithiation; b) Lithiation profile for amorphous Si films; c) Lithiation profile for amorphous SiO_2 films.

Starting with a fixed amount of Si or SiO_2, we calculate the film thickness at each lithiation step, assuming the film expansion is limited to only the film-normal direction, with little stress in plane, as shown in the schematic in Figure 4a. The film energies are then calculated for the expanding film, following the regressions shown in Figure 3, and a convex hull is constructed. Using the chemical potential of Li in each of the hull simplices, we obtain the lithiation profiles shown in Figures 4b and 4c. In general, we find the trend that films have a higher initial lithiation potential than bulk materials. This is primarily due to the decreased stability of the initial film. As the film grows, through lithiation, the relative number of surface atoms to internal atoms decreases, and the difference in lithiation potentials decreases.

This suggests that an amorphous oxide layer is preferred initially, but the energy conditions favor recrystallization after a very thin layer has formed. Also, thin-film materials in general tend toward higher potential for lithiation than their bulk counterparts.

SiO_2 Model System Studies

In general, flat Si wafers, such as those used in the semiconductor and photovoltaics industry, provide a good model system to study electrochemistry of the SEI formation, although the perturbing factors of diffusion and permeation through a coated layer are absent in these systems. Two general types of samples are used in these studies: i) silicon wafers that are diced to test samples and used as-is after a cleaning protocol and oxidation, and ii) samples that are backed by bulk copper current collectors and that have thin (~50–100 nm) Si physically deposited onto the Cu. These thin samples are then coated with SiO_2 through physical deposition, as well.

Si wafers with SiO_2 coatings must be tested in cells that define the electrochemically active area of the wafer using an O-ring to avoid participation of the wafer edges or rear in the electrochemical processes. This is crucial because the edges are not coated with SiO_2 and are thus initially much more electronically conductive.

However, a cell with an O-ring necessarily uses a larger electrolyte volume, and we found that this can lead to more pronounced side reactions. When only cleaning cell parts in dimethyl carbonate between experiments, galvanostatic cycling at 20 µAcm^{-2} yields continuous electrolyte reduction at voltages far above the lithiation potential. Through a series of experiments, we found that using fresh Li metal for reference and counter electrodes, using fresh electrolyte, and cleaning cell parts in organic solvents as well as water between experiments was crucial to suppress electrolyte reduction. With this procedure, we are able to achieve lithiation at current densities down to 5 µAcm^{-2} (see Figure 5).

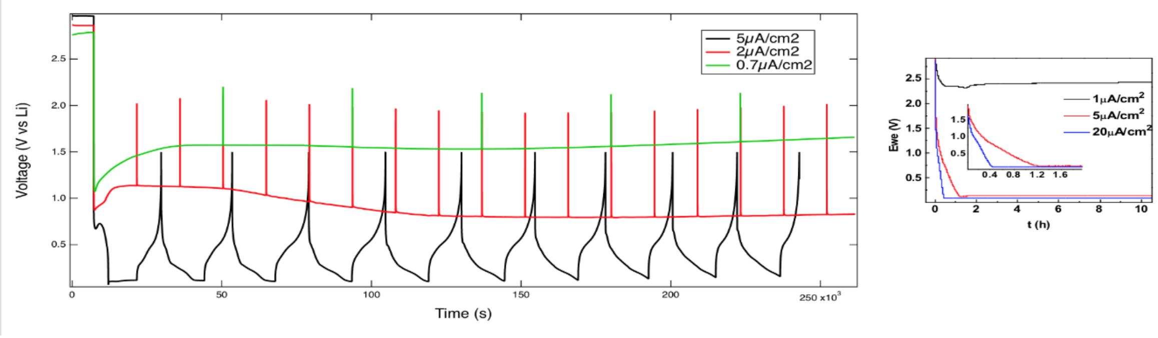

Figure 5. Left: Galvanostatic cycling results obtained with an O-ring cell and Si wafer anode as a function of current density at NREL (4-h half-cycles for 5 and 2 µAcm^{-2}, 12 h for 0.7 µAcm^{-2}). Right: Comparable results reported by LBL for a single lithiation cycle.

As seen from the figure, current densities of 2.0 and 0.7 µAcm^{-2} do not allow lithiation even with this optimized procedure This result agrees with earlier results, suggesting that this effect is not related to our particular cell components, but perhaps to the fact that ~1.4 mL electrolyte is used per cm^2 of anode area, as opposed to ~20 µLcm^{-2} in a typical coin cell. For the following studies, the cell cycling was performed at 20 µAcm^{-2}.

Using these O-ring cells, we proceeded to study the effect of 1.4–5.2-nm thermal SiO_2 coatings on the lithiation of Si wafers. Galvanostatic cycling was performed at 20 µAcm^{-2} in Gen2 electrolyte against Li metal counter and reference electrodes with no lower voltage cut-off; the results are summarized in Figure 6. From the electrochemical data, there is a stark difference between samples with less than 3.0-nm SiO_2 and more than 3.0-nm SiO_2.

Samples with less than 3.0-nm SiO_2 all cycle in the same manner: their cycling curves overlap (except for the very start, where 2.1-nm and 2.6-nm SiO_2 samples exhibit a spike to negative voltage vs Li (VLi), whereas the 1.4-nm sample does not), their Coulombic efficiencies overlap at over 99% from the 2nd cycle onwards, and photographs of cycled samples indicate uniform lithiation.

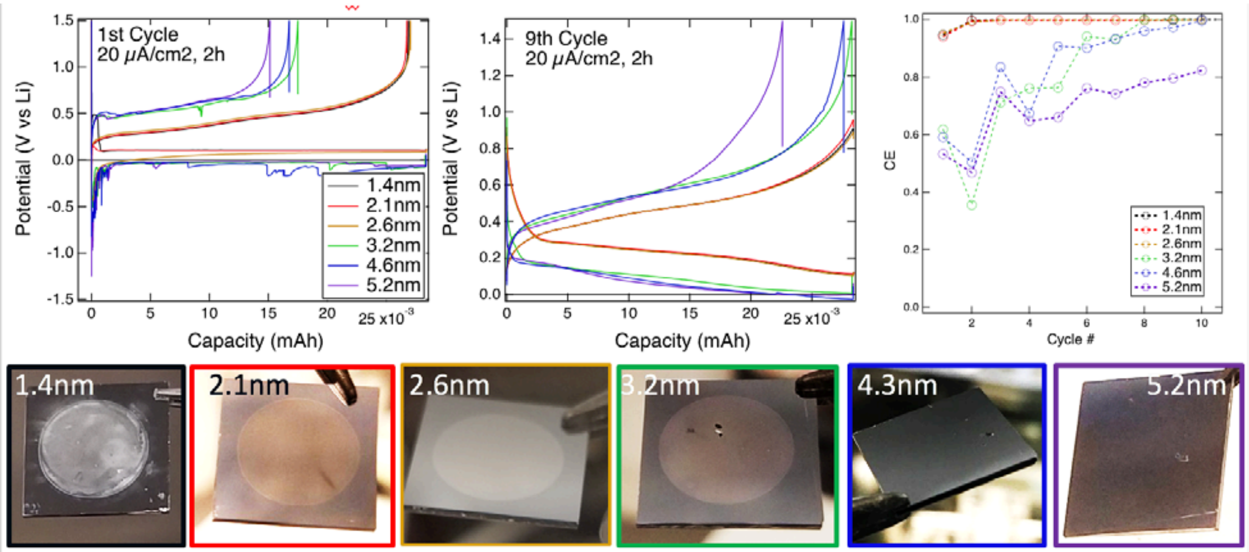

Figure 6. Cycling of Si wafer anodes with variation of SiO_2 coating thickness at 20 µAcm^{-2} with no lower voltage cut-off. Top: 1st and 9th cycles as a function of SiO_2 thickness (left, middle), and Coulombic efficiency as a function of cycle number (right). Bottom: Photographs of Si wafers after 10 cycles.

In contrast, samples with more than 3.0-nm SiO_2 initially only lithiate at negative voltages vs Li, exhibit low Coulombic efficiencies, and photographs of cycled samples at the bottom Figure 6 show only localized lithiation or Li plating. However, by the 9th cycle, they exhibit markedly higher Coulombic efficiency, and cycling occurs at positive VLi, although the difference between lithiation and delithiation voltages is higher than for thinner oxides, indicating that a higher resistance remains. This may be correlated to the question of amorphous vs. crystalline transformations discussed in the modeling sections or may be due to strict overpotential needs due to the resistance of the films.

Nevertheless, it appears that samples with more than 3.0-nm SiO_2 undergo a change within the first 10 cycles that facilitates lithiation, allowing it to occur at positive VLi and higher Coulombic efficiency—again, possibly due to conversion of the films to lower resistance, or to a more crystalline network structure. To determine whether this is due to prolonged exposure to low VLi, we acquired a second dataset on sister samples by holding them at 0.01 VLi and recording the current. These data, along with images of tested anodes, are shown in Figure 7.

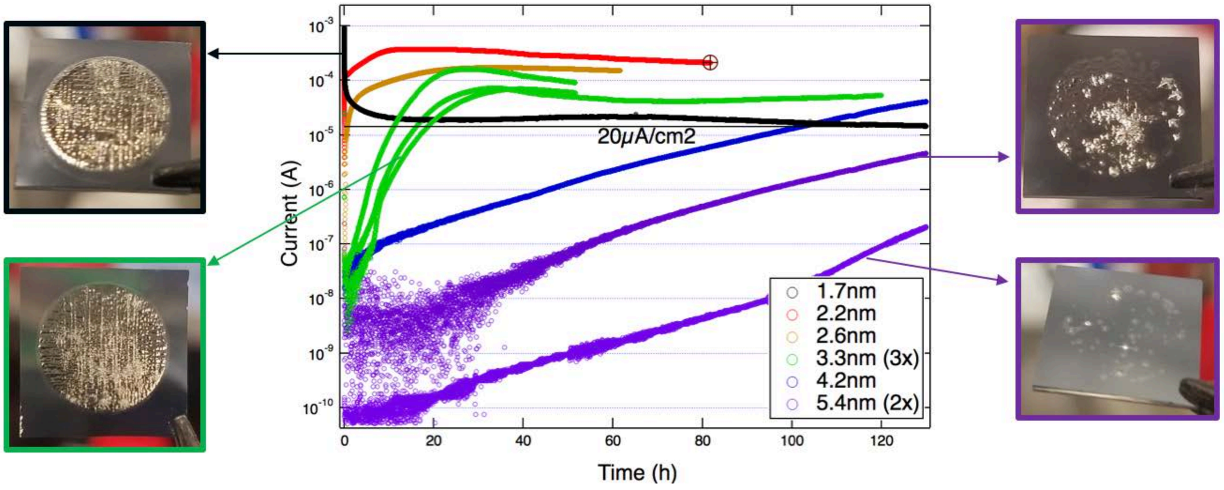

Figure 7. Chronoamperometry at 0.01 VLi for different SiO_2 thicknesses. Photographs of selected samples at the end of testing are shown.

Two regimes are apparent: samples with <3.0-nm SiO_2, which all cycled identically, rapidly reach currents above the 20 µAcm^{-2} previously used for cycling and reach a steady-state lithiation current after 15–20 hours. Examination of the anodes after testing reveals uniform lithiation overlaid with cracks resulting from the long duration of lithiation. On the other hand, samples with more than 4.0-nm SiO_2 initially exhibit very low currents, which rise slowly and exponentially by 2–3 orders of magnitude. This process appears to proceed at a fixed rate (the slopes of the corresponding curves are very similar), but the starting current varies widely, even among two nominally identical samples with 5.4-nm SiO_2. Examination of these two anodes shows that lithiation or Li plating in this regime is highly nonuniform: the process appears to initiate at pinholes, and then spreads radially. The somewhat random pinhole density on a given sample appears to be responsible for the initial current, from which the increase in current with time proceeds. The transition between the two regimes appears to occur around 3-nm SiO_2; hence, three samples with 3.3-nm SiO_2 exhibit intermediate behavior.

We investigated the changes in Si, Li, O, and F bonding by the XPS for thin (up to 2.6-nm) oxide overlayers, and morphology of two-dimensional (2D) chemical composition changes in Si samples with thick (~5-nm) SiO_2 using time-of-flight secondary-ion mass spectrometry (TOF-SIMS) mapping. The XPS results for the two thin SiO_2 layers are compared in Figure 8.

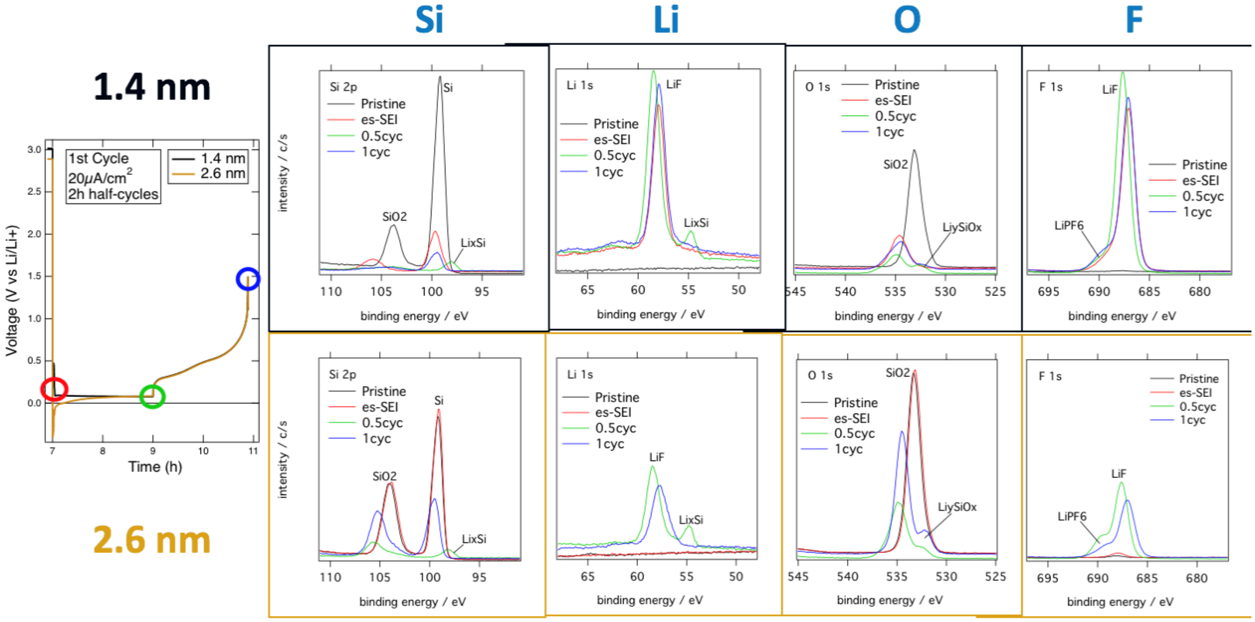

Figure 8. Changes in Si, Li, O, and F bonding studied by the XPS. Colors of the XPS curves correspond to the lithiation-delithiation stages in the voltage-time plot on the left (2 half-cycles, 2 h each).

From these data, we conclude that 2.6-nm SiO_2 blocks pre-lithiation SEI, because the SiO_2 remains visible after one full cycle, and that silicon wafer lithiates reversibly ($LiSi_x$ peak appears and disappears), whereas the conversion of silicon oxide to a lithium silicate $SiO_2 \rightarrow Li_xSiO_y$ is not reversible.

In contrast, samples with >3.0-nm SiO_2 overlayer initially only lithiated at negative voltages vs Li, exhibited low Coulombic efficiencies, and photographs of cycled samples show only localized lithiation or Li plating.

To study this in more detail, as the second microscopic/compositional technique, we performed TOF-SIMS 2D compositional mapping around the lithiated spots. The results are shown in Figure 9.

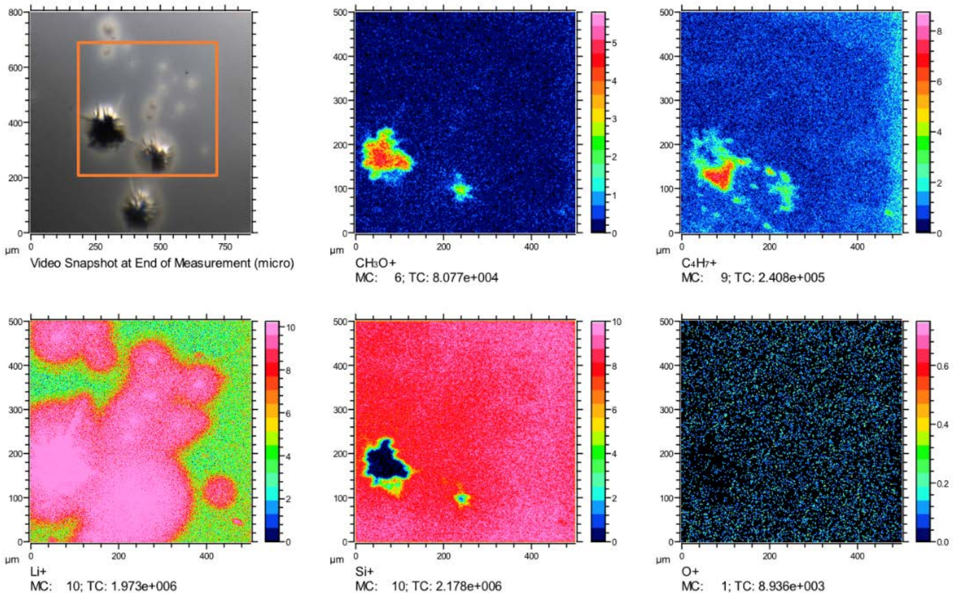

Figure 9. Two-dimensional TOF-SIMS map of Li, Si, O, and carbon-containing sputtering fragments, along with the optical micrograph. The mapping area was 500x500 microns and is shown in the micrograph by the orange contour.

These data show that the location of Li and of SEI-related organic species such as CH_3O+ and C_4H_7+, correlates with the optically visible features (pinholes). However, although the SEI species are localized there, the Li has spread massively over a much larger sample area than indicated by the optical contrast. From these 2D maps alone, it is not possible to attribute Li spreading to within the wafer (underneath the SiO_2) or first lithiating the SiO_2 overlayer. However, 2D depth profile maps (not shown) indicate that Li had first entered the Si wafer through the pinholes, and then had spread underneath the thick SiO_2. This suggests interfacial enhancement of Li diffusion. It further indicates that even if the area at which SEI is formed is limited to pinholes (which we might expect reduces the irreversible capacity loss associated with SEI formation), then lateral diffusion beyond the pinholes means that a larger area can be lithiated than had to be passivated by SEI, potentially lowering the irreversible capacity loss as a proportion of total capacity. This class of interfacial phenomena is currently used to design next-generation solid-state electrolytes [5,6].

CV Studies of Previously Lithiated Oxides

The previous data show that, above a certain thickness, oxides are too resistive to lithiate directly, and instead, they lithiate through pinholes in the oxide. Over time, it appears that these processes give rise to less electrochemically resistive structures and result in more nominal electrochemical behavior. It is possible that this process is the actual lithation of the oxide itself, as is predicted from the simulations. To study this possibility, physically deposited samples of previously lithiated oxides were prepared as thin-film 50-nm Si on 500-nm Cu on Si substrates. These samples were then used as substrates for the sputter deposition of 40-nm-thick lithium silicates of varying compositions (SiO_2, $Li_2Si_2O_5$, Li_2SiO_3, and Li_3SiO_x) expected from the tie line on the Li-Si-O ternary for lithiation of SiO_2. Note that these substrates are substantially thicker than those studied in the previous analysis and should therefore be electrochemically inert. These correspond to a 0, 1:1, 2:1, and 3:1 composition of Li:Si. Samples were then assembled into half cells using Li metal as a counterelectrode in a standard coin-cell configuration using Gen2 electrolyte without FEC. Cyclic voltammetry (CV) was conducted at 10 uV/s sweeps from open circuit to 0.08 V. As was observed previously, in the absence of pre-existing lithium within the oxide, the onset potential for lithiation was observed at 0.23 V, in good agreement with other observations for SiO_2-coated Si samples. However, if lithium was present at all in the oxide, the onset potential was significantly higher, near 0.35 V, and there were plateaus or peaks that manifested in the lithiation sweep. A first plateau that is present for all lithium-containing silicates exists at 0.31 V vs. Li/Li^+, which does not exist for the pure SiO_2 film. There are additional plateaus/peaks at lower potential, with increasing lithium content in the oxide resulting in an increasing onset potential for the second plateau. It may be that the first plateau is based on the formation of $Li_{12}Si_7$ with Li inserting into the Si substrate directly from the glass, and the lower-potential plateaus onsetting at the formation of $Li_{14}Si_6$ and $Li_{13}Si_4$, respectively, as the amount of available lithium for insertion from the oxide increases. These first-cycle CV curves are shown in Figure 10.

Further cycling of the samples in CV result in a steady evolution of both the early-onset potential plateau and the lower potential insertions. At the second cycle (see Figure 11), SiO_2 now shows some of the peaks observed from the silicates at both the $Li1_2Si_7$ and $Li_{14}Si_6$ state; and by the 14th cycle, the SiO_2 is closely matched to those films with the starting silicates, which potentially match to the onset of the $Li_{14}Si_6$ phase. This suggests that, upon cycling, any native starting oxide is lithiated to behave electrochemically similarly to those oxides that start with lithium in them, suggesting that evolution of the silicon oxide film toward a silicate-like structure may be happening. However, evidence of the silicates through direct beam observation are unable to identify these silicates directly, suggesting that it may just be the existence of lithium within the film that gives rise to these effects, rather than for formation of the stoichiometric silicates in the SiO_2 network. It may be that the presence of Li as a network modifier results in a substantively less ionically resistive film, as was observed in the thin-film studies above.

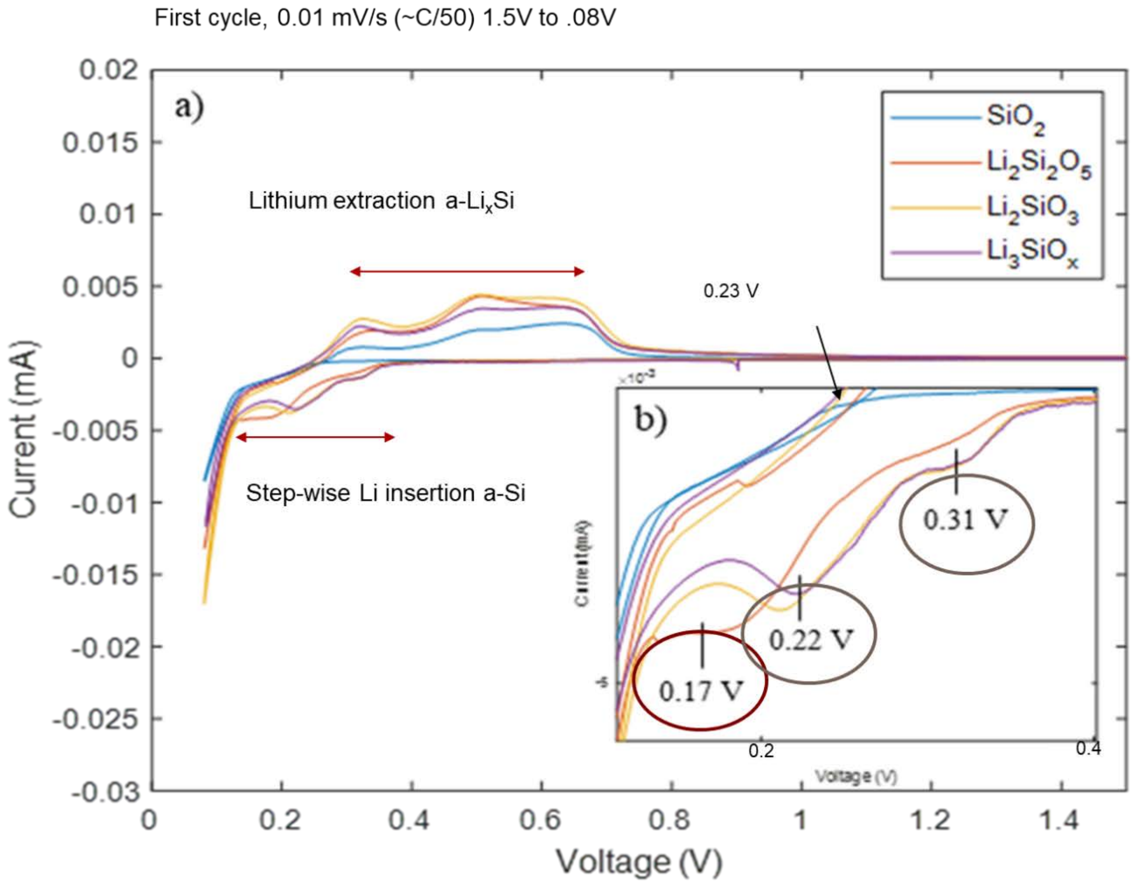

Figure 10. CV of 50-nm-thick Si_xLi_yO films under slow CV. Conditions: 25 °C, 10 µV/s, 50-nm Si/500-nm Cu/300-µm Si/20-nm Ti/200-nm Au WE, Li CE, Li RE.

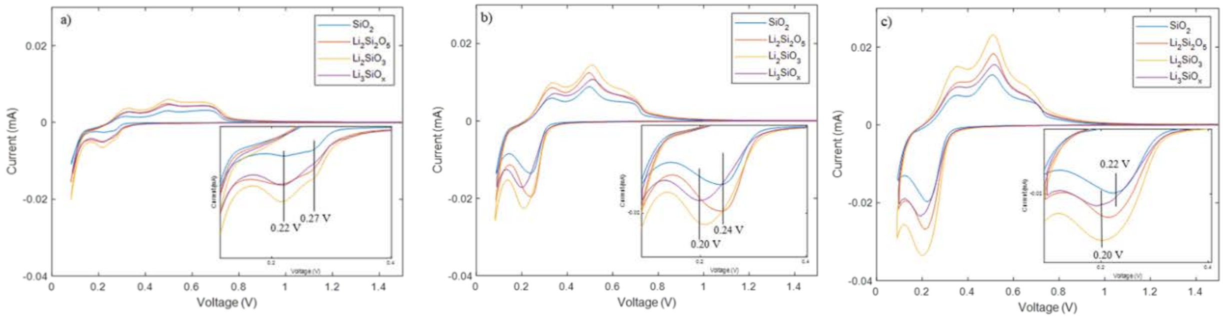

Figure 11. CVs of a) 2nd cycle, b)7th cycle, and c) 14th cycle of Si_xLi_yO samples under slow-scan CV (same conditions as above).

If the films are indeed becoming less resistive, such an effect should be visible as changes in their electrochemical impedance plots. To test this, films of varying composition were prepared as above and assembled into half cells with a lithium counterelectrode, with Gen2 electrolyte. Electrochemical impedance spectroscopy (EIS) was preformed between 10 kHz and 0.1 Hz with 10-mV perturbation and were studies as a function of both time and temperature. The resulting impedance curves are very different between film chemistries, with elevated temperatures showing a much-changed response over time. SiO_2 films exposed to the electrolyte show little change over time at room temperature, with several days of exposure showing minimal change (Figure 12). However, at 60°C and 80°C (Figure 13), there is significant evolution of the film conditions over time, and at 80°C, the equivalent circuit of the resulting response is quite different than in the simple capacitive case, indicating that lithium transport may be affected at the elevated temperatures, which

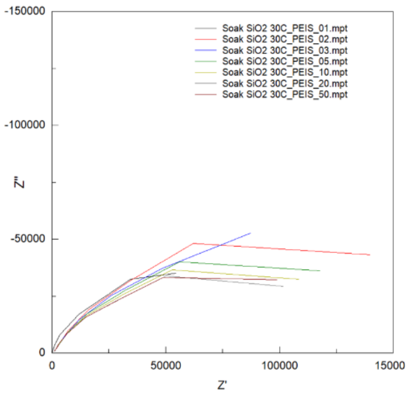

Figure 12: Nyquist plots of SIO2 film exposed to Gen-2 electrolyte at 30C for various times. Film evolution is very slow, with little change after several days.

would be expected if the Li is penetrating faster into the film over time at elevated temperature. In the case of highly lithiated films (such as the Li_4SiO_4 films), much different impedance response is observed. At room temperature, after a few hours, the impedance response starts to show signs of a low-frequency "loop" in the data, indicative of instability within the electronic response on the timescale of the experiment. At 80°C, the kinetics of the response are fast enough to remove this low-frequency loop, but the evolution of the film is largely complete by the time the first round of EIS is complete, and the film shows little further evolution over time at the elevated temperature. Because the electrical response model is changing depending on chemistry of the film and temperature, it is difficult to coordinate a single set of parameters to extract kinetic properties from the films using EIS solely; but the obvious change in conduction and EIS behavior suggests permanent conductivity changes occurring within the film, in agreement with the other studies done here.

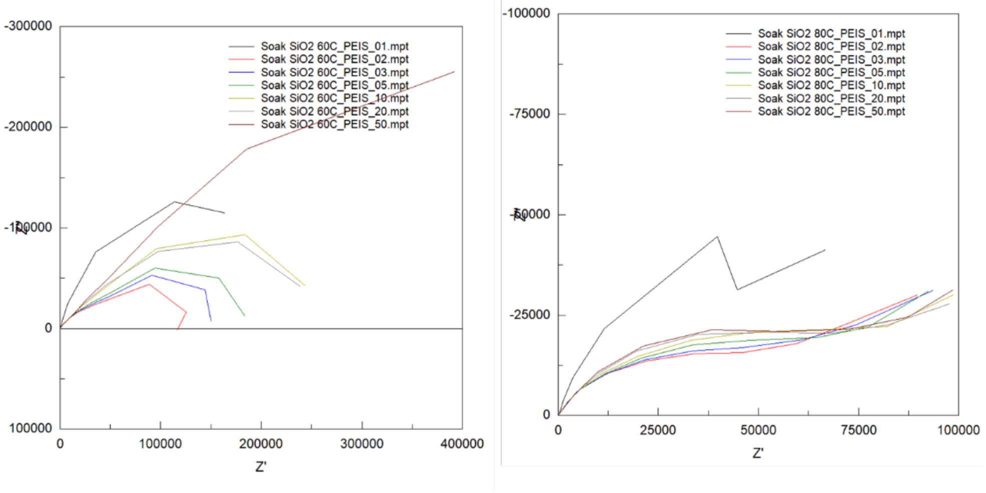

Figure 13. Nyquist plots of SiO_2 film exposed to Gen 2 electrolyte at 60 ° C (left) and 80 ° C (right) over time. Both the electrical model and the film evolution are dramatically changed from the room-temperature case.

Effect of Oxygen Content on Electrochemical Performance

In the final study done on flat model substrates, the question of oxygen and its role in allowing for lithiation was probed by changing the oxygen content of the starting film. SiO$_x$ anode with minimum oxygen content (referred to as Si) was prepared by magnetron sputtering with Si target under low base pressure ($\sim 2\times10^{-7}$ torr), low deposition pressure (5 mtorr), and short work distance (8 cm). This Si anode was assembled into coin cells after the deposition and was not exposed to air in the process. In other samples, the prepared low-oxygen-content Si was exposed to air to obtain Si with native oxide layer. To prepare SiO$_x$ anodes with higher oxygen level, we performed Si and SiO$_2$ co-sputtering with different power combinations (90–30 W, 90–60 W, 90–90 W, 60–90 W) for the Si and SiO$_2$ target and obtained SiO$_x$ anodes with four different oxygen levels. We also performed Si sputtering under different base pressures, deposition pressure, and working distance to study whether these different sputtering conditions would affect the performance of the obtained Si anodes. The thickness for all the Si and SiO$_x$ anodes reported here is around 50 nm, and all the cells were tested in Gen2 with 10% FEC.

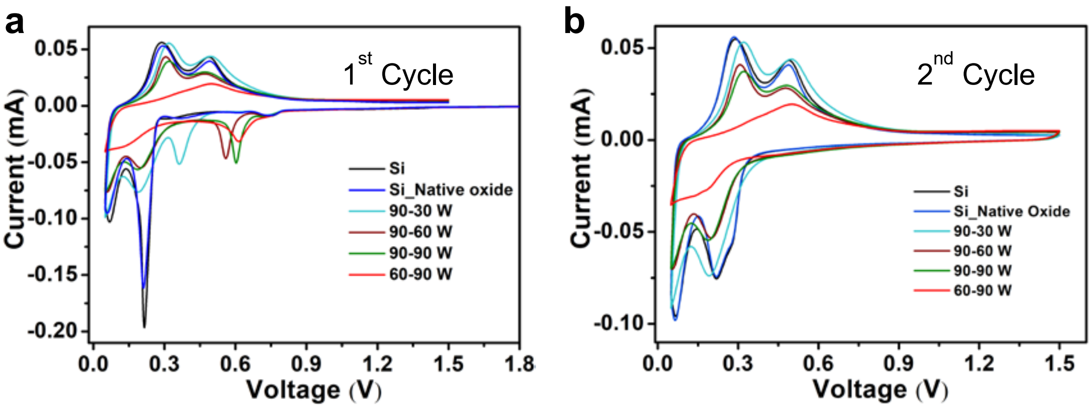

Figure 14. a) 1st-cycle and b) 2nd-cycle CV curves of Si, Si with native oxide layer, and four SiO$_x$ anodes with different oxygen level tested under the scan rate of 0.1 mV/s in the potential range of 0.05–1.5 V.

The obtained Si, Si with native oxide layer, and SiO$_x$ anodes with different levels of oxygen content were first evaluated with CV test at scan rate of 0.1 mV/s. As shown in Figure 14a, all the Si, Si with native oxide layer, and SiO$_x$ anodes exhibit a small reduction peak at around 0.7 V, which should be due to electrolyte reduction. By comparing Si, Si with native oxide layer, and SiO$_x$ anodes, a distinct difference is observed in the first CV cycle. All the SiO$_x$ anodes prepared by co-sputtering show an extra reduction peak in the potential range of 0.3–0.6 V, where the peak position shifts to lower potential with possibly lower oxygen content. This peak should be due to the formation of lithium silicates during the lithiation of the surface silicon oxides. Because the Si anode has very low oxygen content, it did not show this reduction peak—once again suggesting that lithiation into an oxide has an electrochemical signature.

Even for Si anode with surface native oxide layer, the oxygen level is still not high enough to exhibit this lithium silicate formation peak. In addition, both Si and Si with native oxide layer show a much stronger peak than the other SiO$_x$ anodes at around 0.2 V during the first cathodic process. This much stronger peak at low potential may suggest more electrolyte decomposition for Si anode and Si anode with native oxide layer. As Xu et al. have reported, lithium silicate is more stable toward the electrolyte than lithium silicide [7,8]. The formation of silicates at higher potential for SiO$_x$ may stabilize the electrodes toward electrolyte reduction at lower potential. Note that the SiO$_x$ anode synthesized with power combination of 60 W for the Si target and 90 W for the SiO$_2$ target have much broader redox peaks than other anodes, indicating a high resistivity of this anode due to its high oxygen content. All the SiO$_x$ anodes did not show the reduction peak in the potential range of 0.3–0.6 V in the second CV cycle (Figure 14b), which suggests that the formation of lithium silicates is irreversible. The reduction peak at around 0.2 V for Si and Si with native oxide layer was smaller during the second cycle, suggesting that there was more electrolyte decomposition during the first cathodic cycle, in agreement with other observations made for first-cycle electrochemical performance in the absence of formation cycles.

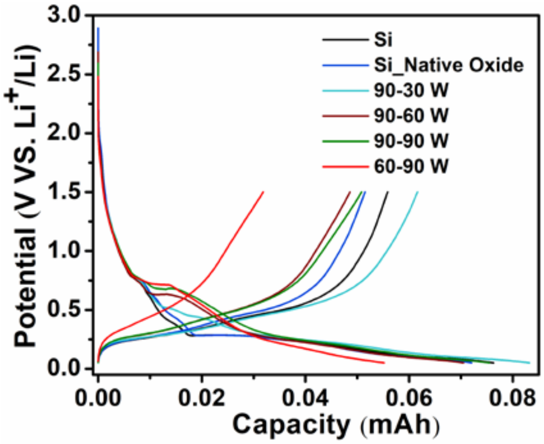

Figure 15. Galvanostatic charge-discharge profiles of Si, Si with native oxide layer, and SiO_x anode under the current of 1 C (6 µA) in the potential range of 0.05–1.5 V.

The galvanostatic charge-discharge profiles of all Si and SiO_x anodes (Figure 15) agrees well with the CV data, where the Si and Si with native oxide layer show similar shapes during the first discharge and the SiO_x anodes with higher oxygen content have a much longer plateau in the potential range of 0.3–0.7 V. The potential of the plateau is higher for SiO_x with possibly higher oxygen levels; again, this agrees with the potential of the reduction of SiO_x during the first cathodic CV cycle. The first-cycle Coulombic efficiency for Si, Si with native oxide layer, and SiO_x with different power combination is 75%, 75%, 73% (90–30 W), 69% (90–60 W), 67% (90–90 W), and 58% (60–90 W), respectively. Increasing the oxygen content appears to lower the first-cycle Coulombic efficiency, possibly due to the irreversible formation of lithium silicates. The cycling performance of all these anodes was also evaluated, and the capacity retention at 100th cycle is 69%, 69%, 70%, 72%, 75%, and 84% for Si, Si with native oxide layer, and the SiO_x obtained at 90–30 W, 90–60 W, 90–90 W, and 60–90 W, respectively. It is worth noting that although SiO_x obtained at 60–90 W has a much better capacity retention, its reversible capacity is much lower than others due to its high oxygen content. The cycling test was performed by running three cycles at 1/10 C (6 µA) and then raising the current to 1 C. The capacity retention was calculated by comparing the capacity at 100th cycle with the 1st-cycle capacity at 1

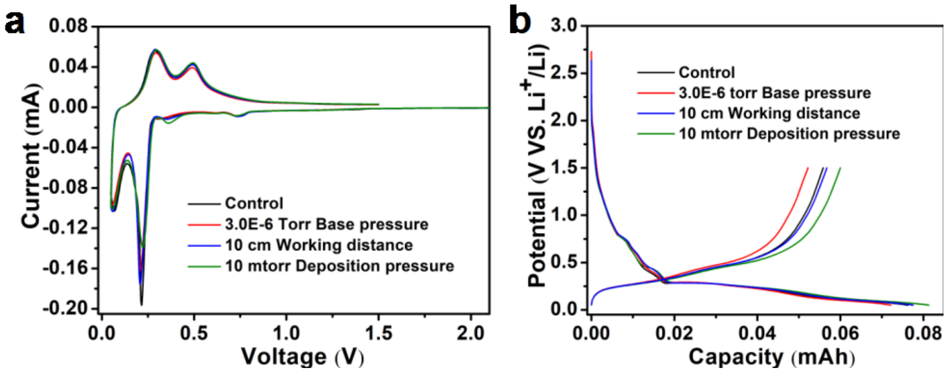

C.

Figure 16. CV curves and galvanostatic charge-discharge profiles of Si prepared under different sputtering conditions under the scan rate of 0.1 mV/s in the potential range of 0.05–1.5 V.

The CV curves and galvanostatic charge-discharge profiles of all the pure Si anodes prepared under different conditions (changing base pressure, changing working distance, and changing deposition pressure) were also collected, and these results are shown in Figure 16. All these Si anodes prepared under different conditions did not show a clear difference from both the CV curves and the charge-discharge profiles. In addition, their capacity retention at 100th cycle is also all around 69%. These results indicate that these different Si anode preparation conditions did not lead to a large difference in the oxygen level and electrochemical performance, therefore giving us some flexibility in preparing the Si anode with magnetron sputtering. We recognized, however, that these changes, although they may not give rise to electrochemical behavioral changes in the flat electrodes, do give rise to stress variation. Because stress applied to the SEI has previously been suggested as a reason for the loss of capacity, efforts to measure the stress in thin, flat Si films was undertaken.

Interfacial Stress Measurement

Measuring the stress in thin-film samples requires that the substrates be compliant and that the changes in shape on these thin samples can be measured accurately while in contact with the electrolyte and undergoing electrochemical cycling. To make measurements that allow simultaneous measurement of mechanical displacement and electrochemical behavior, new samples were constructed that are similar those used above, but remove the rigid Si substrate, leaving only a thin Cu layer covered by a nanometer-scale Si layer. The resulting thin samples are sufficiently compliant that stress changes due to electrochemical phenomena occurring on the silicon will register as changes in mechanical shape of the sample, which can be observed using a printed grating on the back of the substrate and Moiré interferometry.

As part of this effort, a new test cell needed to be designed that allowed for electrolyte contact with the Si continuously, even as the substrate moved during the lithiation and delithiation process. The current cell design is shown in Figure 17A, featuring a PEEK body and metal heating block. Two chambers are used to allow for pressure equalization to prevent the thin electrodes from rupturing. The electrodes are 2-µm copper foils with a 50-nm Si thin film held in place by an O-ring and washer. The thin foil electrodes are intended to enable magnified changes in stress in the electrode, leading to easier measurement of strain.

The first half of the custom microscope is displayed in Figure 17B including the optical illumination arm, objective, and camera. A schematic of what the finished interferometer will consist of is shown in Figure 17C. The Moiré illumination arm, containing the reference grating, is currently in progress.

To calibrate these measurements, thermal expansion experiments were performed to verify the microscope's functionality and applicability for measuring strain in silicon and the SEI in the future. A film of 500 nm of Cu was evaporated on a silicon wafer. A grating, with a period of 4 μm was then patterned on top of the Cu. The amplitude grating consisted of 2-μm bars of 610-Å-thick Si. With an incident light wavelength of 470 nm, the silicon has near-zero reflectance while the copper has near-total reflectance. Moiré fringes that are formed due to the offset of the sample and reference gratings (Figure 18A) create a sine wave with varying amplitude (shown in Figure 18B). The frequency of this sine wave is consistent over the area of interest, indicating uniform heating of the sample. By fitting the sine wave and tracking the change in frequency with temperature, the strain and coefficient of thermal expansion (CTE) of the material can be determined. The silicon wafer substrate has a theoretical CTE of about 3–5 ppm/K in the temperature range studied. As seen in Figure 18C, the experimental CTE can be found from the slope and is estimated as 4 ± 0.9 ppm/K. Each 30°C change in temperature corresponds to ~0.0001 change in strain whereas the lower limit of strain measured in silicon anodes in the literature is on the order of 0.003 [9,10,11]. This demonstrates the nondestructive ability of Moiré microscopy to measure the strain in silicon and the presumably smaller changes in strain caused by the formation of the SEI. Next will be to apply this confirmed technique to the *in situ* measurement of strain during the operation of a battery.

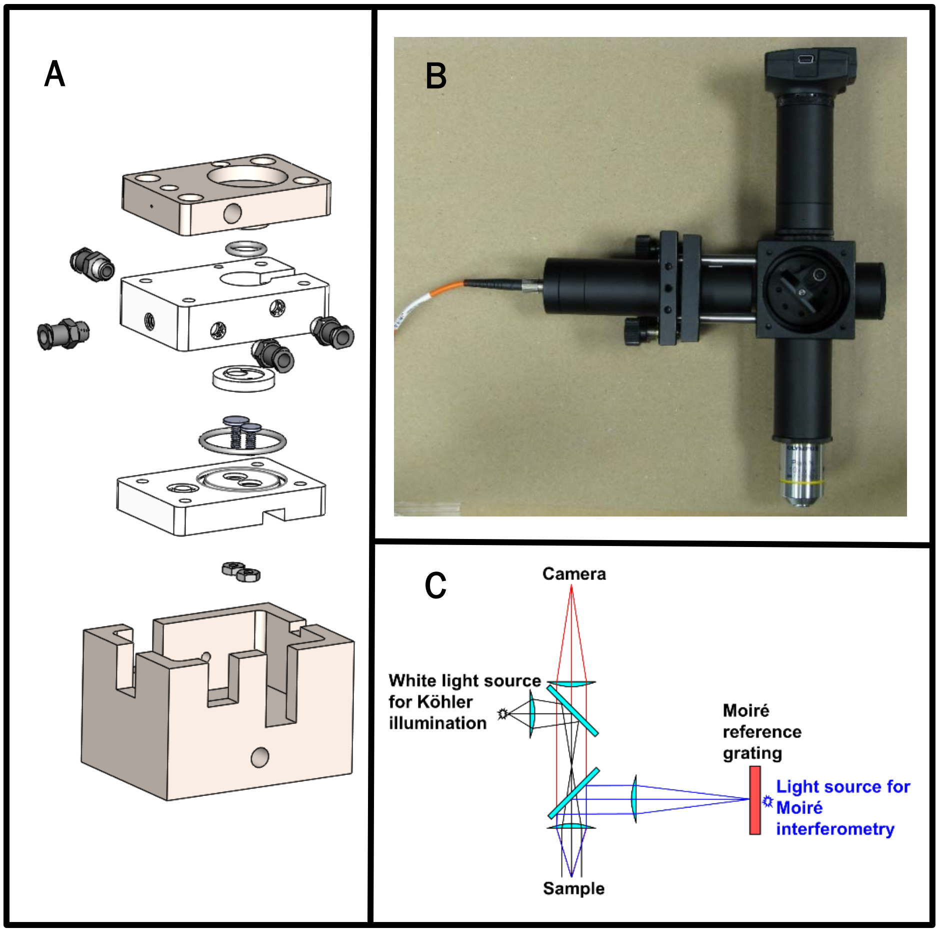

Figure 17. A) Moiré *in situ* cell design with PEEK pieces in white and the metal heating elements in beige. B) Current custom microscope with optical illumination arm complete. C) Schematic of the targeted design of the final Moiré microscope.

Lastly, the electrochemical behavior of the thin samples were verified in the same *in situ* cell assembly. The cyclic voltammograms of 2-µm Cu and 50-nm Si on 2-µm Cu are shown in Figure 18D. In the first cycle, there are two contaminant peaks at ~0.74 V (Cu and Si samples) and 0.5 V (only Si samples) vs. Li/Li$^+$ in the first cycle that are not typically observed in the literature but are present in other samples previously reported and seem to be related to the oxide content of the films. From these data, both the electrochemical behavior of the Si and the mechanical measurements are compatible and will be used in the coming year to assess the stress in the films as the SEI is formed and evolves over time.

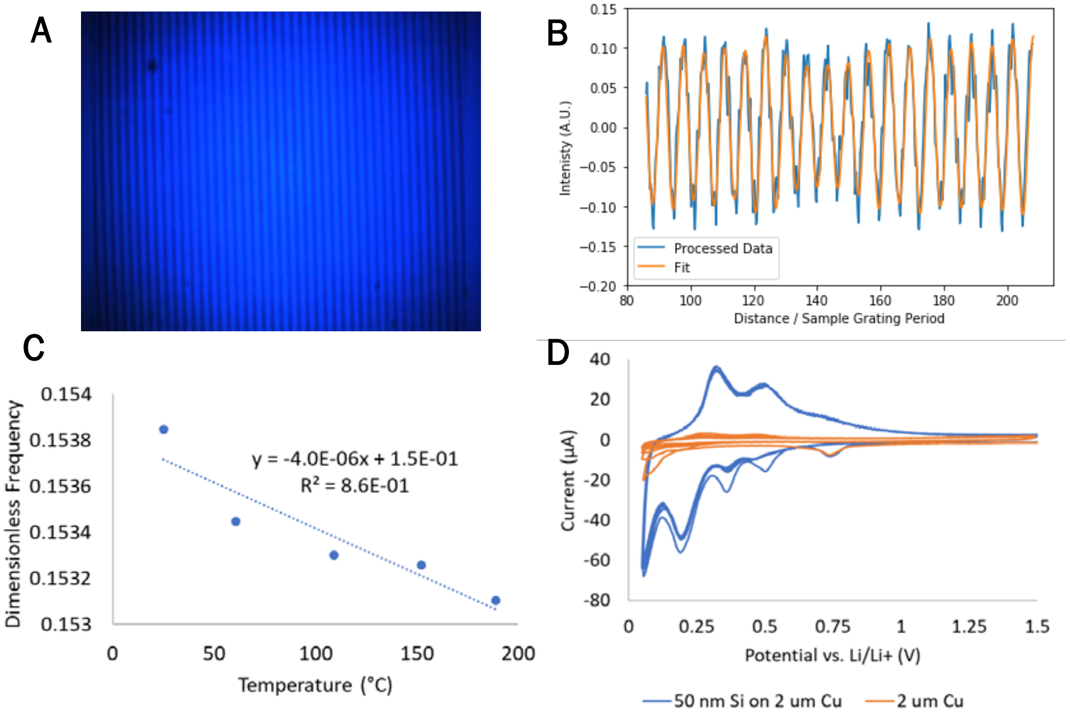

Figure 18. A) Moiré fringe pattern using 470-nm incident light for the Si wafer thermal expansion experiments. B) Cross-sectional average of the Moiré fringe pattern given in A with the data in blue and the fit in orange. C) Dimensionless frequency obtained from the sine-wave fit for each temperature with the slope giving the CTE of the silicon wafer substrate. D) Cyclic voltammogram of the 50-nm Si on 2-µm Cu in blue and 2-µm Cu in orange. The working electrode was the silicon on copper foil and the counter/reference electrode were lithium metal. The electrolyte was the Gen 2 electrolyte. The scan rate was 0.1 mV/s at room temperature. Contamination peaks seem to be present during the first cycle.

Oxygen-Free Particle Formation and Studies

The presence of oxygen, either included in the particle or as a surface oxide, is now understood to have a dramatic effect on the transport of lithium and subsequent electrochemical behavior in the model systems. Any commercially available powders that can be procured for producing Si electrodes have some (often uncontrolled) oxygen in them as part of their preparation. Removing that oxygen in the preparation allows us to study just the effects of the Si, to introduce controlled amounts of oxygen, and to study the effects of different surface modifications. Air-free Si nanoparticles (NPs) production by nonthermal plasma synthesis allows this and was developed previously under the SEISta program. This activity has been significantly expanded to enhance both the size and yield of the NPs. This effort now allows us to regularly produce 30-nm-diameter Si NPs in gram-scale quantities (Figure 19). These are incorporated into various studies on both the inorganic chemical interface, detailed below, as well as the chemistry at the Si NP interface (included in the (Re)engineering of the Si/Electrolyte Interface via Molecular Interactions section).

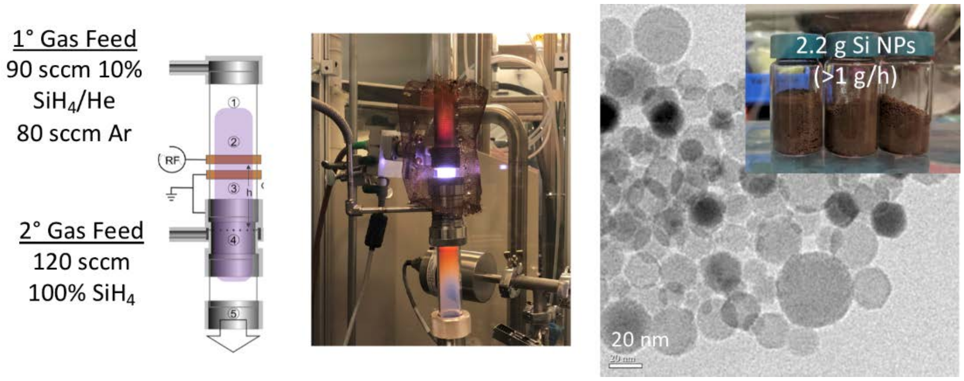

Figure 19. Summary of optimized nonthermal plasma growth conditions for preparing 30-nm-diameter Si NPs at gram scale.

All electrode slurries using these NP powders are prepared using in-house purified polyacrylic acid (PAA) binder and dried Timcal C65 conductive carbon in purified N-methyl-2-pyrrolidone (NMP) solvent. Slurries of plasma-grown 3.9–35-nm Si NPs contain 1:4:2 Si:TimcalC65:PAA. The low Si/C65 ratio ensures an effective electrical percolation network with smaller NP diameters (because percolation scales inversely with NP size, Figure 20). We have previously determined that processing Si NPs in water results in significant surface oxidation (penetrating at least 3 nm into the particle) and that *the SiO_2 formed is electrochemically inactive toward lithiation/delithiation*, as evidenced by the lack of a delithiation peak in the dQ/dV plots in water-processes electrodes (Figure 20). This matches previous work in the thin-film form where oxides larger than 3 nm are electrochemically inert under normal polarizations. For air-free Si NPs with no oxide, the capacity fade rate was minimal, with ≥99.0% Coulombic efficiency (CE) from cycles 20–100 (Figure 20). However, given that the CE was constantly increasing, this suggested poor wetting of active material (slurry formulation needed to be optimized). The air-free slurry formulation process has since been optimized so that we could more definitively understand the role of the oxide SiO_x on the capacity fade rate.

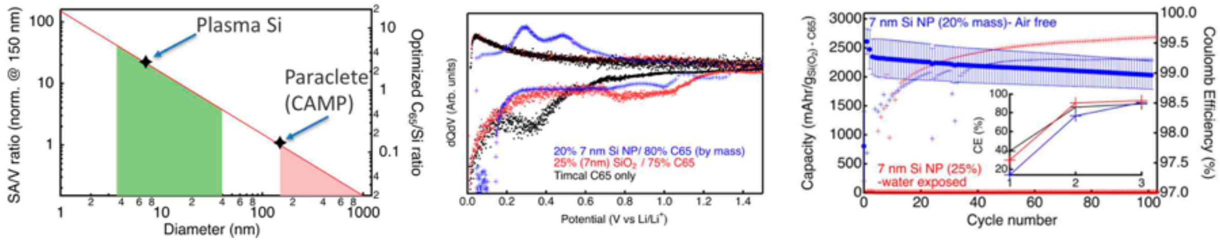

Figure 20. Left: C_{65}/Si ratio must increase as the Si NP size decreases to ensure an electrical percolation network for active anode material as the surface area/volume ratio increases. Center: Normalized dQdV versus potential plot of the 1st cycle of the same samples showing that only the air-free-processed Si NP electrode undergoes reversible lithiation and

delithiation, whereas SiO_2 electrodes do not exhibit reversible lithiation. Right: Capacity and Coulombic efficiency of half-cell anodes made from plasma-grown Si NPs (blue) fabricated air-free using NMP solvent or (red) in air using H_2O solvent.

With an optimized slurry process, coatings of NP were made that allowed us to deduce the effects of chemical (SiO_2) and mechanical stress (Si NP size) on capacity fade. In addition, we carried out a detailed impedance spectroscopy analysis of the SEI layer for Si NPs with and without surface oxide.

Figure 21a shows the normalized capacity at a cycle 50 using a C/5 rate for Si NP ranging from 4–35 nm in diameter. The gravimetric capacities of these anodes range between ~1700–2500 $mAhg^{-1}_{Si}$, and there is no obvious dependence of gravimetric capacity on NP size. We believe the range of capacities is likely related to C_{65} percolation. Therefore, we normalize capacity data to highlight the important dependence of the capacity fade rate on the Si NP size. From Figure 21a, the *smallest 3.9-nm-diameter Si NPs display the flattest curves and exhibit virtually no change in capacity over 100 cycles*. At Si NP diameters >10 nm (13–35 nm), the largest 35-nm-diameter Si NPs display the steepest curves; but all Si NPs in this size regime show very similar fade rates because the traces of each are nearly superimposable on each other. To further analyze these data, we fit the traces in Figure 21a (starting from cycle 20) to a linear function to extract an average capacity fade rate per cycle for each of the SiNP sizes measured. Those data are shown in Figure 21b.

From Figure 21b (blue data points), the smallest-diameter Si NPs have the lowest fade rate and the largest Si NPs have the fastest fade. From this plot, however, the trend is clearly not linear—as the SiNP size increases, the capacity fade rate appears to approach a horizontal asymptote. Thus, this scatter plot is fit with a sub-linear power function (black dashed line in Figure 21), where the exponent = 0.75. We do not currently have an explanation for the significance of this number, other than that the fade rate is likely related to the ratio of surface area to volume (SA/V). When the same data are plotted against their SA/V (Figure 21b inset), the data fall on a linear fit, which suggests that the origin of capacity fade is a combination of chemical (surface area, SEI) and mechanical (volume expansion/contraction) properties of the electrode.

We next performed additional experiments on water-processed Si NPs that will have a SiO_2 shell (red data points, Figure 21b). Interestingly, these SiO_2-terminated Si NP samples overlay perfectly on the same exponential fit as the SiH_X-terminated Si NPs, suggesting that with these plasma-derived Si NPs, surface oxidation has no effect on the capacity fade rate. Another surprising result is found with Paraclete Si NPs (provided by CAMP, processed into slurries and electrodes at NREL), where these heavily oxidized SiO_2/Si NPs also fall on this curve. This result suggests that regardless of initial inorganic interface, all roads point toward the same capacity fade rate under these conditions.

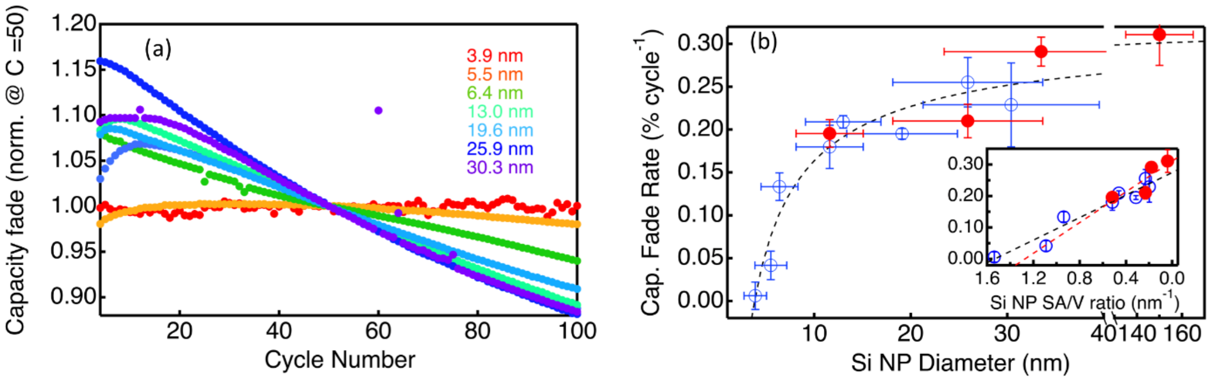

Figure 21. (a) Normalized cycling data for a range of SiH_X-terminated Si NP anodes. The data here have been normalized to their capacity at cycle number 50. (b) Scatter plot of the average capacity fade rate as determined by fitting the last 50 cycles of each of the different-diameter Si NP-based anodes. The data in the blue open circles represent silicon with SiH_X-termination, and the data in red are those from oxidized (SiO_2) Si NPs. The black dashed line is a power function fit to the SiH_X-data with the form cap. fade = axn + b, where x represents the Si NP diameter. The inset is the same data plotted as a function of Si NP surface-area-to-volume (SA/V) ratio.

We next probe the electronic properties of the SEI with and without surface oxidation on the Si NPs. EIS analysis of these composite anodes are conducted at three different states of charge after the first formation cycle (2^{nd}-cycle delithiation). The impedance data are summarized in Figure 22. Figure 22a shows the Nyquist plots for 11.6-nm Si NP anodes with and without surface oxidation, as well as the equivalent circuit used to model these data. The equivalent circuit is established in the literature for silicon anodes [12]. In these measurements, there are three distinct processes occurring at different timescales. The fastest process (first semicircle) is double-layer charging (CPE_{DL}) and electrical resistance associated with electron propagation at the surface ($R_{Surface}$). As expected, the SiO_2 surface has a much higher $R_{Surface}$ than the SiH_X-terminated Si NPs. The second process is associated with ion conduction through the SEI (R_{SEI}) and SEI capacitance (CPE_{SEI}). This process occurs on the 1–100-ms timescale. The third process is lithium diffusion in silicon and is accounted for with a Warburg circuit element. Because this process is slow, we are not able to make meaningful conclusions from the fits, and therefore, we analyze the characteristics of the SEI component only.

Figure 22c displays plots R_{SEI} after the first formation cycle. For all samples measured, R_{SEI} decreases as the potential increases, indicating that the electronic character of the SEI at these Si NPs varies with potential. The SiO_2-terminated Si NP anodes display increased R_{SEI} compared to the SiH_2-terminated Si NPs, implying that SiO_2 contributes to the SEI and that it impedes Li^+ diffusion. The capacitance for this process is shown in Figure 22d. Interestingly, the capacitance for the SiH_X-terminated Si NP anodes is higher than that of the corresponding oxidized SiO_2-terminated Si NP sample. This could mean that the SEI formed from SiH_X-terminated Si NP anodes accommodates more Li^+ or that the SEI is thicker. Finally, we plot the RC time constants for all of the measured anodes. As shown in Figure 22e, the time constants are slower for the SiO_2- versus the SiH_x-terminated Si NPs electrodes. Taken together, all these observations indicate that the electronic character of the SEI depends greatly on the inorganic surface of the Si NP. However, given that the capacity fade rate appears to be unaffected by the presence of SiO_2 and simply depends on the Si NP size, the differences in the SEI between SiH_X- and SiO_2-terminated silicon are unimportant with respect to the overall capacity-fade mechanism.

Finally, to test whether the limited Li^+ conduction (increased R_{SEI} and decrease C_{SEI}) limits the rate capability of the electrode, we carried out a rate-dependence experiment in which the lithiation/delithiation rate capabilities are affected by the SiO_2 interface. The results are summarized in Figure 22b. All the samples measured show a decrease in the delithiation capacity as the rate increases from C/20 to 10C. However, the magnitude of scan-rate dependence is strongly influenced by the Si NP size, where smaller-diameter Si NPs retain more capacity with increasing scan rates compared to larger-diameter Si NPs. Comparing the rate dependence for the samples of the same Si NP size, but with or without surface oxide layers, there appears to be no difference between the capacity drop between SiH_x- and SiO_2-terminated Si NP electrodes. This surprising finding suggests that the measured SEI character is not limiting the uptake of Li^+ during lithiation/delithiation. Rather, the limiting factor is related to Si NP size, indicating the Li^+-diffusion in silicon determines the rate dependence.

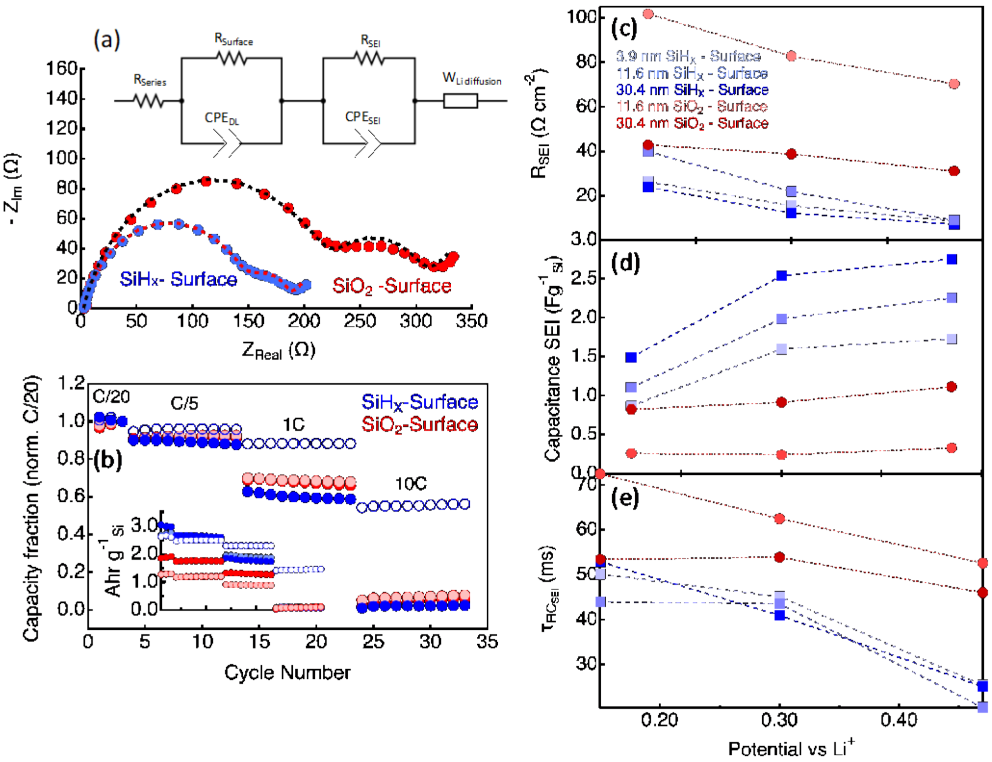

Figure 22. (a) Representative Nyquist plots for Si NP-based anode half-cells with (red) and without (blue) an intentionally grown surface oxide (SiO_2) layer. The equivalent circuit used to model these data are shown in the top of panel (a), and fits to the data using this circuit are shown in the dashed lines. (b) Normalized scan-rate-dependent data for SiH_x- (blue) and SiO_2- (red) terminated Si NPs for 3.9 nm (open circles), 11.6 nm (light-colored circles), and 30.3 nm (dark-colored circles). The inset shows the non-normalized data. (c) Values of the resistance of the SEI layer (RSEI) extracted from fitting the impedance data. (d) Values of the capacitance of the SEI layer (RSEI) extracted from fitting the impedance data. (e) RC time constants for impedance process associated with the SEI layer.

$LiSiO_x$ Powder Chemical Reactivity Study

The question of formation of the silicates during lithiation and delithiation is still debated, but there is ample evidence that a combination of Li, Si, and O are present in the SEI during formation and subsequent cycling, whether they form the crystalline silicate phases as the modeling has previously suggested. It may be that they are kinetically hampered in this formation, or that the transport of the lithium ion across the silicon oxide retards the recrystallization into the thermodynamically preferred phases, and so, only a quasi-stable amorphous structure is present in the film during electrochemical cycling. SEISta has previously reported that the presence of the electrolyte against such amorphous silicates (deposited via physical vapor deposition) results in the chemical attack of the silicate phases with increasing lithium content. This was at open-circuit potentials, and so, no current was flowing, although an exchange current would have been present in this system as it represents an electrochemical couple at dynamic equilibrium.

If the electrochemical processes are removed, there is the question of stability simply sitting against an electrolyte. Is the surface of any formed silicates intrinsically reactive enough to decompose the electrolyte salt and initiate chemical attack of the surface? To answer this question, a short study was done on powder forms of the silicates exposed to the Gen2 electrolyte, but in the absence of any electrochemical cell or exchange current. We synthesized high-purity raw silicates through the direct reaction with Li_2CO_3 and SiO_2 to form Li_2SiO_3, $Li_2Si_2O_5$, and Li_4SiO_4. The as-prepared materials were loaded in a glove box and subjected to a 500°C anneal for 2 hours to remove water and any surface carbonates. The dried materials were ground to a velvet-like consistency in the glove box prior to use. One gram of the resulting materials was exposed to 5 mL of the

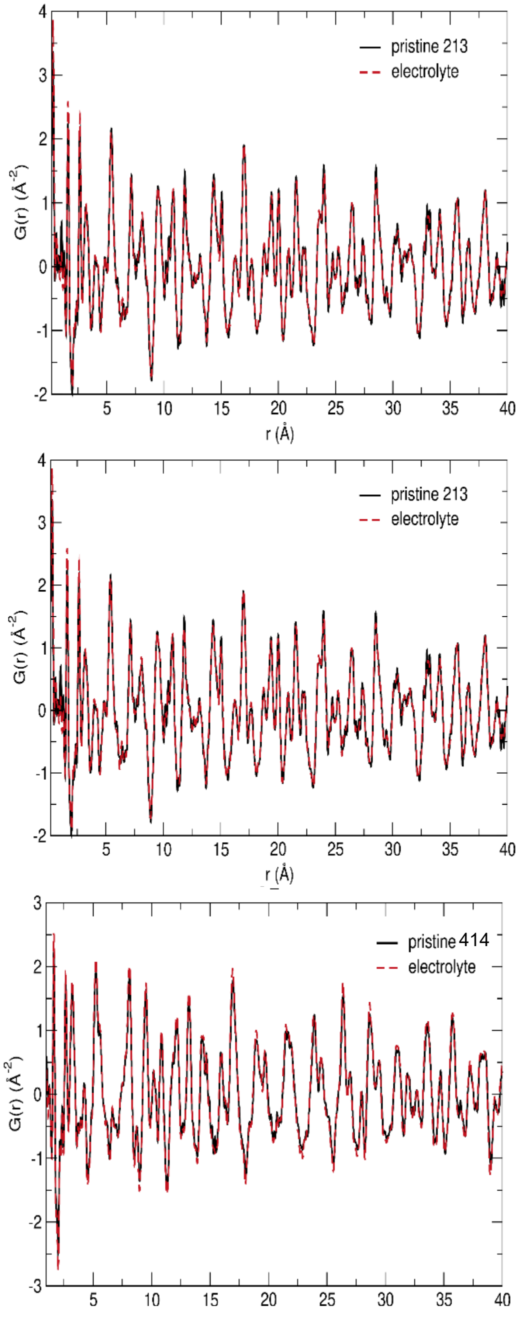

Figure 23. Neutron PDF data collected for Li_2SiO_3 (top), $Li_2Si_2O_5$ (middle), and Li_4SiO_4 (bottom) for the raw material (black line) and material exposed to electrolyte (red dashed line).

standard 1.2M $LiPF_6$ 3:7 wt% ethylene carbonate/ethyl methyl carbonate at 60°C for 72 hours to explore the reactivity of crystalline Li-Si-O materials with the electrolyte. Previous work on amorphous films indicated that the amorphous films reacted readily with the electrolyte forming a complex Li-Si-O-P-F layer.

After aging, the powders were collected and washed four times with 15-mL aliquots of dry dimethyl carbonate to remove residual solvents. The samples were dried in vacuum for 24 hours and packed in 3-mm glass capillaries. In addition, reference samples of LiF, Li_2CO_3, ethylene carbonate, $LiPF_6$, and pristine starting materials were loaded in capillary tubes. The samples were analyzed on the Nanoscaled-Ordered Materials Diffractometer (NOMAD) located at the Spallation Neutron Source. This instrument is ideally configured to collect data suitable for pair distribution analysis, which is useful for identifying structural correlations within amorphous material. Furthermore, neutrons are especially sensitive to low-Z elements such as Li and O, allowing for structural determination of materials containing these elements.

The results of the neutron study are shown in Figure 23. The black lines are the data collected for the pristine samples whereas the red dashed line shows the data after electrolyte exposure. From these data, there is no evidence of changes to the bulk structure of the Li-Si-O materials. Furthermore, there is no evidence of the formation of an amorphous surface phase on the crystalline materials. If there was such an amorphous phase, we would see new peaks and valleys in the data. Finally, there was no evidence for significant concentrations of organic species in or on the sample, which would attenuate the neutron signal due to the absorption of neutrons by H.

Together, this indicates that the crystalline Li-Si-O materials are very stable against the electrolyte. This is true at high temperatures where one would expect greater reactivity. Furthermore, we see no evidence of other significant lithium or organic phases trapped on the surface. These data do not exclude catalytic activity of the materials, but do point to stability in the crystalline phase. This is in contrast to the data measured for amorphous materials reported previously, which demonstrated significant electrolyte reactivity.

Microcalorimetry

When processed and incorporated into electrodes, silicon active material surfaces such as those that are being grown under the SEISta program above are altered from their pristine conditions in a way that likely influences SEI formation and function. To understand the difference between model silicon systems and powders incorporated into electrodes, microcalorimetry has been employed to measure the heat generated from the aqueous processing of silicon powders with LiPAA binders and carbon additives, because this technique can show how different processing conditions can give rise to substantively different heat generation depending on how the surface reacts during early cycling behavior. To initiate this study, commercially available powders were used to understand how the measurement would vary under known variances of surface treatment.

Previous isothermal microcalorimetry curves of nanosilicon from various suppliers showed the Paraclete-4KD commercially available Si powder material to have one of the highest peaks and average heat generation over the test duration, correlated to its high Brunauer, Emmett and Teller (BET) surface area. Although generated heat was known to correlate to BET surface area, this material sample was noted to also have poor surface properties that impacted cycling performance. We hypothesized that these surface properties may also correlate with our high heat generation. However, similar analysis of new Paraclete-G18 material, with improved surface properties and cycling, demonstrated nearly identical heat generation. This suggests that surface area is the primary correlative property because both samples showed similar BET surface areas. These data are summarized in Table 1.

Table 1. Quantified energy generation based on the fit curve of the Paraclete-4KD + CB sample in Figure 24 as well as predicted material and performance loss based on the formation of silica.

NanoSilicon	Peak Signal, μW	Average Signal, μW	Normalized Peak Signal, μW/g-Si	Normalized Peak Signal, μW/m^2-Si
Paraclete – 4KD	90.7	64.2	468.6	13.9
Paraclete – G18	97	57.3	489	15.2

Electrochemical microcalorimetry has also been carried out on two silicon-containing coin cells. The microcalorimetry fixture was first calibrated for dynamic time correction using a “dummy” coin cell of known resistance to both confirm measurement accuracy and enable reduction of signal latency by roughly one order of magnitude [13]. Figure 24a shows the overlay of the voltage and heat-generation curves for a full coin cell of NMC cathode vs Paraclete G18 anode. The current level of analysis does not enable us to isolate parasitic heat flow from other sources (entropic and ohmic), but it does provide quantification of the overall reduction in heat generation with subsequent cycling [14]. Figure 24b shows the measured coin-cell capacity along with heat generated per cycle, with both showing similar decreasing trends. The values measured here also agree closely with those reported in a newly accepted paper on microcalorimetry of silicon anodes [15].

Continued electrochemical microcalorimetry testing of coin cells will enable comparison of heat generation between cathodes and anodes within cells and, through controlled discharge parameters, enable isolation of the parasitic heat flow from the entropic and ohmic heat flow coming out of the tested coin cell. This will enable us to determine the point of cycling with peak parasitic losses as well as, through charge-counting potentiostatic measurements, determine the heats of formation for SEI layers at different states of charge.

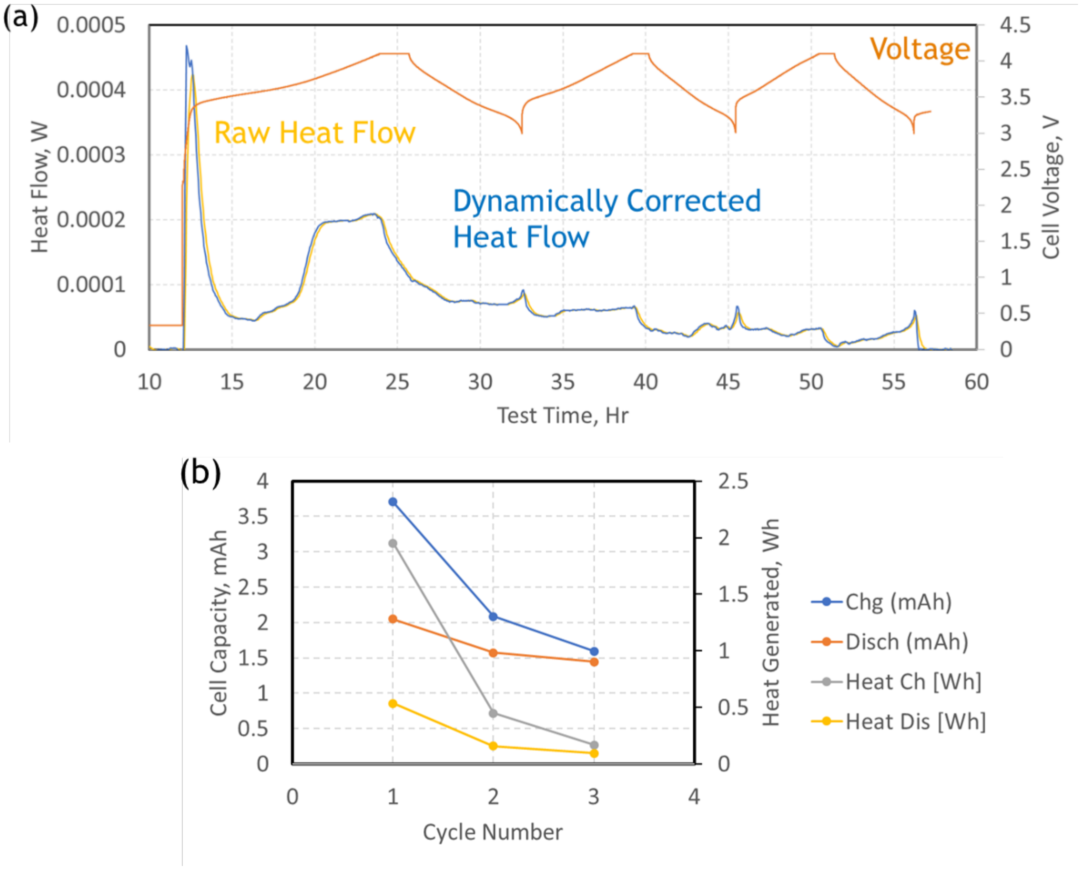

Figure 24. a) Heat flow and voltage curves for NMC vs Paraclete-G18 coin cell subjected to electrochemical microcalorimetry. b) The cell capacities and generated heat per cycle derived from these curves.

Zintl Oxide Electrochemistry

The nature and function of the reactivity of the Si surface (and of the SiO_2 surface) has been observed repeatedly to influence the formation and evolution of the SEI and to have an impact on the cycling of the Si electrode. Recently, workers in SEISta from ANL have used a small amount of metal salt additive in the electrolyte during cell construction to modify this surface. This is an attempt to stabilize its formation and evolution by supplying additional charge density at the surface of the Si to tie up uncoordinated Si near the surface and to hopefully improve the stability of this surface. To that end, experiments were done on powder-coated anodes that used a new electrolyte additive that forms a Zintl phase at the surface of the Si during assembly.

The half cells of Si electrode (CAMP A-A017, Paraclete Si nano-particle(80):C_{45} conductive carbon(10):LiPAA binder(10)) | GenF or GenFM (GenF + 0.1 M $Mg(TFSI)_2$) | Li metal were electrochemically cycled using 2032-type coin-type cells. Cells were subjected to one of three electrochemical treatments: 1) 200-mV GenF or GenFM (discharge and potentiostatic hold at 200 mV until $i \leq 5.0\times10^{-6}$); 2) 10-mV GenF or GenFM (discharge and potentiostatic hold at 10 mV until $i \leq 5.0\times10^{-6}$); or 3) 1-cycle GenF or GenFM (one galvanostatic cycle from 1.5 to 0.01 V (*vs.* Li/Li^+, hereafter) at a C/20 rate with potentiostatic hold at 10 mV until $i \leq 5.0\times10^{-6}$ between discharge and charge). The collected Si electrodes from cycled cells did not go through a rinsing process to protect formed Silicon SEI. All collected electrodes were stored in an Ar-filled glove box after vacuum drying at room temperature and transferred to each analytical equipment without air exposure.

Chemical Composition of Zintl Phase. Raman microscopy was used to investigate the chemical composition of the first cycle at 200 mV and 10 mV using both the GenF or GenFM electrolyte. Figure 25a shows a photograph of the six types of samples, and Figure 25b shows micrographs recorded through a 20x Raman microscope objective for the samples. Optically, GenFM samples look the same as GenF. The first-cycle GenF or GenFM composite anodes had a “powdery” appearance against the copper substrate and many individual microdomains. This surface morphology is likely due to cracking of the film after silicon expansion (during lithiation) and contraction (during delithiation). In contrast, the 200-mV GenF or GenFM samples have a very smooth crack-free appearance. Samples that were held at 10 mV in GenF or GenFM are also smooth, but many cracks exist, and the film has plate-like domains, many of which have detached from the copper foil, suggesting that lithiating the anode may have detrimental effects of anode adhesion properties. In Figure 25c, Raman spectra of the samples are presented and show expected chemical composition signatures. A large crystalline silicon (c-Si) peak at 520 cm^{-1} and band between 920–980 cm^{-1} appear in the 200-mV sample, indicating that it has not been highly lithiated. These peaks are present in the 1-cycle sample as well, but to a lesser extent. In contrast, the 10-mV sample shows almost no evidence of c-Si, except a weak 520 cm^{-1} peak for GenFM (suggesting incomplete lithiation). Instead, a new peak appears at 385 cm^{-1} that is attributed to lithium silicide (Li_xSi_y) [16]. Due to a peak from the sapphire window of the sample holder at around 420 cm^{-1}, we are unable to distinguish whether the phase of the lithium silicide is Li_7Si_4 or $Li_{13}Si_4$. Also observed in the Raman spectra are peaks representing the other components of the anode: conductive carbon (1355 and 1560 cm^{-1}) and LiPAA binder (1445 cm^{-1}). In this measurement, we did not observe any specific differences between GenF and GenFM samples in terms of chemical composition.

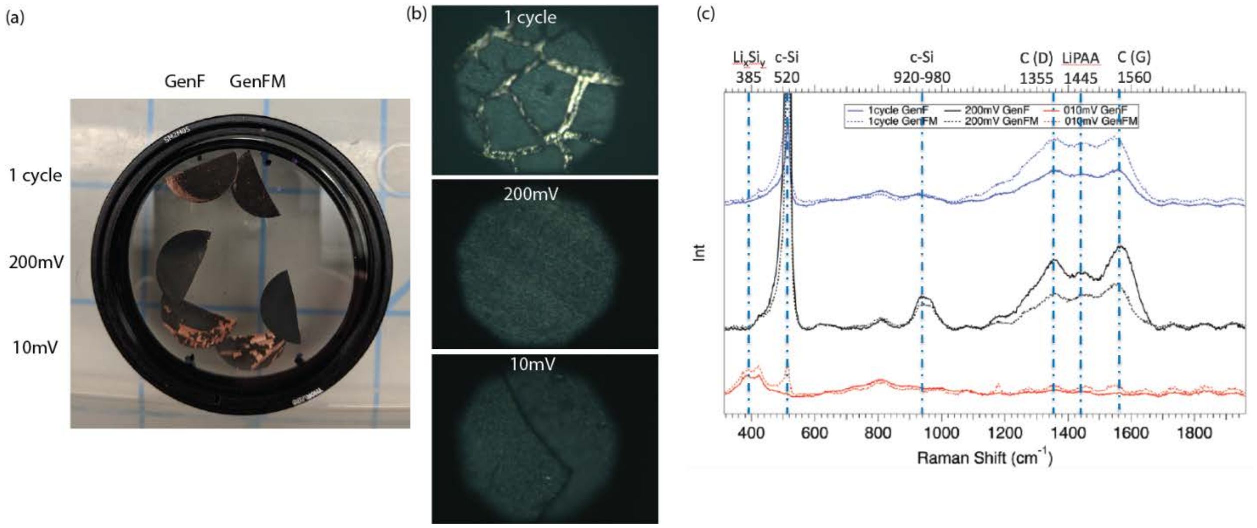

Figure 25. (a) Photograph of the 1-cycle, 200-mV, and 10-mV GenF or GenFM samples in the air-free holder used for micro-Raman analysis. (b) Optical micrographs of the samples imaged through a 20x objective on the Raman microscope. Samples from GenF and GenFM looked the same. (c) Raman spectra of the samples.

To further characterize the samples, we used two different methods of Fourier transform infrared (FTIR) spectroscopy. Figures 26a and 26b show the attenuated total reflection (ATR)- and diffuse reflectance (DRIFTS)-FTIR spectra, respectively. For reference, a pristine electrode spectrum is presented in Figure 26a (green line). The pristine sample matches well with previous studies [17]. Silicon oxide shows a broad peak between 1200 and 1000 cm^{-1}. A Si-O-Si absorption at 870 cm^{-1} indicates some SiO_2 surface layer to the silicon nanoparticles. In addition, we observe asymmetric and symmetric COO^- from the LiPAA binder at 1545 cm^{-1} and 1400 cm^{-1}, respectively. There is also a C=O peak at 1700 cm^{-1} from COOH of unreacted PAA binder. Upon lithiation of silicon and SiO_2 to form Li_xSi_y and Li_xSiO_y SiEI components, respectively, the FTIR spectra show a reduction of both the silicon oxide and LiPAA binder signals due to lithium lost in the formation of these SiEI species. ATR works well with smooth films but cannot measure rough films well. Because the 10-mV GenF or GenFM samples are so flaky and they show many spots of bare copper, we were unable to use ATR to measure these films. Instead, at least for 10-mV GenF, we were able to use DRIFTS to acquire a well-resolved FTIR absorption spectrum. The 10-mV GenFM sample was too degraded to measure. Additionally,

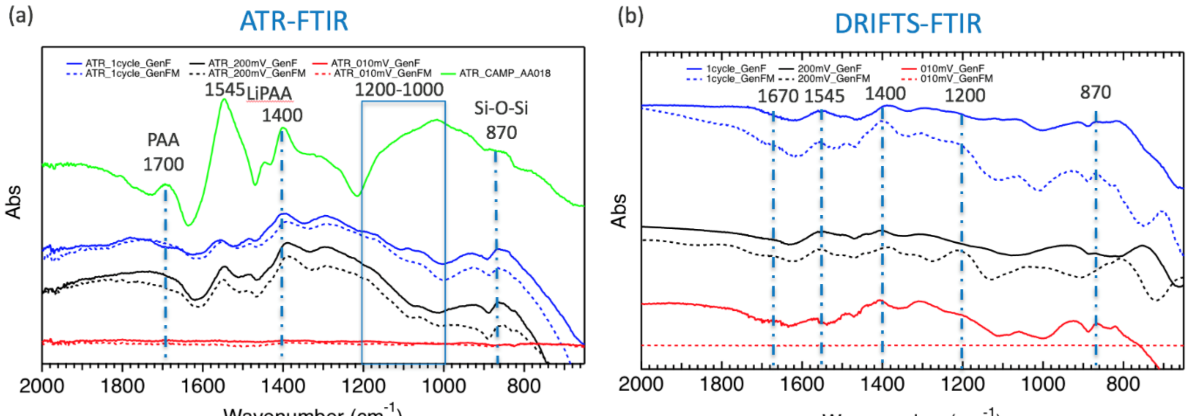

Figure 26. (a) ATR-FTIR and (b) DRIFTS-FTIR spectra of 1 cycle, 200 mV, and 10 mV GenF or GenFM samples.

the DRIFTS spectra contain two peaks, 1670 cm^{-1} and 1200 cm^{-1}, that are slightly more prominent in the GenFM, compared to GenF samples, at all potentials.

The XPS spectra of 1-cycle, 200-mV, and 10-mV GenF or GenFM samples are shown in Figure 27 and Figure 28, respectively. In all samples, the signals from PF$_6^-$ species are detected (P 2p and F 1s peaks at ~139 eV and ~689 eV, respectively), which is highly attributed to the residual electrolyte on the surface of unwashed electrodes. One major difference observed between the GenF and GenFM samples, specifically for the 200- and 10-mV ones, is found in the Si 2p spectra: there are apparent peaks from lithiated Si species (Li$_x$Si, ~98.5 eV, bright yellow) in GenF samples (200- and 10-mV lithiated ones), but it is not the case for GenFM samples. One possible explanation for this is that a surface-sensitive XPS technique cannot detect the Li$_x$Si formation in the presence of a relatively thick and well-covered SiEI layer (with possible Zintl phase) formed in GenFM electrolyte. It is noted that Raman can detect 385 cm^{-1} peaks attributed to lithium silicide (Li$_x$Si$_y$) in both 10-mV GenF and GenFM samples (Figure 25c). Another major difference in Mg 2p core level is detected in GenFM samples. The peak shape is distinctively different between 200-mV and 10-mV lithiated samples. The 1-cycle and 200-mV lithiated samples have two peaks at ~53 eV and ~52 eV, which are tentatively assigned to MgO and MgF$_2$, respectively. In the 10-mV lithiated sample, the ~53-eV peak disappears, and a new peak is observed at a lower binding energy (~50.5 eV), which is likely Mg^0. Mg(TFSI)$_2$ was eliminated from the assignment because there was not enough N 1s signal (not shown).

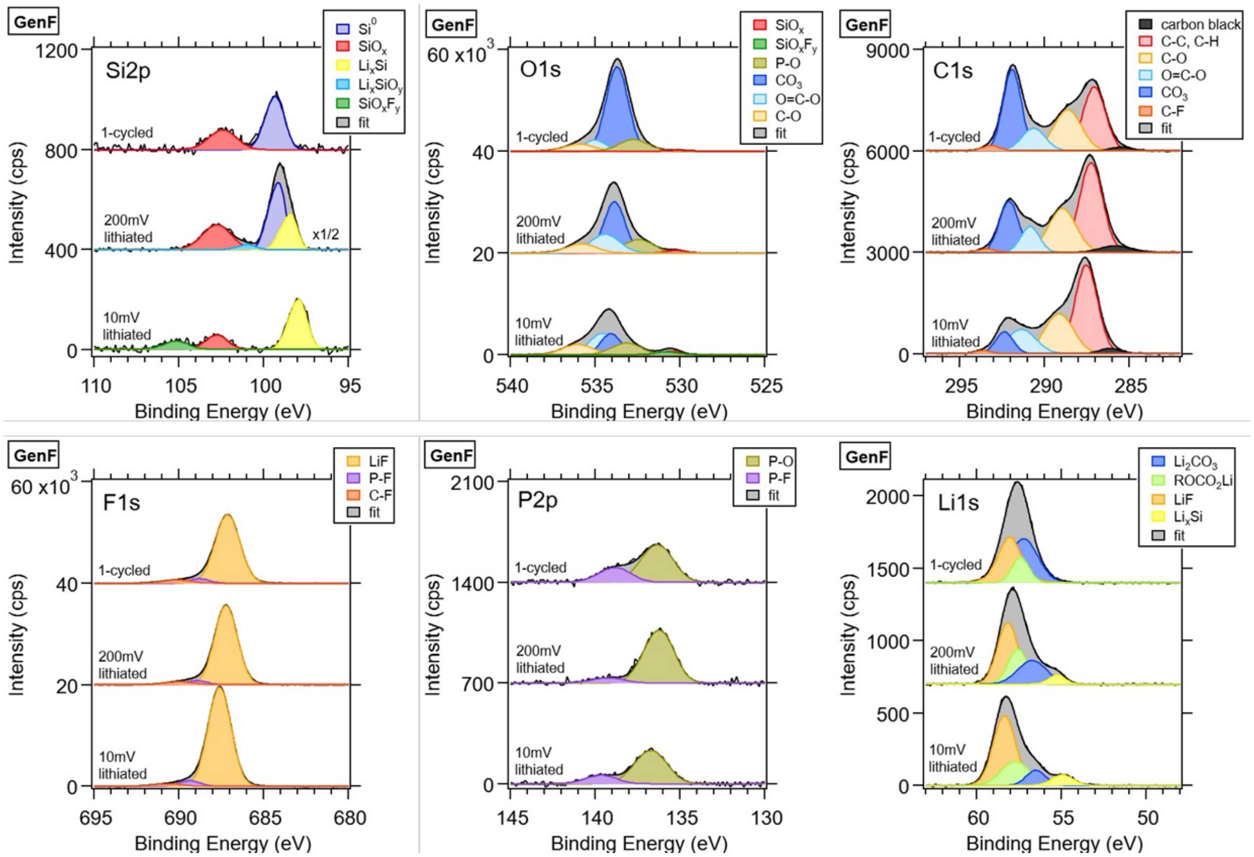

Figure 27. XPS spectra of the Si electrodes cycled in GenF. Peak assignments are preliminary.

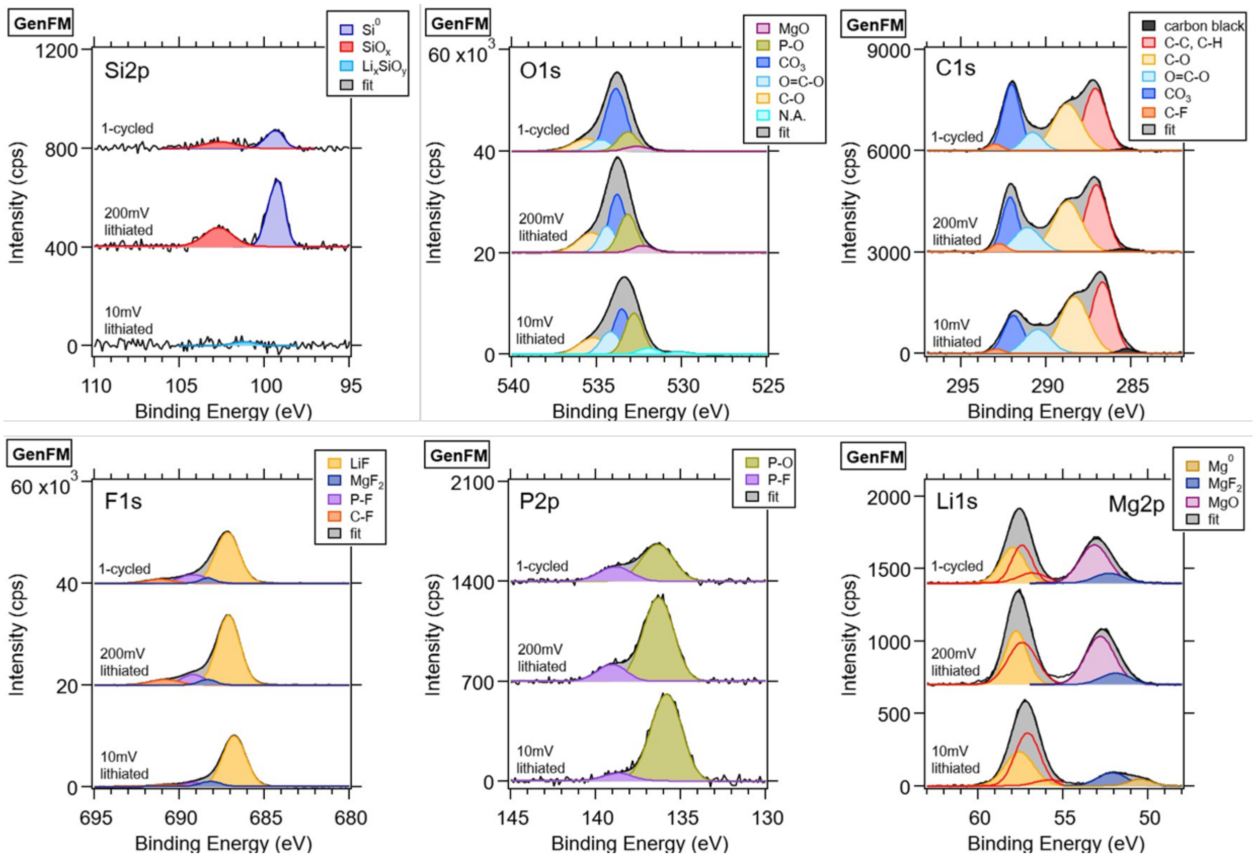

Figure 28. XPS spectra of the Si electrodes cycled in GenFM. Peak assignments are preliminary (N.A. denotes “not assigned”).

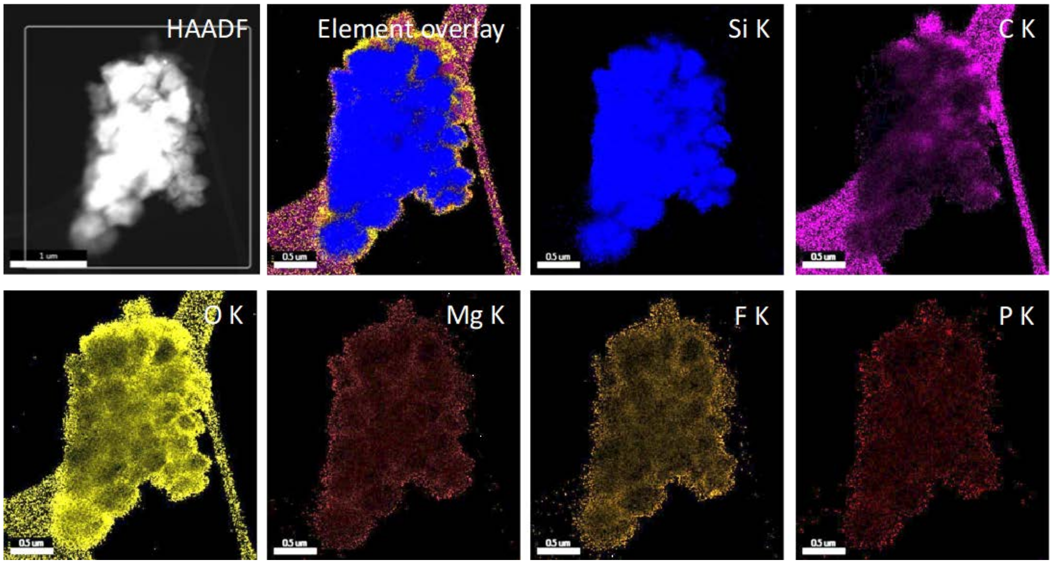

Figure 29. STEM EDS atomic % maps of particles of first-cycle GenFM sample.

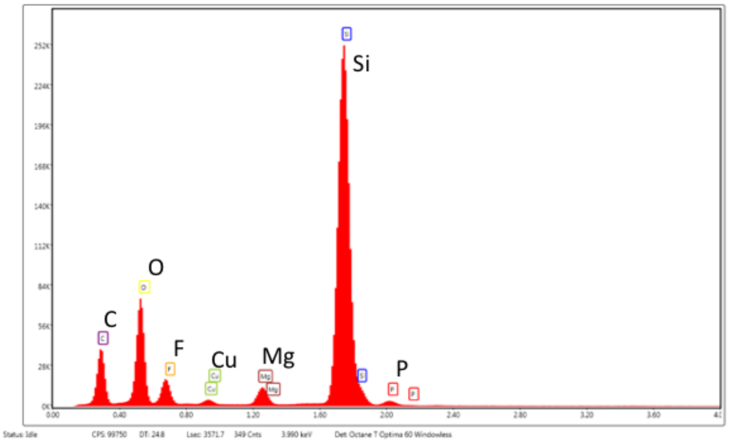

Figure 30. STEM EDS spectra obtained from particles of 1-cycle GenFM sample.

Scanning transmission electron microscopy (STEM) energy-dispersive X-ray spectroscopy (EDS) and electron energy-loss spectroscopy (EELS) analysis were performed on the first-cycle GenFM sample. A TEM sample was prepared in an Ar glove box by scraping particles of the Si-based composite electrode off the Cu foil substrate onto an ultrathin carbon support-film TEM grid. Examples of STEM EDS atomic % maps are shown in Figure 29, and the sum EDS spectra from this map area is in Figure 30. The results are consistent with Si nanoparticles being present either containing or being surrounded by a shell containing C, O, Mg, F, and P. STEM EELS analysis (not shown) revealed the presence of lithium in or around the Si particles. Areas of LiF were found to be present. STEM EELS mapping of Mg may be difficult due to the high energy of the Mg *K* edge.

Surface Morphology and Roughness of Zintl Phase. Optical microscope images obtained in the AFM instrument are illustrative of the effect of cycling (Figure 31). The 200-mV GenF or GenFM sample shows an undisturbed composite electrode because lithiation potentials were not reached under this condition. The effect of volume expansion during lithiation is seen in the sample held at 10-mV potential; large cracks appear where active material has delaminated from the underlying Cu current collector. The sample that underwent one full cycle of lithiation and delithiation shows the most damage, with diffuse cracking induced by volume contraction during delithiation.

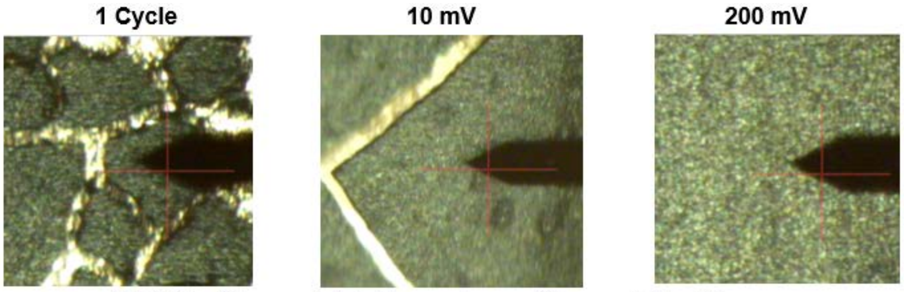

AFM Cantilever visible for scale; cantilever width=40 μm

Figure 31. Optical microscope images of composite electrodes after cycling and disassembly. Scale is visible in the width of the visible AFM cantilever, which measures 40 μm in width.

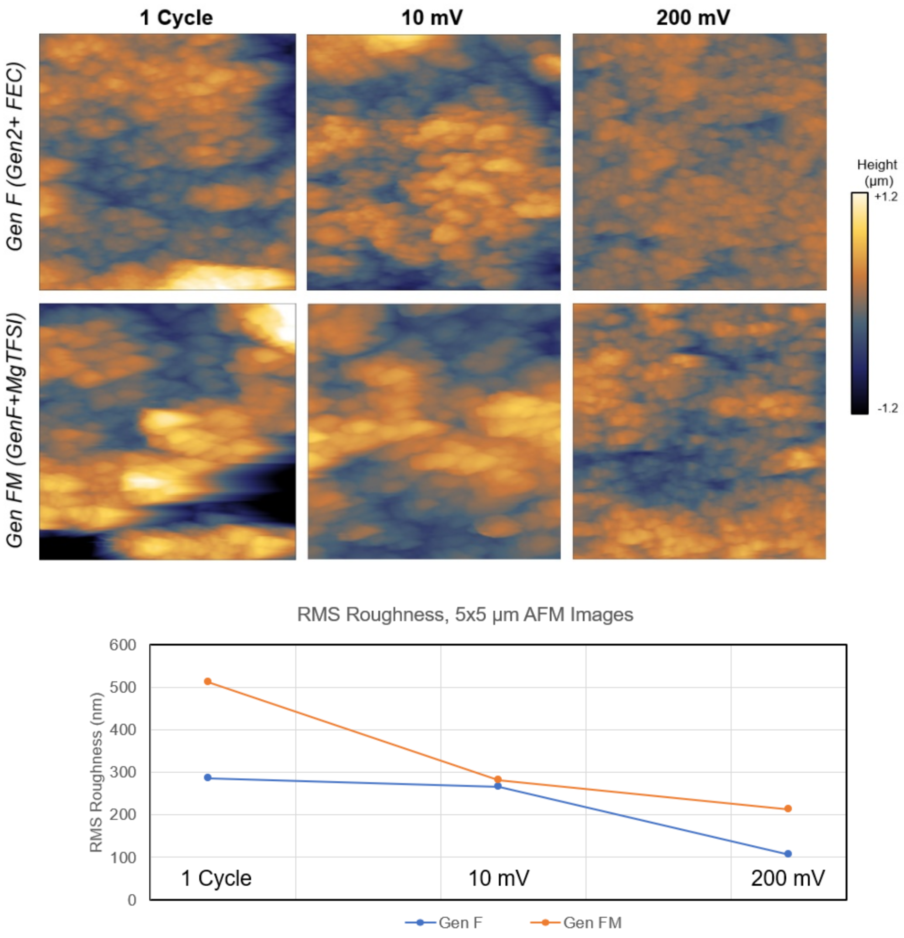

Figure 32. 5×5-µm AFM images and RMS roughness calculated from AFM images.

In Figure 32, AFM images show a rough surface, with the same trend visible in the optical microscope images (1-cycle roughness > 10-mV roughness > 200-mV roughness). Minor differences were also visible in roughness between the two sample sets, with greater roughness measured for samples cycled in GenFM electrolyte. However, with such heterogenous structures, measurements may be representative of a local area rather than the entire surface. In the future, measurements will be carried out over more locations to establish a measurement of roughness with a quantified standard deviation.

Li Beam Lithiation, Model System

All previous experiments, whether on thin film or powders, describe the interaction of Li with the Si and the oxide coating, but in the presence of electrolyte. It is clear that electrolyte decomposition plays a role in the formation and evolution of the SEI, but it was not previously possible to deconvolute the electrochemistry of electrolyte decomposition and SEI formation from the lithiation of the silica films, because they tend to occur at similar potentials in the first few cycles. Being able to independently study the process of lithium insertion into the oxide without an electrolyte or solvent present would allow us to understand the mechanisms of evolution purely of the oxide, without the salt decomposition and possible subsequent HF attack, which will give insight into the oxide layer's evolution as it accepts Li into its structure. The SEISta program has previously developed a capability to deliver Li+ ions of a given kinetic energy to the surface of an oxide or Si sample in vacuum conditions and study the resulting structure. We have named this process the virtual electrode (VE) because it does not require an electrode or metal surface to provide ion species for lithiation, instead relying on an ion beam to deliver these species to the surface.

A variant of the VE technique that uses a galvanostatic titration (GITT) technique, VE-GITT XPS measurements on a 5-nm SiO_2 / Si(001) wafer sample are summarized in Figure 33. On the as-received, pre-lithiation sample, the Si 2p core-level spectrum shows features associated with SiO_2 (~104.0 eV) and Si_0 (~99.0 eV). Corresponding features are observed in the valence-band spectrum: the Si_0 and SiO_2 valence-band maxima (VBMs) appear at ~0.5 eV and 5.5 eV, respectively. The relative peak heights of these Si 2p features are consistent with an SiO_2 thickness on the order of 5 nm, and the single core level in the O 1s spectrum (O 1s to Si 2p ΔBE ~429.1 eV) supports the SiO_2 phase assignment. As observed previously, application of Li^+ current bias (middle row of spectra in Figure 33) causes an immediate shift to higher binding energies (BEs) for all core levels. Initially, the Si_0 peak shifts to higher BE by ~ 0.9 eV, and this effect is attributed to the introduction of substantial downward band bending in the Si(001) wafer, initially caused by the transient accumulation of positive charge (Li^+ ions) on the free surface, and at later times by a shift in near-surface doping of the Si(001) from p- to n-type. A similar shift can be discerned in the VBM associated with the Si_0 region of the VB spectra.

The applied Li^+ current bias produces substantially larger BE shifts (~2.5 eV) in the SiO_2 features for the O 1s, Si 2p, and VB spectra in Figure 33. In part, these shifts are due to the fact that the potential at the surface of the SiO_2 layer rides atop that of the underlying Si(001) layer. As a result, the potential shift across the SiO_2 layer is additive to that of the Si(001) substrate, and consequently, one can infer that the potential difference across the SiO_2 layer is ~1.6 V. This value is significant in that it represents the overpotential (i.e., quasi-equilibrium magnitude of the potential difference) required to drive Li+ migration through the SiO_2 layer.

Also clearly seen in Figure 33 is the appearance and growth of spectral features associated with an Li_ySiO_x phase. This phase forms via the reaction SiO_x + yLi+ + ye- → Li_ySiO_x, and therefore, it represents a mechanism for transformation of the relatively resistive SiO_2 phase into less-resistive Li_ySiO_x. Lastly, comparison of core-level BEs acquired with vs. without Li^+ current bias (middle- vs. bottom-row spectra in Figure 33) shows how overpotential evolves over the course of lithiation.

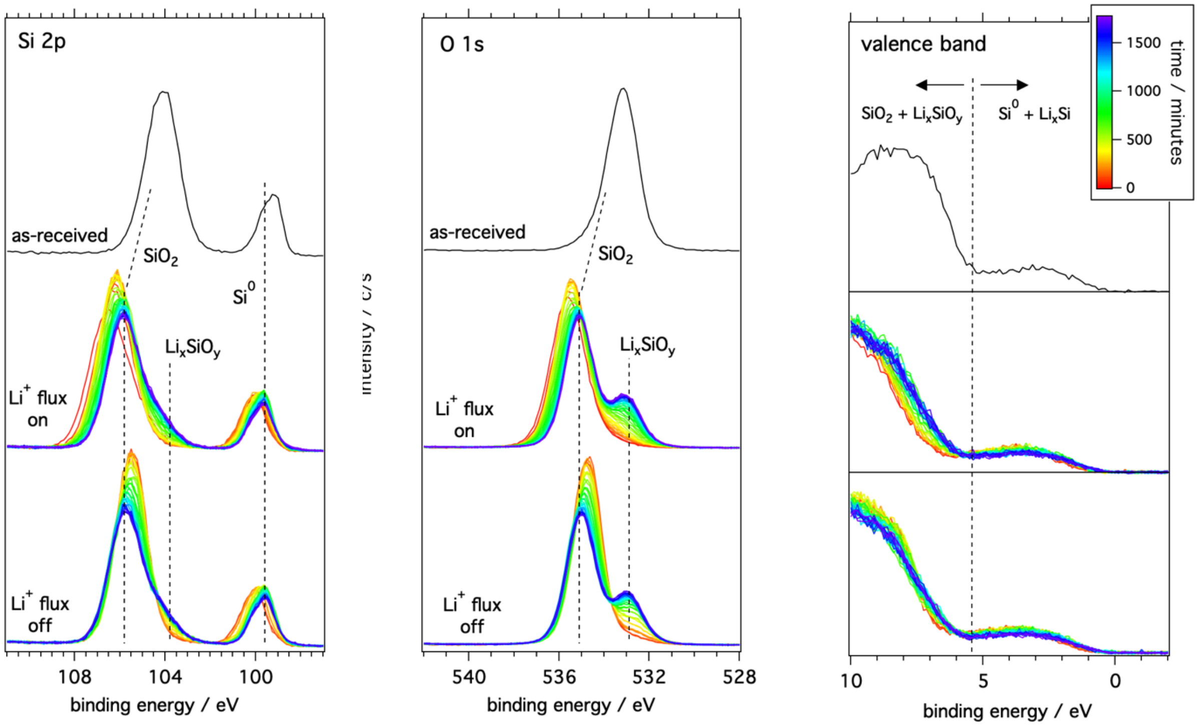

Figure 33. Summary of XPS measurements for the O 1s, Si 2p, and valence-band (VB) regions during *in situ* lithiation of 5-nm SiO_2 / Si(001) sample. For these measurements, the Li+ ion gun was pulsed (square wave, 50% duty cycle) at 200 μHz with a current density ~55 nA/cm^2. The top row represents core-level spectra from the as-received sample. The middle and lower rows show spectra acquired when the Li+ ion gun was on and off, respectively. The dashed vertical lines are a guide to the eye to illustrate core-level shifts associated with the lithiation overpotential.

The time evolution of the overpotential associated with conversion of SiO_2 to Li_ySiO_x is summarized in Figure 34. In the top panel of Figure 34 (a), the O 1s BE from the SiO_2 phase is plotted vs. time. The SiO_2 O 1s BE toggles between high and low values as the flux of Li^+ ions pulses on and off. The lower panel of Figure 34 (a) shows how the difference in upper and lower BEs changes with time: initially (~ 0–200 s), the overpotential is nearly constant at ~ 0.7 V, but thereafter, the magnitude decreases monotonically. Figures 34 (b)–(f) show sets of spectra at various time over the course of the *in situ* lithiation experiment. In each case, several spectra each are shown for the Li^+ flux off and on conditions, and the relative shifts in these spectra directly reveal the evolution in the lithiation overpotential as SiO_2 is progressively converted to Li_ySiO_x. The effect of this phase conversion on overpotential is dramatic—whereas initially the overpotential is ~ 0.7 eV, it eventually drops to ~0.05 eV.

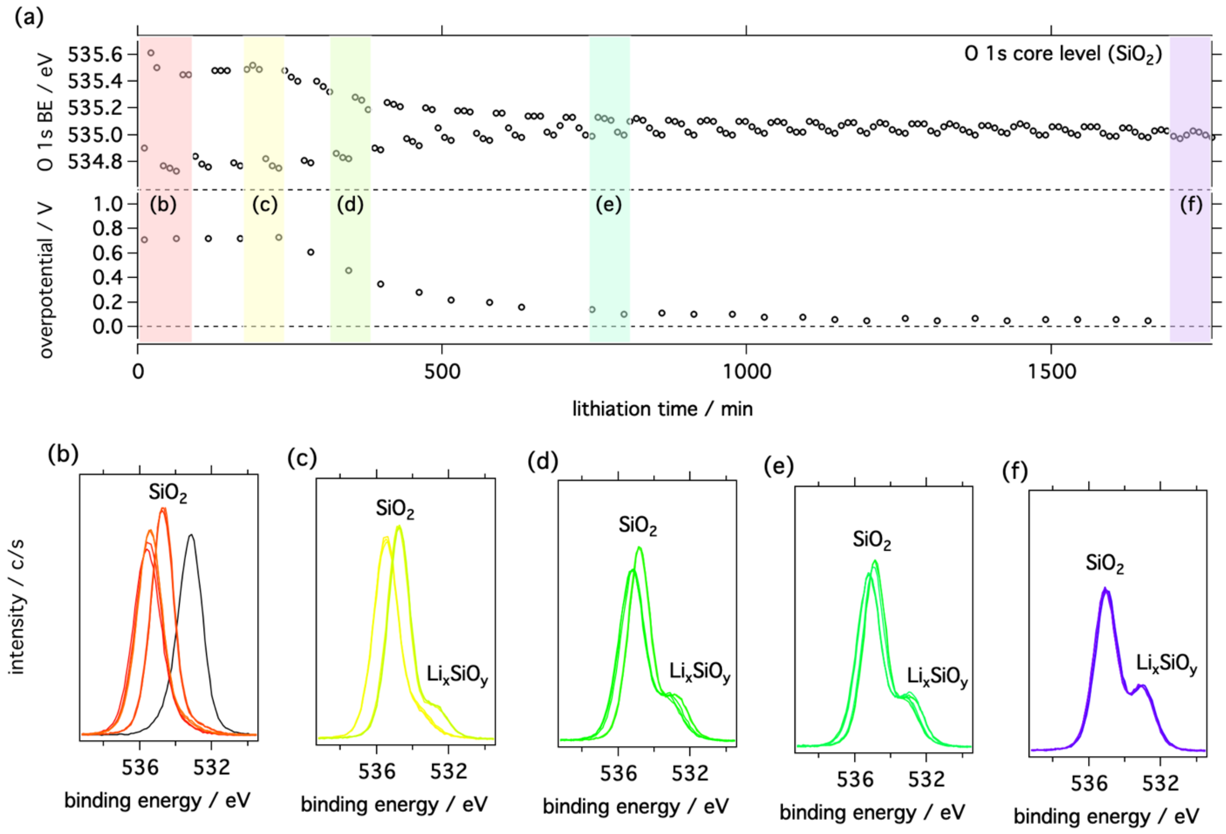

Figure 34. (a) Summary of time evolution of SiO_2 O 1s binding energy and overpotential during VE-GITT (i.e., the pulsed *in situ* lithiation experiment). (b)–(f) O 1s core-level spectra at various times illustrating that the core-level shifts associated with the overpotential become progressively smaller in magnitude as the lithiation proceeds. (Note that the black trace in (b) corresponds to the initial, pre-lithiated state.)

Another interesting feature revealed in the evolution of XPS spectra during the early stage of lithiation is that all spectral features associated with both Si0 and SiO_2 shift to substantially higher BE as soon as the Li+

current bias is applied, and thereafter, they never return to initial values, even after the current bias has been turned off. Figure 35 compares spectra from the as-received, pre-lithiated sample to those after the first half-cycle of the VE-GITT XPS experiment. Focusing first on the Si0 features (Si 2p peaks ~99.0–100.0 eV, and VBMs ~0.0–1.0 eV), from these shifts as noted previously we can infer that the initial effect of lithiation is to induce substantial downward band bending, ~0.9 eV, in the Si(001) near the free surface. This observation is consistent with conversion of the near-surface silicon from p-type to n-type, presumably due to near-degenerate doping by Li, which acts as a shallow donor. On the other hand, the SiO_2 features (O 1s peaks ~533.0–535.0 eV, Si 2p peaks ~105.0–107.0 eV, and VBMs ~5.0–7.0 eV) shift to higher BE by ~1.6 eV. The fact that lithiation results in larger shifts in the SiO_2 relative to the Si0 features can only be explained by a change in the interfacial valence-band offset (VBO) between SiO_2 and Si(001)—from 5.1 eV to 5.8 eV—as illustrated in Figure 36. We speculate that the change in VBO is a result in a change in the SiO_2 / Si(001) interfacial dipole, possibly as a result of changes in chemical bonding at this interface associated with the introduction of Li^+ ions. For example, Li^+ might effectively passivate Si dangling-bond states at this interface.

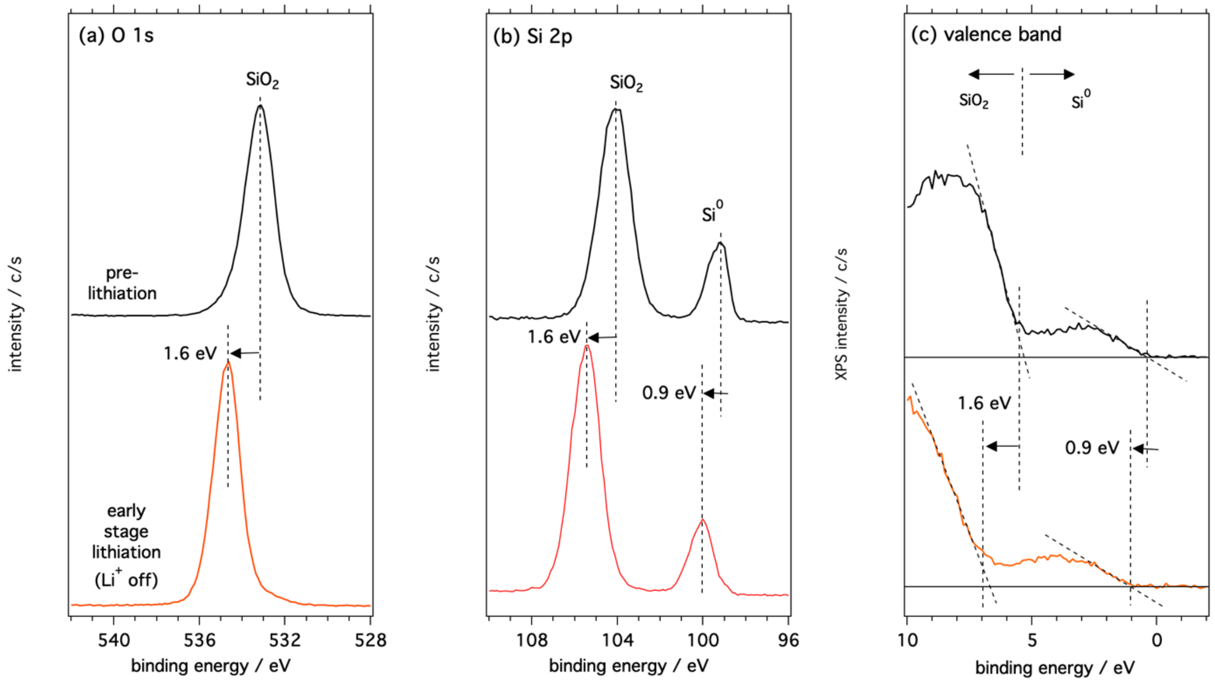

Figure 35. (a) XPS spectra from the (a) O 1s and (b) Si 2p core levels, as well as the (c) valence-band regions. The top row of spectra (black traces) show spectra from the pre-lithiated sample. The Si 2p and VB spectra both show clear features associated with both SiO_2 and SiO, whereas the O 1s spectra each show a single feature associated with SiO_2. O 1s. The bottom row of spectra (red traces) shows the sample at an early stage of lithiation (cf. Figures 34(b) and (c)) with the Li+ ion gun in the off state.

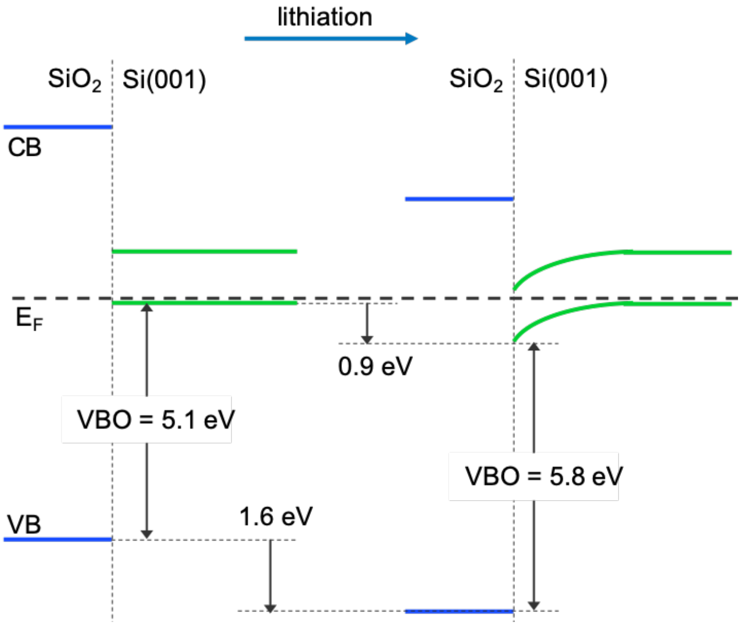

Fig. 36. Schematic illustration of the observed change in interfacial band alignment that occurs during early-stage lithiation of the 5-nm SiO_2 / Si(001) model-system interface.

Conclusions

Our studies show that an amorphous oxide layer is preferred over a crystalline oxide in early stages of film growth; however, after ~0.3 nm, the crystalline film is thermodynamically favored. The fact that amorphous oxide films are observed in nm-thick SiO_2 suggests that the crystallization of the early-stage oxide is kinetically hindered, and the growth conditions favor the amorphous configuration. Additionally, we observe that the onset of lithiation in Si and SiO_2 films occurs at higher potentials than for bulk material.

We note that a strong dependence of lithiation on SiO_2 thickness is observed in both cycling and chronoamperometric measurements. Below 3.0-nm SiO_2, lithiation on cycling is homogeneous and occurs with high Coulombic efficiency, and holding at 0.01 V_{Li} leads to a rapid current rise that reaches steady state in under 24 h, ultimately yielding uniform lithiation. Conversely, above 3.0-nm SiO_2, initial lithiation upon both cycling and holding at 0.01 V_{Li} is very inhomogeneous, occurring at pinholes first and then spreading radially, decreasing the resistance to further lithiation as the process proceeds. This also exhibits, as exponentially in time, rising current at 0.01 V_{Li}. The thickness dependence of peak currents in CV suggests an effect of tunneling through the SiO_2 on reaction kinetics.

We note that lithiated silica tends to have lower onset potentials than unlithiated oxide, and that the onset potential scales with the degree of lithium content in the oxide film. Additionally, conductivity of the films increases with lithium content, leading to lower overpotentials for lithiation into the underlying silicon.

Localized lithiation proceeds through SiO_2 pinholes, local decrease in SiO_2, and Li spreading beneath SiO_2. Li spreads hundreds of microns or even millimeters near the Si/SiO_2 interface, whereas diffusing only a few microns in the depth of the Si wafer. This suggests very significant interfacial diffusion enhancement for Li, which could be used for battery and electrode applications.

SiO_x anodes with high oxygen content appear to form lithium silicates irreversibly during the first lithiation process. The formation of lithium silicates may suppress the electrolyte decomposition at low potential; however, it also leads to a lower first-cycle Coulombic efficiency due to its irreversibility. Raising oxygen content in the Si anode could improve its cycling performance; however, it is at the cost of lowering its reversible capacity.

The capacity fade rate of SiNP-based anodes displays a size-dependent relationship with the smallest-diameter (<10-nm) Si NPs exhibiting the best capacity retention (>99.9% CE). SiO_2 surface layers on Si NPs do not appear to affect the capacity fade rate. The capacity fade-rate trend appears to scale with the surface-area-to-volume (SA/V) ratio, indicating that both mechanical and chemical aspects may be responsible for the capacity fade. Impedance spectroscopy analysis shows significant differences in the SEI layers between Si NPs with and without surface oxidation. Despite a slower Li+ conduction mechanism through the SEI formed on top of SiO_2-terminated Si NPs, lithiation rates are still determined by Li+ diffusion in silicon, not through the SEI.

The voltage- and time-dependent formation (e.g., potentiostatic hold at specific voltage until $i \leq 5.0\times10^{-6}$ and/or one cycle at the voltage range of 1.5–0.01 V) and the chemical and physical nature, such as chemical composition, surface morphology, and roughness, of the Li-Mg-Si ternary phase were characterized using a variety of analytical techniques. From both spectroscopic analyses, we did not observe any specific differences between GenF and GenFM samples in terms of chemical composition; but XPS analysis revealed the possible presence of MgO (O 1s), MgF_2 (F 1s), and $Mg^0/MgF_2/MgO$ (Mg 2p) that may be originated from the Li-Mg-Si ternary Zintl phase. In addition, the STEM EDS atomic % maps and the corresponding sum EDS spectra are shown with Si nanoparticles being present either containing or being surrounded by a shell containing C, O, Mg, F, and P. From the Si 2p XPS spectra (in particular, from availability of Li_xSi peak), we could assume that a relatively thick and well-covered SiEI layer (with possible Zintl phase) is formed in GenFM electrolyte, which may be correlated with relatively greater roughness of 200-mV, 10-mV, and 1-cycle GenFM samples from AFM analysis. To obtain a better understanding of detailed formation mechanism of the Zintl phase, we have a plan to study a Si wafer as a model electrode without additional electrode elements (e.g., conductive carbon and binder).

The novel technique VE-GITT XPS was developed and applied to study effects of lithiation on 5-nm SiO_2 / Si(001) wafer model-system anodes. Key results of these experiments include the following: As previously reported, surface silicon oxides are converted to silicate phases according to $SiOx + yLi^+ + ye^- \rightarrow Li_ySiO_x$. Lithiation leads to a dramatic reduction of the overpotential for 5-nm SiO_2 from >0.7 V to ~0.05 V. The evolution of Li^+ current-bias-induced BE shifts in the SiO_2 XPS peaks enable a direct correlation between lithiation overpotential and the extent of SiO_2 to Li_ySiO_x conversion. Lithium incorporation leads to a change in near-surface doping of the Si(001) wafer from p- to n-type. Lithiation changes the magnitude of the SiO_2/Si(001) interfacial dipole by ~0.7 eV, which, in turn, shifts the valence-band offset from 5.1 eV to 5.8 eV.

References

[1] B. Han, C. Liao, F. Dogan, S.E. Trask, S.H. Lapidus, J.T. Vaughey, B. Key, Using Mixed Salt Electrolytes to Stabilize Silicon Anodes for Lithium-Ion Batteries via in Situ Formation of Li-M-Si Ternaries (M = Mg, Zn, Al, Ca). ACS Appl. Mater. Interfaces 11, 29780–29790 (2019).
[2] K.N. Wood et al., Comm. 9, 2490 (2018).
[3] A. Zur, T.C. McGill, Lattice match: An application to heteroepitaxy. J. Appl. Phys. 55, 378–386 (1984).
[4] M. Aykol, K.A. Persson, ACS Appl. Mater. Interfaces 10, 3039–3045 (2018).
[5] X. Chen, P.M. Vereecken. Solid and Solid-Like Composite Electrolyte for Lithium Ion Batteries: Engineering the Ion Conductivity at Interfaces. Adv. Mater. Interfaces 6, 1800899 (2019).

[6] M. Schnabel, S. Harvey, E. Arca, G. Teeter, C. Ban, P. Stradins. Lithiation of Oxidized Silicon. Talk at the ECS conference (May 2019); Journal paper in preparation.

[7] Y. Xu, C. Stetson, K. Wood, E. Sivonxay, C. Jiang, G. Teeter, S. Pylypenko, S.D. Han, K.A. Persson, A. Burrell, A. Zakutayev, Mechanical Properties and Chemical Reactivity of Li_xSiO_y Thin Films. ACS Appl. Mater. Interfaces 10, 38558 (2018).

[8] Y. Xu, K. Wood, J. Coyle, C. Engtrakul, G. Teeter, C. Stoldt, A. Burrell, A. Zakutayev, Chemistry of Electrolyte Reduction on Lithium Silicide. J. Phys. Chem. C 123, 13219 (2019).

[9] R. Kumar, A. Tokranov, B.W. Sheldon, X.C. Xiao, Z.Q. Huang, C.Z. Li, T. Mueller, In Situ and Operando Investigations of Failure Mechanisms of the Solid Electrolyte Interphase on Silicon Electrodes, ACS Energy Lett. 1, 689 (2016).

[10] C.Y. Dai, C.S. Li, H.Y. Huang, Z. Wang, X.X. Zhu, X.B. Liao, X. Chen, Y. Pan, D.N. Fang, In Situ Strain Measurements and Stress Analysis of SiO@C Composite Electrodes during Electrochemical Cycling by Using Digital Image Correlation, Solid State Ionics 331, 56 (2019).

[11] R. Kumar, P. Lu, X.C. Xiao, Z.Q. Huang, B.W. Sheldon, Strain-Induced Lithium Losses in the Solid Electrolyte Interphase on Silicon Electrodes, ACS Appl Mater Inter. 9, 28406 (2017).

[12] F. Paloukis, C. Elmasides, F. Farmakis, P. Selinis, S.G. Neophytides, N. Georgoulas, J. Power Sources 331, 285–292 (2016).

[13] S.L. Randzio, J. Suurkuusk, A.E. Beezer (Ed.). Biological Microcalorimetry, Academic Press, pp. 311–341 (1980).

[14] L.J. Krause, L.D. Jensen, J.R. Dahn. J. Electrochem. Soc. 159, A937–A943 (2012).

[15] L.M. Housel et al. ACS Appl. Mater. & Interfaces, accepted (2019).

[16] T. Gruber, D. Thomas, C. Röder, F. Mertens, J. Kortus, Raman spectroscopic studies of LixSiy compounds. Journal of Raman Spectroscopy 44 (6), 934–938 (2013).

[17] R.E. Ruther, K.A. Hays, S.J. An, J. Li, D.L. Wood, J. Nanda, Chemical Evolution in Silicon–Graphite Composite Anodes Investigated by Vibrational Spectroscopy. ACS Applied Materials & Interfaces 10(22), 18641–18649 (2018).

Part 2: Origins of Si/Electrolyte Interface Stability

I. Hasa, E. Arca, S. Jurng, L. Zhang, P. Ross, G. Liu, R. Kostecki (LBNL), Y. Ha, C. Stetson, S. Harvey, G. Teeter, B. Tremolet de Villers, C.-S. Jiang, M. Al-Jassim, S.-D. Han, Y. Yin, A. Norman, M. Al-Jassim, (NREL), G. Yang, G. Veith, and J. Nanda (ORNL)

Background

The primary objective of our effort is to understand the processes occurring at the silicon/electrolyte interface (SEI). The reductive decomposition of the electrolyte in lithium-ion systems employing silicon anodes is inevitable because the working potential of the electrode is far below the electrochemical stability window of the electrolyte components. In principle, the insoluble decomposition products should precipitate on the electrode surface and result in the formation of a passivating film that suppresses further electrolyte decomposition [1,2]. However, cycling performance is adversely impacted by the inherent instability of the silicon/electrolyte interface and the mechanical instability of the electrodes, which, upon alloying with lithium, experience a huge volume expansion and consequent cracking [3]. A better understanding of the kinetic processes occurring upon cycling will enable an efficient implementation of silicon-based electrodes in high-performance lithium-ion batteries.

To accomplish this, two model systems were used: the first consisting of thin-film electrodes, the second consisting of Si wafers. For the thin-films studies, we address the inherent non-passivating behavior of silicon model electrodes in organic electrolytes by studying the corrosion behavior and thus the evolution of the SEI as a function of cycling. In addition to understanding the fundamental shortcomings of carbonate-based electrolyte for the Si anode, we explored Glyme-based electrolyte, a potential alternative to Gen2 electrolyte and compare the performance and reactivity of the two electrolyte systems.

Likewise, for the Si-wafers model, cracking is a well-understood limitation, but the evolution of a solid-electrolyte interphase (SEI) through cycling is not fully understood, yet it plays a fundamental role in understanding of SEI stability of Si anodes. By applying microscopic and spectroscopic methods to this two-dimensional (2D) model system, we were capable of producing valuable insight into the characteristics of the SEI and its development over the lifetime of the anode material. We further investigate the role of water, a contaminant that potentially can be introduced during the battery manufacturing process. Specifically, we assessed how 50 ppm of water affects the SEI stability and evolution.

Finally, we investigate the role of carbon coatings on the stability of the SEI using nanoparticles as a model system and the use of gradient polarity solvent wash to remove sequentially different SEI components from electrode surfaces to help their precise identification.

Corrosion Task: Role of Lithium Salts on the Passivation Behavior of Si/Electrolyte Interface

The “Corrosion Task” is a coordinated research effort to provide a basic understanding and effective ways to mitigate the corrosion of Si anodes in organic carbonate-based electrolytes. For this task, Oak Ridge National Laboratory fabricated all model electrodes, the team at Lawrence Berkeley National Laboratory (LBNL) electrochemically investigated the corrosion currents involved upon cycling, and samples were further characterized in a joint-effort at LBNL and the National Renewable Energy Laboratory (NREL).

Firstly, we defined the electrochemical protocols to be employed to determine the corrosion currents. Two different electrochemical protocols have been established involving galvanostatic tests followed by chronoamperometry measurements, both in potentiostatic mode at fixed voltage values (Protocol 1), and at open-circuit voltage conditions (Protocol 2). A schematic of the electrochemical cell and a description of the two protocols is given in Figure 1.

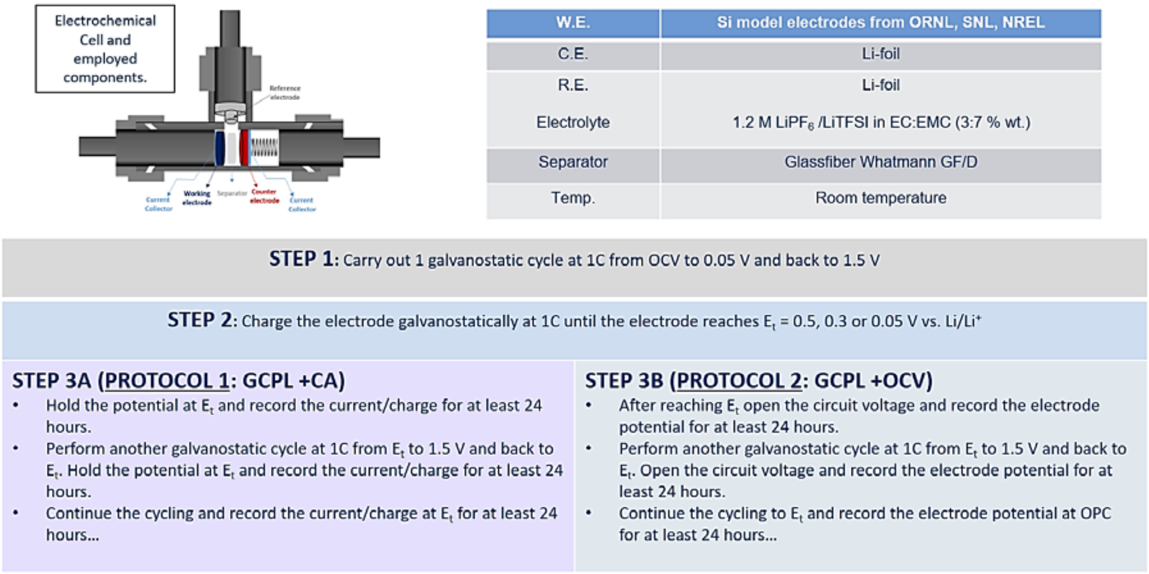

W.E.	Si model electrodes from ORNL, SNL, NREL
C.E.	Li-foil
R.E.	Li-foil
Electrolyte	1.2 M $LiPF_6$ /LiTFSI in EC:EMC (3:7 % wt.)
Separator	Glassfiber Whatmann GF/D
Temp.	Room temperature

STEP 1: Carry out 1 galvanostatic cycle at 1C from OCV to 0.05 V and back to 1.5 V

STEP 2: Charge the electrode galvanostatically at 1C until the electrode reaches E_t = 0.5, 0.3 or 0.05 V vs. Li/Li$^+$

STEP 3A (PROTOCOL 1: GCPL +CA)

- Hold the potential at E_t and record the current/charge for at least 24 hours.
- Perform another galvanostatic cycle at 1C from E_t to 1.5 V and back to E_t. Hold the potential at E_t and record the current/charge for at least 24 hours.
- Continue the cycling and record the current/charge at E_t for at least 24 hours…

STEP 3B (PROTOCOL 2: GCPL +OCV)

- After reaching E_t open the circuit voltage and record the electrode potential for at least 24 hours.
- Perform another galvanostatic cycle at 1C from E_t to 1.5 V and back to E_t. Open the circuit voltage and record the electrode potential for at least 24 hours.
- Continue the cycling to E_t and record the electrode potential at OPC for at least 24 hours…

Figure 1. Schematic representation of the electrochemical cell set up, cell components, and protocols employed in the Corrosion Task.

Several configurations were tested using the developed Protocol 1 (GCPL + CA) to determine the residual currents after every lithiation, as described in details in the FY19 Q1 quarterly report. The results indicate that almost one third of the current values observed are associated with the copper piston, most likely due to the large surface area of copper exposed to the electrolyte in T-cell configuration. To find a more suitable substrate involving less exposed surface area, different copper substrates have been tested. A schematic representation of the investigated substrates and the residual current values observed after the 1st cycle by appling Protocol 1 are reported in Table 1.

Table 1. Copper-based substrates investigated with Protocol 1. The values of the residual current observed after 24 hours of potentiostatic step at 0.05 V are reported. The thin copper foil presents the lower values on the order of 1 µA cm^{-2}.

Substrate	 Cu piston	 Cu piston + protective plastic	 Cu thick disk	 Cu foil
Residual Current after 1st cycle	2.7 µA cm^{-2}	1.8 µA cm^{-2}	2.6 µA cm^{-2}	1.0 µA cm^{-2}

Copper foil (12-mm diameter) presented the smaller residual current values. Accordingly, the first model electrode of choice for the evaluation of the corrosion currents has been identified as: 500-nm amorphous silicon (with 3-nm native oxide) deposited on copper foil (500-nm Si + 3-nm SiO_2 on Cu). The 500-nm Si thin film has been investigated in four electrolyte solutions, i.e., 1.2 M $LiPF_6$ EC:EMC (3:7 wt%), 1.2 M $LiPF_6$ EC:EMC (3:7 wt%) + 10%wt. FEC, 1.2 M LiTFSI EC:EMC (3:7 wt%), and 1.2 M LiTFSI EC:EMC (3:7

wt%) + 10%wt. FEC. The electrochemical characterization has been performed both in terms of cyclic voltammetry and galvanostatic cycling test as reported in Figure 2.

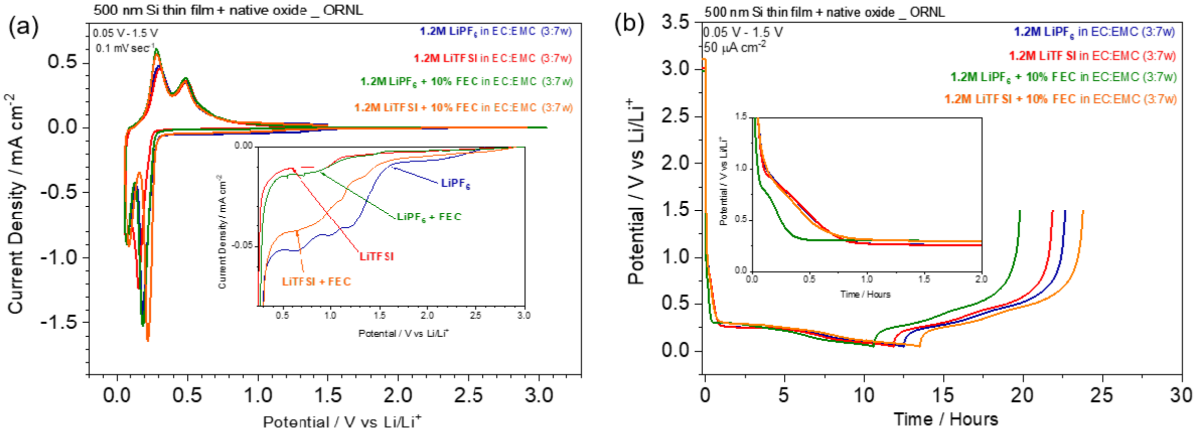

Figure 2. (a) First lithiation–delithiation process of 500-nm Si thin film on Cu foil observed by cyclic voltammetry by using four different electrolyte solutions. A scan rate of 0.1 mV s^{-1} has been applied within the 0.05–1.5 V potential range. Inset shows the enlarged potential region of the electrolyte decomposition. (b) Galvanostatic cycling test of the same systems performed at 50 μA cm^{-2}.

Interestingly, the inset of Figure 2 reports the current values involved during the electrolyte decomposition process occurring before lithiation. The $LiPF_6$-based electrolyte presents the largest reductive current density, whereas the presence of FEC and the substitution of $LiPF_6$ with LiTFSI strongly reduce the current involved in the process.

The observation has been confirmed by galvanostatic cycling test reported in Figure 2(b). Indeed, the first Coulombic efficiency has been calculated to be: 81.4%, 84.3%, 86.5%, and 75.8%, respectively, for the 1.2 M $LiPF_6$ EC:EMC (3:7 wt%), 1.2 M $LiPF_6$ EC:EMC (3:7 wt%) + 10% FEC, 1.2 M LiTFSI EC:EMC (3:7 wt%), and 1.2 M LiTFSI EC:EMC (3:7 wt%) + 10% FEC electrolyte solutions. Protocol 1 (GCPL + CA) has been applied to the above-mentioned system to understand and evaluate the effect of different salts ($LiPF_6$ vs LiTFSI) and the effect of the additive (10% wt. FEC) on the passivating properties of silicon.

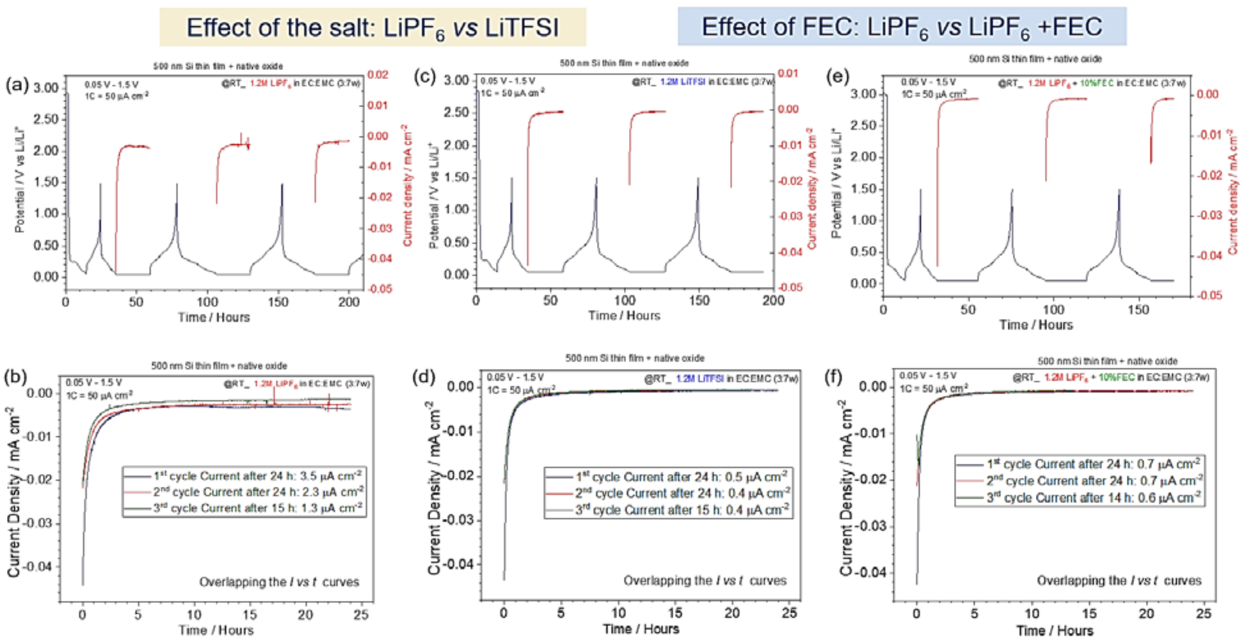

Figure 3. Application of Protocol 1 (GCPL + CA) to the 500-nm Si thin-film model electrode by using (a, b) 1.2 M $LiPF_6$ EC:EMC (3:7 wt%), (c, d) 1.2 M $LiPF_6$ EC:EMC (3:7 wt%) + 10% FEC, and (e, f) 1.2 M LiTFSI EC:EMC (3:7 wt%). (a, b, c) show the galvanostatic cycling with associated potentiostatic step at 0.05 V. (b, d, f) reports the related current-density measurement during the potentiostatic step.

Figure 3 reports the galvanostatic cycling tests and the I vs t curves obtained during the constant voltage step at 0.05 V in three different electrolytes. Interestingly, the residual current detected after 24 hours at 0.05 V are very large for the 1.2 M $LiPF_6$ EC:EMC (3:7 wt%) electrolyte, whereas by substituting $LiPF_6$ with LiTFSI, the current value is about 7 times smaller. The same effect is observed with the addition of 10% FEC to the bare 1.2 M $LiPF_6$ EC:EMC (3:7 wt%) solution. The data are in agreement with the CV and GCPL tests reported in Figure 2. It is also observed that the passivation of silicon improves upon cycling, as demonstrated by the lower current values observed after the third potentiostatic step when compared to the first one.

The same kind of analysis has also been conducted to investigate other effects on the corrosion currents and passivating properties of silicon. The investigated effects include: 1) the state of charge at which the potentiostatic step is applied (0.5 V *vs* 0.05 V); 2) the effect of the silicon thickness (500-nm Si *vs* 50-nm Si, cracking effect of silicon upon cycling); and 3) the effect of the surface silicon oxide layer on silicon, which has also been investigated by applying protocol 2 (GCPL + OCV) (3-nm native SiO_2 *vs* 10-nm sputtered SiO_2). All the investigated effects and related conclusions are summarized in Table 2.

Table 2. Summary of the Investigated Effects on the Passivating Properties of Silicon and Preliminary Conclusions.

Investigated Effects	Conclusion
Effect of the salt: $LiPF_6$ vs LiTFSI	LiTFSI-based electrolytes exhibit lower residual currents
Effect of additives: 10% wt. FEC addition	FEC improves the passivation properties of Si

Effect of the state of charge on corrosion current: 0.5 V vs 0.05 V	Larger currents are observed at 0.05 V than 0.5 V
Effect of silicon thickness: 500 nm vs 50 nm Si decoupling cracking effect from catalytic activity of Si	The cracking effect is responsible of about 60% of the parasitic currents observed in fully lithiated state
Effect of SiO_2 on passivating behavior	SiO_2 inhibits passivation of silicon surface

The 50-nm films with 3-nm and 10-nm SiO_2, respectively, were further analyzed. Galvanostatic cycling was performed by applying a constant current of 5 μA cm^{-2} within the 0.05–1.5 V potential range in a three-electrode Swagelok T-type cell, using Gen 2 electrolyte (1.2M $LiPF_6$, EC:EMC 3:7 wt.%). Following galvanostatic testing, samples were rinsed with DEC, packaged and shipped to the National Renewable Energy Laboratory (NREL) for X-ray photoelectron spectroscopy (XPS) measurements. At NREL, samples were transferred from an argon-filled glove box into the XPS analysis chamber via an ultrahigh-vacuum transport pod to avoid exposure to ambient atmosphere. XPS measurements were performed in a Kratos Axis Nova instrument.

XPS measurements on the 50-nm a-Si / 3-nm SiO_x sample are summarized in Figure 4. XPS datasets were analyzed using a method previously developed in the SEISta project, where phases are identified by constraining elemental ratios and binding-energy separation (ΔBE) values for all core-level peaks in a particular phase [4]. Initially, during the first lithiation (1.5 V), XPS spectra primarily showed the presence of SiO_x (Si 2p and O 1s peaks at ~105 eV and 534.2 eV, respectively), as well as the underlying Si^0 (Si 2p peak at ~99.5 eV). Additionally, there appears to be a small amount of Li_ySiO_x present even at 1.5 V. As the first lithiation proceeds down to 0.05 V, the most striking changes include the appearance and growth of peaks associated with Li_2CO_3, Li_3PO_4, LiF, and a P-F-containing species. The P-F species is revealed by F 1s and P 2p peaks (~690.5 eV and ~138 eV, respectively) that are strongly correlated with respect to both ΔBE values and peak-intensity ratios. The existence of $(PF_6)^-$ (or $LiPF_6$) as a candidate to explain the observed P-F features is tentatively ruled out, because the observed F 1s –to – P 2p ΔBE values (~553 eV) do not match the expected value for $LiPF_6$ (~552 eV). Also, the observed peak intensity ratios F/P are too low to be consistent with $(PF_6)^-$; therefore, we tentatively assign these peaks to $Li_xPF_yO_z$ [5,6]. This assignment is supported by the existence of intensity-ratio- and ΔBE-correlated peaks in the O 1s core-level spectra. An additional pair of features is observed in the F 1s and O 1s spectra following the first delithiation to 1.5 V that is tentatively attributed to $(SiF_6)^{2-}$ [7]. Lastly, SiO_xF_y is tentatively identified as a relatively strong set of peaks following the second lithitation to 0.05 V [8, 9].

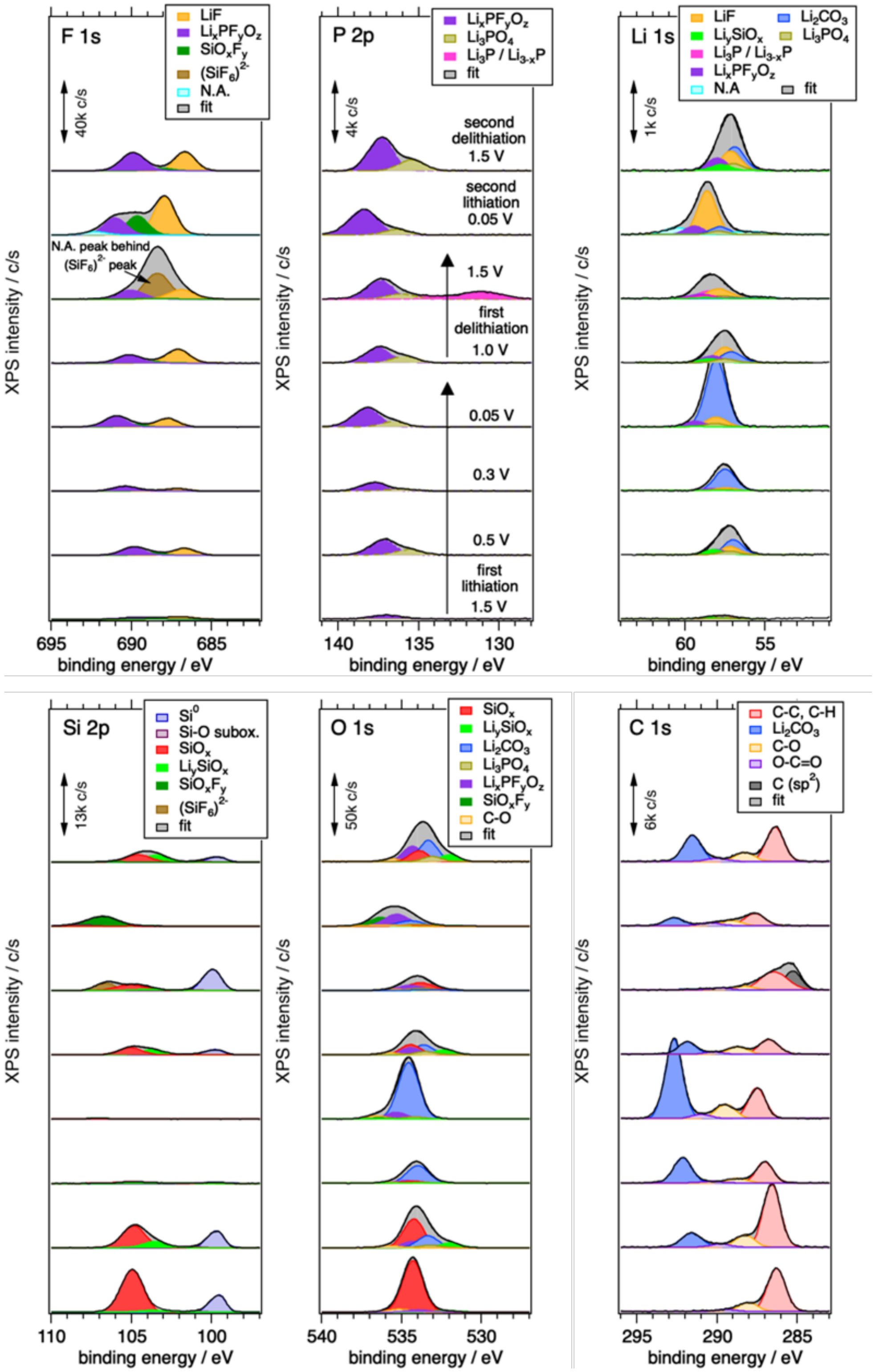

F 1s
LiF
$Li_xPF_yO_z$
SiO_xF_y
$(SiF_6)^{2-}$
N.A.
fit
40k c/s
N.A. peak behind $(SiF_6)^{2-}$ peak
P 2p
$Li_xPF_yO_z$
Li_3PO_4
Li_3P / $Li_{3-x}P$
fit
4k c/s
second delithiation 1.5 V
second lithiation 0.05 V
1.5 V
first delithiation 1.0 V
0.05 V
0.3 V
0.5 V
first lithiation 1.5 V
Li 1s
LiF
Li_ySiO_x
Li_3P / $Li_{3-x}P$
$Li_xPF_yO_z$
N.A
Li_2CO_3
Li_3PO_4
fit
1k c/s
XPS intensity / c/s
695
690
685
140
135
130
60
55
binding energy / eV
Si 2p
Si^0
Si-O subox.
SiO_x
Li_ySiO_x
SiO_xF_y
$(SiF_6)^{2-}$
fit
13k c/s
O 1s
SiO_x
Li_ySiO_x
Li_2CO_3
Li_3PO_4
$Li_xPF_yO_z$
SiO_xF_y
C-O
fit
50k c/s
C 1s
C-C, C-H
Li_2CO_3
C-O
O-C=O
C (sp^2)
fit
6k c/s
110
105
100
540
535
530
295
290
285

Figure 4. Summary of XPS measurements on 50-nm a-Si / 3-nm SiO_2 films at varying states of lithiation and delithiation. Peak assignments are preliminary, N.A. denotes “not assigned.”

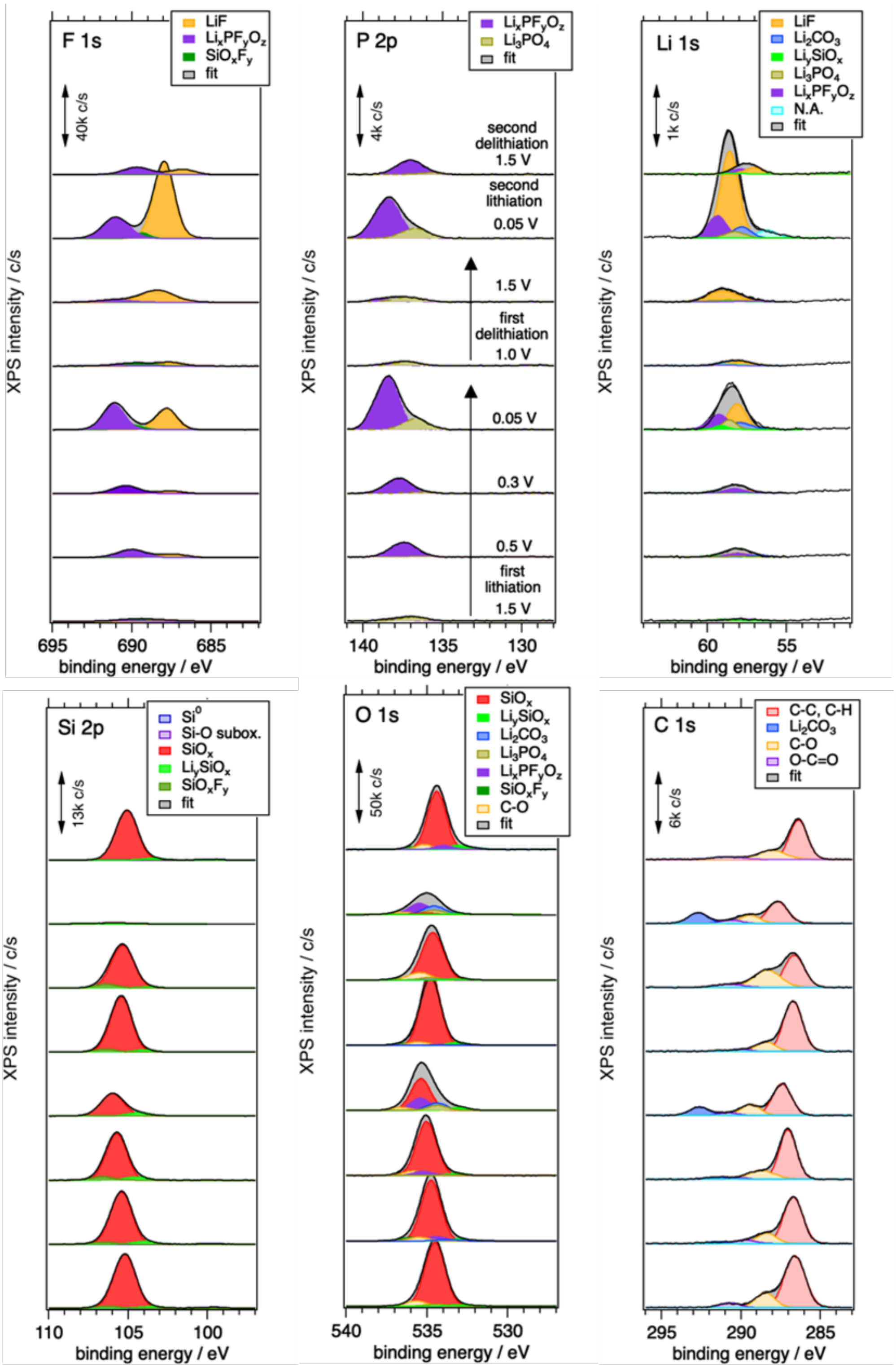

Figure 5. Summary of XPS measurements on 50-nm a-Si / 10-nm SiO_2 films at varying states of lithiation and delithiation. Peak assignments are preliminary, N.A. denotes “not assigned.”

XPS measurements for the 10-nm SiO_x samples are shown in Figure 5. For the most part, the same phases are observed for the SEI in these samples as were seen in the native-oxide samples. On the other hand, significantly less Li_2CO_3 is seen for the 10-nm samples than for the native-oxide sample, and it forms at substantially lower potentials. Also, less Li_ySiO_x phases are observed for the 10-nm sample. In contrast to the native-oxide samples, relatively more LiF and $Li_xPF_yO_z$-containing phases form on the 10-nm samples, especially at the lowest lithiation potential, 0.05 V.

An interesting feature for both the native-oxide and 10-nm SiO_x samples is that the peaks associated with Li_2CO_3 are most intense at the lowest lithiation potentials (0.05 V) and subsequently decrease during delithiation. Similar effects are seen with both LiF and the $Li_xPF_yO_z$ phase. Furthermore, the attenuation of Si^0 and SiO_x XPS signals also indicates that SEI layer thickness tends to increase during lithiation and decreases during delithiation. These observations suggest that formation of these phases is partially reversible, or, that after formation these phases can detach from the SEI.

C 1s spectral features tentatively assigned to C-C, C-H, C-O, and O-C=O moieties are observed on all samples, and, in general, the magnitudes of these peaks are not strongly correlated with lithiation/delithiation potential. With the exception of Si^0 peaks, there is considerable variability in measured binding-energy (BE) values for all phases, indicating varying degrees of charging during the XPS measurements. For both the native-oxide and 10-nm SiO_x samples, the observed trend is that peaks shift to higher BEs at lower lithiation potentials, consistent with lower net ionic and electronic conductivities in these SEI layers.

In summary, the key results of the XPS analysis include:

- For the native-oxide samples, a fraction of the initial SiO_x layer is converted to Li_ySiO_x phases during the first two cycles, but very little Li_ySiO_x is seen in the 10-nm SiO_x samples.
- Phases including LiF, Li_2CO_3, Li_3PO_4, and $Li_xPF_yO_z$ are clearly observed.
- The relative phase composition of the SEI layers evolve significantly over the course of cycling.
- SEI phase evolution in the 10-nm samples primarily takes place at markedly lower potentials than observed in the native-oxide case.

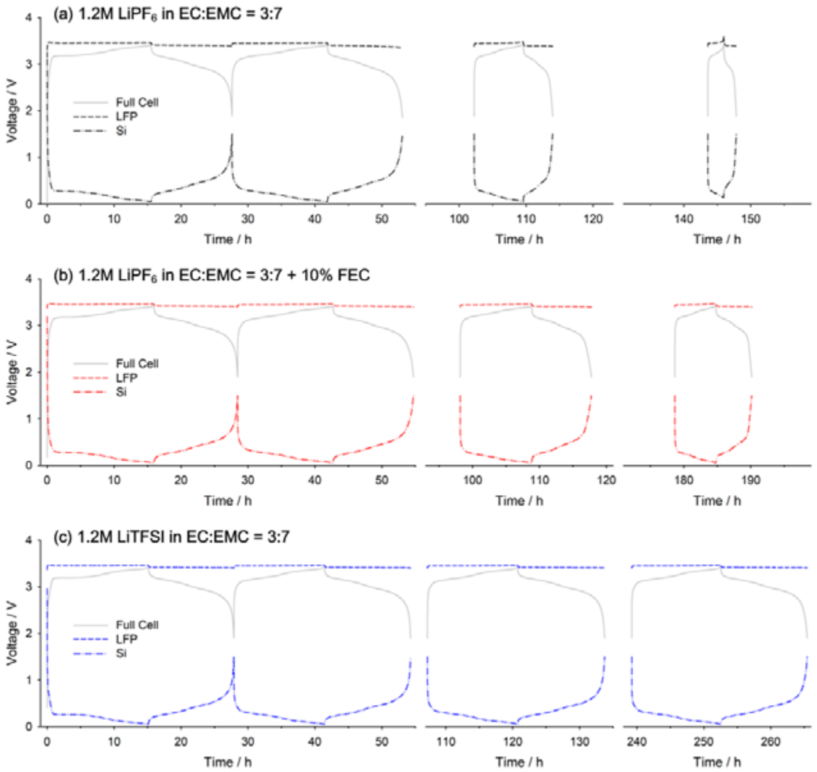

Figure 6. The voltage profiles of $LiFePO_4$/Si cells containing the 500-nm Si thin-film model electrodes (1st, 2nd, 5th, and 10th cycle) with (a) 1.2 M $LiPF_6$ EC:EMC (3:7 wt%), (b) 1.2 M $LiPF_6$ EC:EMC (3:7 wt%) + 10% FEC, and (c) 1.2 M LiTFSI EC:EMC (3:7 wt%).

Finally, we investigated the corrosion behavior of silicon electrodes in the full-cell configuration, in addition to the half-cell configuration, by employing $LiFePO_4$ (LFP) as cathode electrode. The use of LFP, which acts as source of limited amount of lithium, enables a direct visualization of the effect of the silicon corrosion and lithium consumption upon cycling. Fig. 6 and 7 show the voltage profiles (Fig. 6) and cycling performance (Fig. 7) of LFP/Si cells using three different electrolyte solutions, *i.e.* 1.2 M $LiPF_6$ EC:EMC (3:7 wt%), 1.2 M $LiPF_6$ EC:EMC (3:7 wt%) + 10%wt. FEC, and 1.2 M LiTFSI EC:EMC (3:7 wt%). As mentioned above, this full-cell system has a very limited amount of lithium, such that lithium loss upon cycling is directly visible from the remaining capacity of LFP/Si cells. In the initial 10 cycles, the cell with 1.2 M $LiPF_6$ EC:EMC (3:7 wt%) solution lost almost 80% of its initial capacity, which indicates that the lithium consumption from the corrosion behavior on the silicon surface had been very severe. The presence of FEC and the substitution of $LiPF_6$ with LiTFSI improved the cycling performance significantly, comparable to the previous results with the half cells. It should be noted that the cell with 1.2 M LiTFSI EC:EMC (3:7 wt%) presents remarkably good cycling performance and only loses a marginal amount of lithium upon cycling. These results suggest that the corrosion behavior on silicon affects the performance of full cells such that it needs to be reduced for the commercialization of silicon.

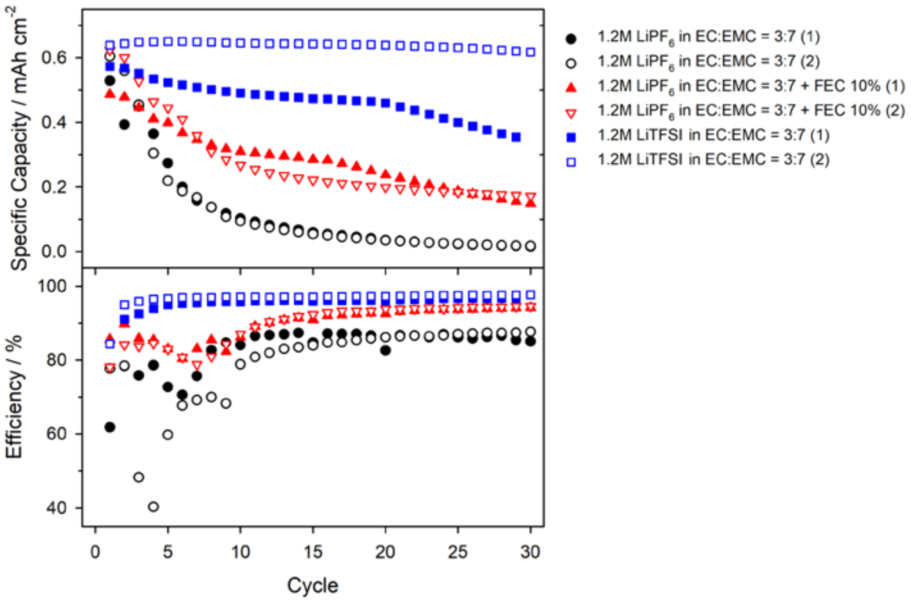

Figure 7. Cycling performance and efficiency of LiFePO$_4$/Si cells containing the 500-nm Si thin-film model electrodes with different electrolyte solutions.

To calculate the amount of consumed lithium from two possible sources—electrolyte decomposition and lithium trapping—we adopted a calculation model [10]. In this calculation model, the irreversible capacity originating from electrolyte decomposition is the difference between the consumed lithium during each lithiation step and the actual amount of inserted lithium to silicon in this step. The irreversible capacity originating from lithium trapping can be obtained by subtracting the delithiation capacity from the lithiation capacity in that cycle. The amount of inserted lithium (lithiation capacity) can be accessed by the quasi-open-circuit voltage (QOCV) at the end of each lithiation step. Figure 8 presents the schematic of the approach to the state-of-charge (SOC) value of each cycle through the QOCV and the galvanostatic intermittent titration technique (GITT) profile.

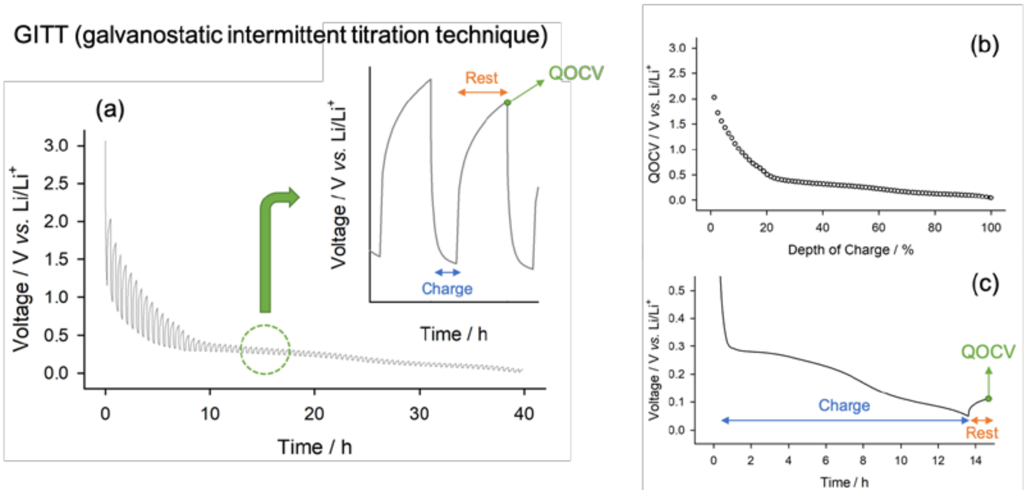

Figure 8. Schematic of the procedure to estimate the actual state of charge (SOC) of silicon electrodes. From (a) the GITT profile, (b) the relation between quasi-open-circuit voltage (QOCV) and SOC is obtained. At the end of each lithiation step, the SOC is extrapolated from (c), the observed QOCV in relation to the QOCV value on the GITT profile.

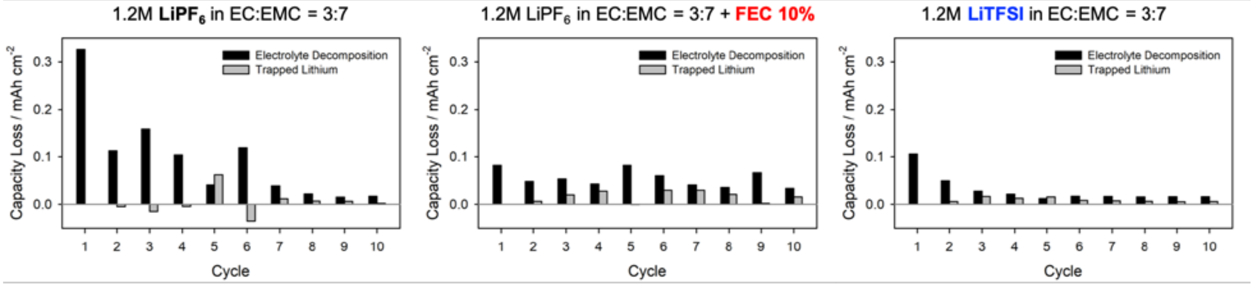

Sum of electrolyte decomposition	**0.95** mAh/cm^2
Sum of trapped lithium	0.03 mAh/cm^2

Sum of electrolyte decomposition	0.54 mAh/cm^2
Sum of trapped lithium	**0.15** mAh/cm^2

Sum of electrolyte decomposition	0.30 mAh/cm^2
Sum of trapped lithium	0.08 mAh/cm^2

Figure 9. The calculated capacity loss from electrolyte decomposition and lithium trapping in $LiFePO_4$/Si cells containing the 500-nm Si thin-film model electrodes with different electrolyte solutions.

Figure 9 shows the calculated irreversible capacity (capacity loss) originating from electrolyte decomposition and lithium trapping in $LiFePO_4$/Si full cells. Overall, electrolyte decomposition is dominant over lithium trapping regardless of electrolytes. It is noteworthy that the cell with 1.2 M $LiPF_6$ EC:EMC (3:7 wt%) solution loses the most lithium over the early 10 cycles, but also, that it shows surface instability (trapped lithium <0).

Again, this suggests the non-passivating behavior of silicon anodes in the standard condition. The calculated irreversible capacity from electrolyte decomposition correlates well with the cycling performance of full cells, indicating that electrolyte decomposition is the main reason of cycling decay of $LiFePO_4$/Si cells.

In summary, the Corrosion Task has led to the definition of standard protocols enabling a relative quantification of the non-passivating behavior of silicon model electrodes. A set of electrodes has been investigated to define the model electrodes of choice. Silicon thin films have been identified as the best model electrodes so far investigated. By applying Protocols 1 and 2 to various systems characterized by different properties (thickness of silicon, thickness of the oxide surface layer) and also different interfaces (employment of four types of electrolyte solutions), we have obtained preliminary conclusions. Specifically, the non-passivating behavior of silicon thin films has been directly observed for the first time as an independent effect from the cracking of silicon particles due to the lithiation. A visualization of the improvement of the passivation properties upon cycling has been quantified, suggesting a thickening of the passivating film on the silicon surface. The beneficial effect of FEC for the SEI stability has been confirmed, and the use of LiTFSI as alternative salt to improve the SEI stability is proposed. Furthermore, we investigated the effect of corrosion of silicon in the full-cell configuration using LFP/Si cells. Due to the non-passivating nature of silicon thin films, the lithium consumption upon cycling was substantial for the standard electrolyte solution. The full-cell results are comparable to our previous observation with the half-cells such that the use of FEC and LiTFSI mitigates such silicon corrosion. Further, the calculation model concludes again that the electrolyte decomposition and surface instability on the silicon anode is the main reason for the irreversible capacity and capacity loss of LFP/Si cells.

Electrolyte Additives and Detection

The solid-electrolyte interphase formed during the cycling of lithium-ion batteries by the decomposition of lithium salt and solvent molecules plays a crucial role in device performance. However, the detailed decomposition process and distribution of products remains elusive due to the wide variety of electrochemical pathways and the lack of facile analytical methods for chemical characterization of SEIs. In this report, a gradient polarity solvent wash (gradient wash) technique involving the use of solvents with gradually increased polarities is employed to sequentially remove different SEI components from electrode surfaces and the near-surface. Fourier transform infrared (FTIR) spectroscopy is used to characterize the SEIs composition. The impacts of electrolyte additives and discharge rates over SEI formation are illustrated. This study presents a new concept of a rationally controlled solvent wash technique for electrode surface analysis that can selectively remove targeted components with gradient wash of the targeted electrode (Figure 10). The gradient wash of electrodes was performed in glass vials, where the electrodes were immersed under 5-mL solvents with gentle manual agitation. The solvents used were 0% to 100% volume ratio ethyl acetate (EA) in hexane (Hex) solutions with 10% intervals (i.e., 0%, 10%, 20%, 30% EA/Hex, etc.). After rinsing, the electrodes were immediately dried and stored under vacuum until FTIR characterization.

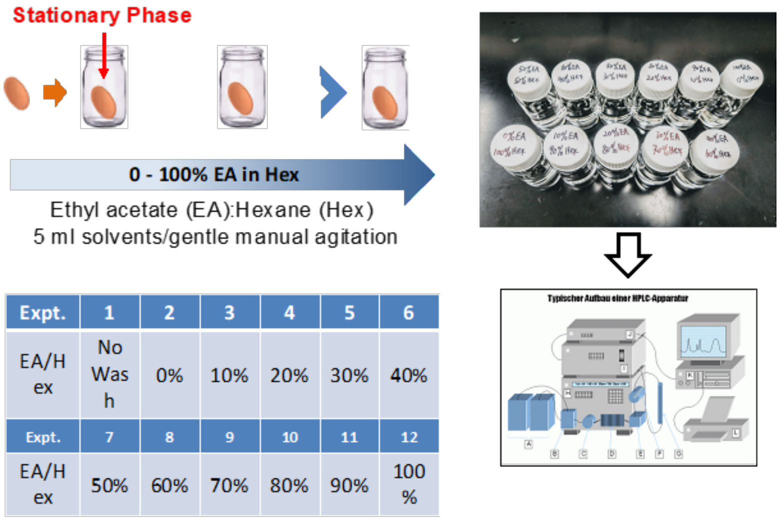

Expt.	1	2	3	4	5	6
EA/Hex	No Wash	0%	10%	20%	30%	40%
Expt.	7	8	9	10	11	12
EA/Hex	50%	60%	70%	80%	90%	100%

Figure 10. Schematics of the gradient polarity solvent wash technique.

We examine the SEIs and near-SEIs produced with both polar methacrylate additive under different electrochemical conditions by gradient wash. Cu electrodes are electrochemically cycled with $LiPF_6$ ethylene carbonate/ethyl methyl carbonate (EC/EMC) electrolyte containing the additive. With a binary solvent system of a non-polar solvent and a polar solvent at various ratios, it is possible to selectively remove different SEI components. The electrode surfaces before and after each wash protocol are characterized with FTIR to identify the decomposition products.

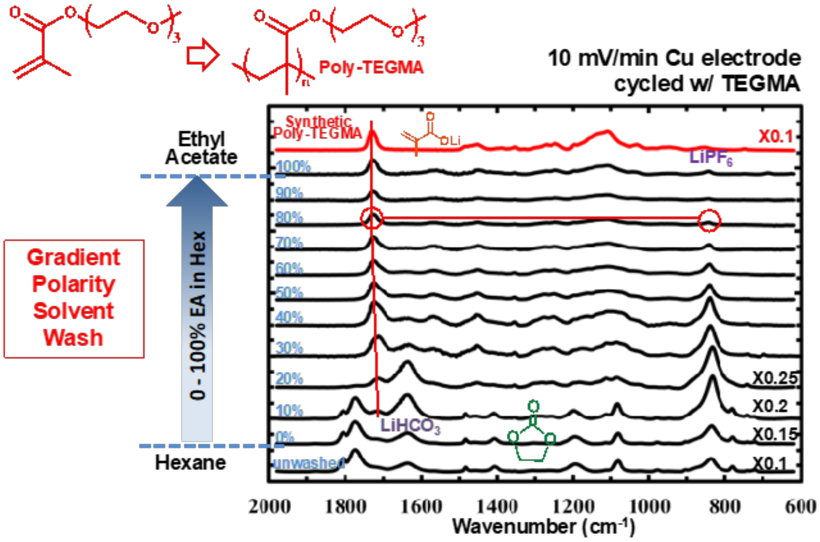

Figure 11. Gradient polarity solvent wash was applied to a Cu electrode polarized to 10 mV Li/Li$^+$.

TEGMA additive also produced a poly-TEGMA film on the Cu electrode surface, which, due to its high polarity, did not resist adsorption of residue electrolyte (EC/EMC:$LiPF_6$ solvates, 1809, 1780, 1269, 1196, 1082, 833 cm^{-1}) and Li_2CO_3 (1510, 1419 cm^{-1}) as shown in Figure 11, Spectrum I. The poly-TEGMA layer was fully exposed after gradient wash with 0%–30% EA/Hex solvents. This polar polymer film also survived all remaining washing steps. Its chemical composition was confirmed with the synthetic sample. The removal of electrolyte species with 0%–30% EA/Hex solutions is consistent with the case of the base electrolyte. It is worth noting that the carbonyl peak for poly-TEGMA at 1726 cm^{-1} presented a slight red shift before removal of lithium salt species due to solvation effect.

Decomposition Product Identified

Cu Electrode	0.0167 mV s^{-1} (1 mV min^{-1})	0.167 mV s^{-1} (10 mV min^{-1})	1 mV s^{-1} (60 mV min^{-1})
Base Electrolyte	LiEDC/LiEMC*, Li_2CO_3*	LiEDC/LiEMC*	/
LMA Electrolyte	Poly-LMA	Lithium Methacrylate oligo-LMA*	/
TEGMA Electrolyte	Li_2CO_3* Poly-TEGMA	Lithium Methacrylate Poly-TEGMA	Poly-TEGMA

*Rinsed off by gradient wash | Revealed by gradient wash

Figure 12. Three different scanning rates of CV at 1, 10, and 60 mV min^{-1} were applied to the Cu electrodes, respectively, with baseline electrolyte and two additives-based electrolytes. The Cu surface species vary due to both the additives and scan rates.

The scanning rate or the potential step-down rate from 3 V to 10 mV has a significant impact to the surface film (SEI) and near-surface species formation (Figure 12). At slow to medium rate of 1 to 10 mV min^{-1}, the baseline electrolyte (EC/EMC:$LiPF_6$) facilitates the formation of LiEDC/LiEMC salts on the Cu surface. In the two additives-based electrolyte-containing systems, they are predominantly additives-derived polymer films on the Cu surface instead of lithium salt species. The species on the Cu surfaces can be clearly observed with the gradient wash technique. However, when the voltage step rate is 60 mV min^{-1}, the Cu surface is free of deposition of decomposition products with the baseline electrolyte. A highly polar TEGMA additive tends to stick to the surface of the Cu at this fast scan rate. Therefore, the chemistry of SEI formation depends on the reaction rate, where lower lithiation rate favors the formation of lithium salts on the electrode surface, and faster rate promote the formation of polar organic decomposition products.

Glyme-Based Electrolytes for Amorphous Silicon Anodes: An Alternative to GEN2 to Improve Passivation

The standard Gen-II electrolyte, $LiPF_6$ in an EC/EMC mixture, has been extensively explored for model amorphous Si (a-Si) films and composite electrodes prepared by slurry casting. The choice of this electrolyte system originates from the successful commercialization of graphite anodes. However, carbonate-based electrolytes do not form stable interfacial layers on silicon. Recent studies by LBNL using model a-Si thin films show that carbonate-based electrolytes do not passivate the silicon surface during cycling, which results in an unstable SEI layer. Based on a suite of local SEI characterization conducted on model silicon anode (with a native nanometer suboxide layer) under the SEISta program, the dominant organic SEI components on a-Si include diethyl alkyl carbonates, carboxylates, and ethers. We hypothesize that solvents containing these functionalities may lead to more stable silicon interfaces. Therefore, the goal of this current work is to investigate ether-based solvents and compatible salts for Si anodes. Specifically, a-Si electrode were cycled in the following electrolyte systems: i) Gen-II electrolyte as a benchmark, ii) lithium bis(fluorosulfonyl)imide (LiFSI) dissolved in dimethyoxyethane (DME), and iii) LiFSI-DME with a fluoroether additive (1,1,2,2-

tetrafluoroethyl-2,2,3,3-tetrafluoropropyl ether, TTE, and iv) 1.2 M $LiPF_6$ in 1,2-dimethoxyethane (DME). TTE has been shown to stabilize the lithium-sulfur (Li-S) batteries [11] and Li-metal batteries [12].

For this work, 50-nm a-Si thin films were used as a model system. First, we explored the cyclic voltammetry (CV) of the a-Si anode cycled against a lithium counter electrode using different electrolytes at a scan rate of 0.1 mV s^{-1}. The initial onset reduction potential occurred at 0.4 V vs. Li/Li^+ for the Gen2 electrolyte, which was lower than that of the other electrolytes. Upon addition of 10 wt% FEC to Gen2, the reduction potential increased slightly to 0.42 V vs. Li/Li^+. The comparable increment occurred to $LiPF_6$-DME and LiTFSI-DME electrolytes. In comparison, the initial reduction peak was at 0.5 V vs. Li/Li+ for LiFSI-DME and did not change with the addition of TTE. The higher reduction potential for the LiFSI-DME system suggests that this electrolyte more readily reduced on the Si surface [13]. This peak became less prominent in subsequent CV scans (see Figure 13(b)), which indicates the presence of a passivated Si surface that inhibited further electrolyte reduction.

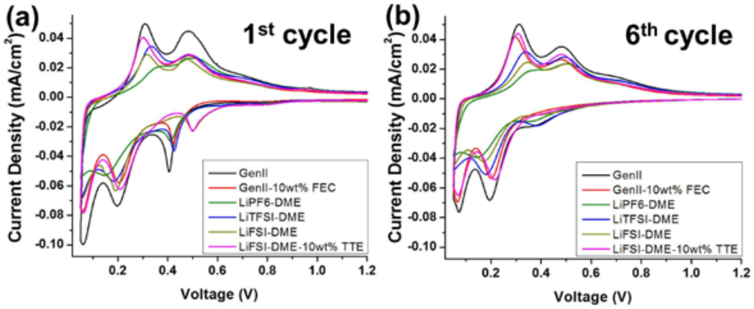

Figure 13. Cyclic voltammograms of a-Si thin-film anodes cycled in various electrolytes between 1.5 V and 50 mV vs. Li/Li^+ at a scan rate of 0.1 mV/s showing the (a) first and (b) sixth cycles.

We further used galvanostatic cycling (GC) and chronoamperometry (CA) testing to evaluate the SEI passivation on the a-Si anode using different electrolytes. This protocol was described in the Q2 report. The steady-state current measured after a 24 h potential hold at 50 mV vs. Li/Li^+ is attributed to continuous parasitic reactions occurring between the electrolyte and lithiated a-Si. As shown in Figure 14, the steady-state current density decreased after cycling for many electrolytes. In general, a lower parasitic current indicates a more effective SEI film on the a-Si surface. Surprisingly, a-Si cycled in Gen2-10 wt% FEC showed a 2-fold increase in the parasitic current during the first cycle compared to other electrolytes, as shown in Figure 14. The parasitic current of Gen2-10 wt% FEC exhibited a sharp drop during the first three cycles and became the smallest among all other electrolytes after five cycles. This result indicates that the SEI formed on a-Si anode during the first three cycles with Gen2-10 wt% FEC electrolyte was not stable. We note here that the SEI layer formed during the initial few cycles may deform and/or dissolve into the electrolyte upon extended cycling.

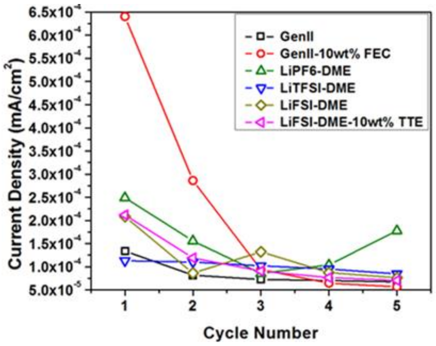

Figure 14. Summary of the parasitic current density during the galvanostatic cycling (GC) – chronoamperometry (CA) test for a-Si cycled in various electrolytes. During the formation cycle, the a-Si was first discharged to 50 mV vs. Li/Li$^+$ and then galvanostatically cycled between 1.5 V and 50 mV at 1C (41.7 μA/cm^2). In between each charge-discharge cycle, a 24-hour potential hold at 50 mV vs. Li/Li$^+$ was performed, and the steady-state current at the end of this step was recorded.

The fact that the parasitic current of glyme and carbonate electrolytes became comparable after five cycles motivates us to continue researching the passivation behavior of the glyme systems after extended cycling. Among all electrolytes, a-Si cycled in Gen2 exhibited the highest initial discharge/lithiation capacity, as shown in Figure 15. Addition of 10 wt% FEC to Gen2 stabilized the SEI formed on a-Si, as demonstrated by the improved capacity retention over 110 cycles (85% as compared to 31% for Gen2). a-Si cycled in $LiPF_6$-DME exhibited the lowest capacity among all electrolytes, agreeing with its unstable parasitic current as observed in the GC-CA test in Q3. The LiTFSI-DME and LiFSI-DME glyme electrolytes exhibited lower discharge capacity compared with Gen2+FEC. Although the addition of 10 wt% TTE to LiTFSI-DME and LiFSI-DME did not stabilize the a-Si well (Figure 15), a formulation containing LiFSI-DME-TTE in a 1:3:3 molar ratio significantly improved the cyclability of the a-Si anodes with 92% capacity retention after 110 cycles. This improved performance is attributed to the formation of a stable, robust SEI layer.

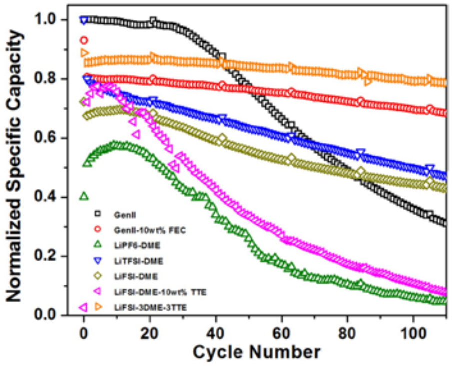

Figure 15. Variation of normalized discharge/lithiation capacity with cycle number (up to 110 cycles) of the a-Si anodes using multiple electrolytes at a 1C equivalent current density. All capacity values were normalized with respect to that of the Gen2 at Cycle 0.

We further explored the surface morphology of the a-Si anodes after prolonged cycles using scanning electron microscopy (SEM). The a-Si anodes cycled in Gen2 and Gen2+FEC electrolytes exhibited significant cracking, as shown in Figure 16. In comparison, the a-Si cycled in LiFSI-DME was covered by a patch-like SEI layer. This may suggest the mechanical failure of the formed SEI layer during Si expansion/contraction. The a-Si anode cycled in LiFSI-3DME-3TTE glyme electrolyte had a much smoother and crack-free surface after 110 cycles, indicating the presence of a more conformal passivation layer. This observation agrees well with the cycling results shown in Figure 15, which show excellent performance of a-Si cycled in LiFSI-3DME-3TTE.

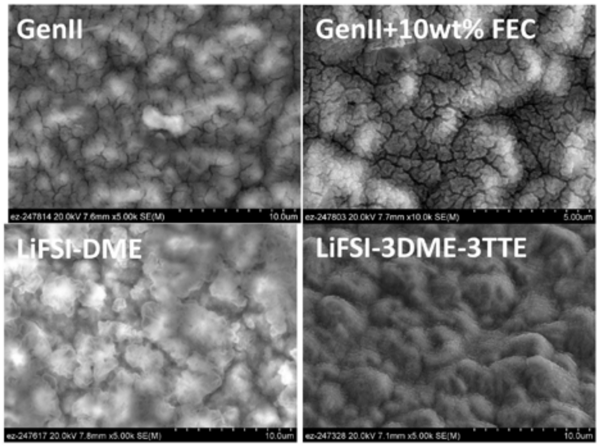

Figure 16. SEM micrographs of the a-Si anodes after 110 cycles.

The surface chemistry of the a-Si anodes during early cycles and after prolonged cycles was explored further by using energy-dispersive X-ray (EDX) spectroscopy. The surface elements in the SEI layer seen from EDX spectroscopy include carbon, oxygen, fluorine, silicon, and sulfur, as shown in Figure 17. Intriguingly, the C-O atomic ratio was close to 2:1 for Gen2 electrolyte after five cycles, suggesting that the initial SEI largely consisted of PEO-like oligomer species as previously reported [14]. After 110 cycles, the C-O ratio for Gen2 and Gen2+FEC was about 1:1, which suggests an increased abundance of C=O groups [14]. These carbonates may include Li_2CO_3 and/or lithium ethylene dicarbonate (LEDC) species. In contrast, the C-O ratio for LiFSI-3DME-3TTE glyme electrolyte was 2:1 after prolonged cycling, indicating enrichment of the organic PEO-like SEI species. This observation agrees fairly well with the infrared (IR) spectra of various a-Si samples cycled in glyme-based electrolytes as reported in a previous quarterly report. Notably, the addition of TTE did not increase the abundance of fluorinated species, which indicates that F content in the SEI layer is largely due to LiFSI decomposition.

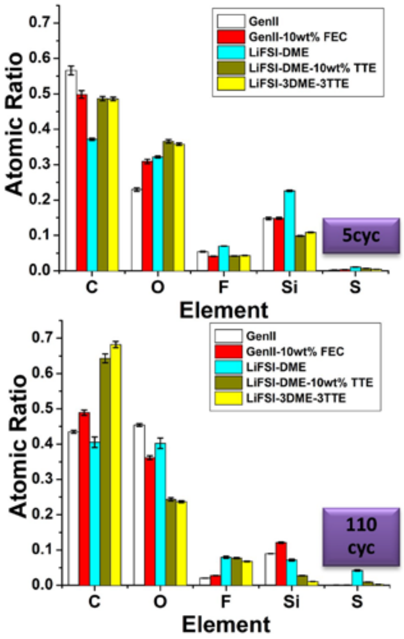

Figure 17. Elemental analysis of the a-Si anodes after five cycles and after 110 cycles using EDX. Error bar indicates the standard deviation of three measurements on three different locations of each sample.

Future research efforts will investigate the surface chemistry of the a-Si before/after cycling using X-ray photoelectron spectroscopy (XPS). We will also explore SEI formation mechanisms in different electrolyte systems. The effect of the electrolyte coordination chemistry will be evaluated for the LiFSI-3DME-3TTE using a similar method reported by Persson et al. [15]. 1H NMR has been measured on various electrolytes after cycling to study soluble electrolyte decomposition products. These data are being analyzed and will be reported in due course.

In summary, we evaluated the passivation behavior of glyme electrolytes on a-Si thin-film anodes. CV profiles indicate that LiFSI-DME-based electrolytes passivate the a-Si better during early-stage electrochemical cycles. The GC-CA test indicates that the SEI formed on a-Si in Gen2-FEC electrolyte is metastable for the first three cycles. In comparison, our new electrolyte formulation (LiFSI-3DME-3TTE) passivates the a-Si better for prolonged galvanostatic cycling. EDX elemental analysis on post-mortem a-Si anodes indicates that the Gen2 electrolyte passivation results in formation of an SEI enriched in carbonate species (e.g., lithium carboxylate, Li_2CO_3, and LEDC) after extended cycling. In contrast, using glyme-based electrolytes leads to the formation of PEO-like organic species on the a-Si surface.

Evolution of SEI on Si Wafer

Si wafers are the second model system that we used for studying the stability of the SEI and its evolution with cycling. Specifically we examined SEI formed on a Si wafer at 1, 10, 50, and 319 cycles, characterizing its thickness, resistivity, surface roughness, and chemical composition.

A native SiO_x-terminated Si wafer was cycled at a fixed current density of 6.82 μA cm^{-2} for a maximum time of 2 h per half cycle. Lithiation cutoff voltage was set at 0.01 V vs. Li/Li^+ while delithiation cutoff voltage was set at 1.5 V vs. Li/Li^+.

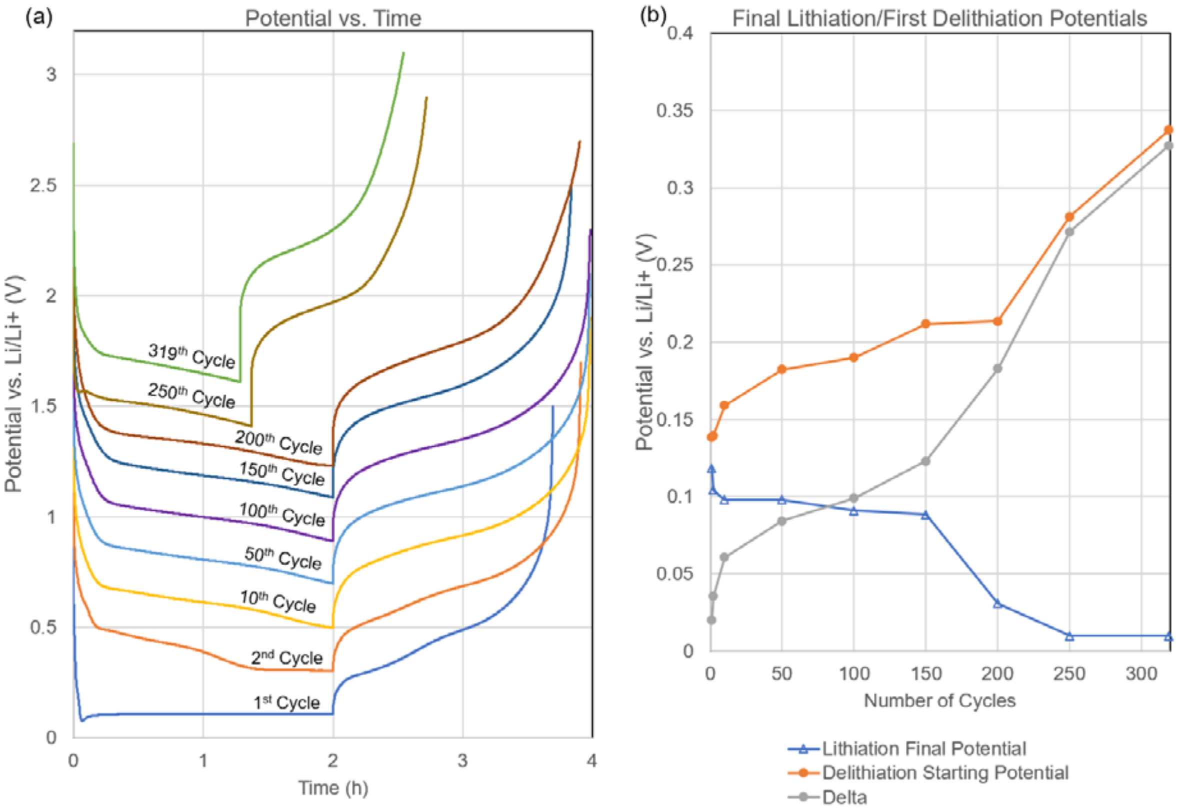

Figure 18. Electrochemical results of 319 cycles on native SiO_x-terminated Si wafer. Panel (a) shows potential vs. time for periodic cycles, with 0.2 V incremental offset, whereas (b) depicts the final lithiation potential and initial delithiation potential vs. number of cycles.

The first cycle depicts the characteristic features of lithiation of crystalline Si. In subsequent cycles, the potential reached at the end of the lithiation period drops lower, while the first potential during delithiation rises (Figure 18(b)). By the 200th cycle, during delithiation, the potential reaches the 1.5 V cutoff before the 2 h time limitation. By the 250th cycle, potential reaches the 0.01 V potential lithiation cutoff prior to the 2 h time limitation. These results indicate that the SEI becomes a barrier to Li diffusion, and/or the condition of the Si degrades such that it becomes increasingly difficult to electrochemically drive Li^+ into the Si and recover Li^+ during delithiation.

SEIs after 1, 10, 50, and 319 cycles were disassembled, soaked in DMC to remove residual salts, and transferred without atmospheric exposure to Ar glove boxes for further characterization. The results of scanning spreading resistance microscopy (SSRM) three-dimensional (3D) resistivity vs. depth profiling and atomic force microscopy (AFM) morphology measurements are summarized in Table 3.

Table 3. Summary of Results: SSRM 3D Resistivity vs. Depth Profiling of SEI and AFM Roughness

SEI Development Stage	Effect on SEI Thickness, *t*	Per Cycle SEI Growth Rate	Effect on SEI Resistivity, ρ_{SEI}	Effect on Si Resistivity, ρ_{Si}	Effect on Surface Roughness
Pristine Si → 1 cycle	Initial SEI formation, <10 nm	Large initial SEI growth rate	Well-segregated Initial SEI, resistive outer SEI, less resistive inner SEI	Decrease	Increase
1 cycle → 10 cycles	Increase	Decreased growth rate	Increase	Increase	Increase
10 cycles → 50 cycles	Increase	Decreased growth rate	Decrease	Increase	Increase
50 cycles → 319 cycles	Increase	Decreased growth rate	Decrease	Increase	Large Increase

Scanning transmission electron microscopy (STEM) was used to examine a focused ion beam (FIB)-prepared cross-sectional sample of the SEI formed at 50 cycles. Electron energy-loss spectroscopy (EELS) was also used to examine elemental SEI composition (Figure 19).

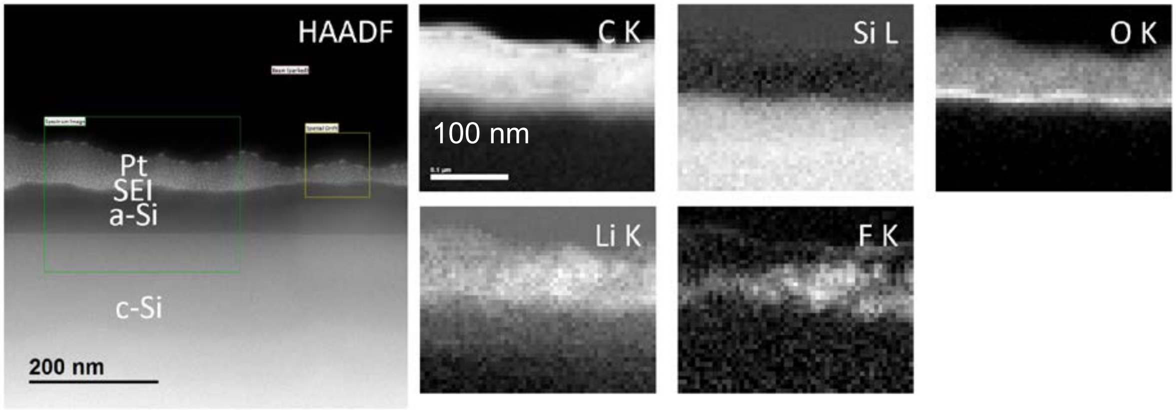

Figure 19. STEM HAADF image and EELS areal density maps for a FIB-prepared cross section of SEI formed on Si wafer after 50 cycles. C K, Si L, O K, Li K, and F K EELS areal density maps, with map area shown in the green box on the HAADF image, depict elemental composition of SEI.

STEM HAADF image shows that heterogeneity has already begun to form in the active Si material and SEI, while a linear amorphization front is achieved by lithiation. Expansion of lithiated Si forms an uneven amorphized Si layer of 80–120 nm in thickness. SEI shows a Li-, F-, O-, and C-rich composition (Figure 19).

Secondary-ion mass spectrometry (SIMS) was carried out on formed SEI after 1 and 319 cycles. The comparative SIMS depth profiles are shown in Figure 20.

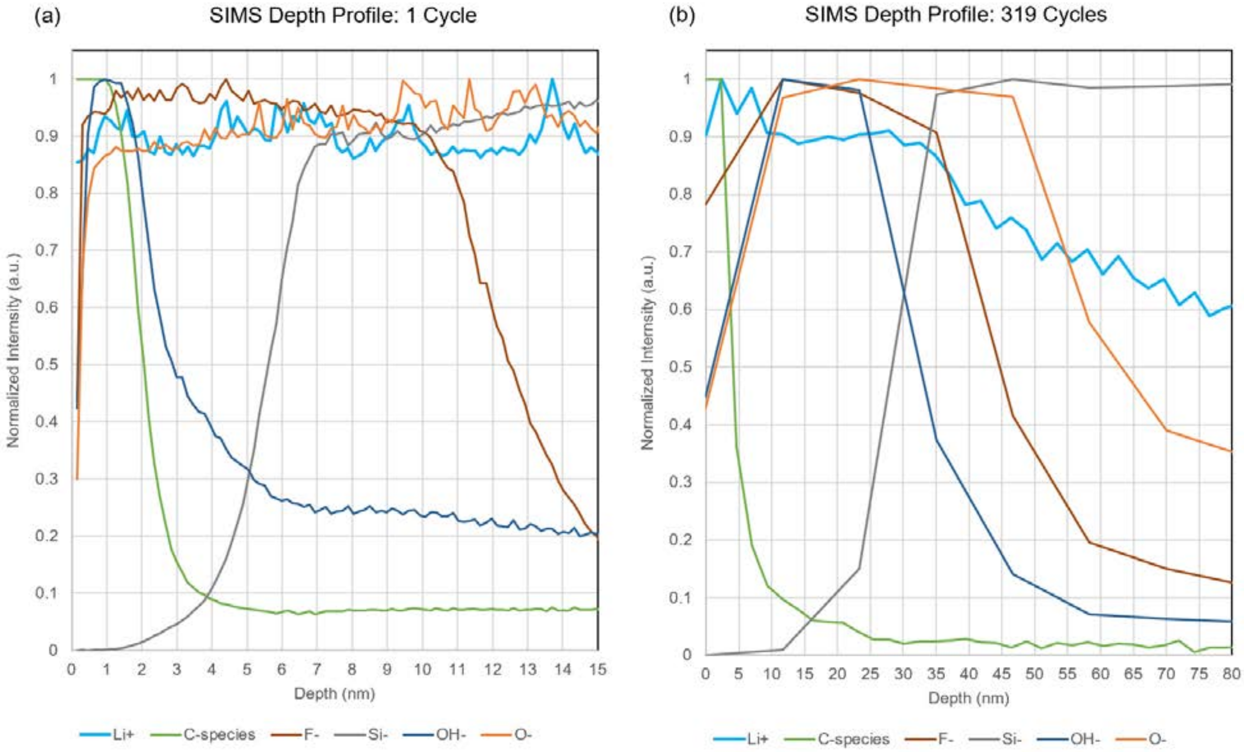

Figure 20. SIMS depth profiles on formed SEI after 1 cycle (left) and 319 cycles (right). All series are normalized to their maximum intensity.

SIMS depth profiles show that SEI composition remains somewhat consistent throughout its evolution; however, from 1 cycle to 319 cycles, there is an increase in the relative composition of hydroxides with a concurrent decrease in the relative composition of organic species. The SEI and the underlying Si show high levels of O, F, and Li. Thickness increases substantially from 1 to 319 cycles, consistent with SSRM thickness measurements.

In summary, electrochemical results show that the cyclability of Si wafer diminishes by about 250 cycles. At later stages of cycling, increasingly large potentials are required to drive lithiation and recover Li^+ from Si. SSRM results show that the thickness of SEI increases from 1→10→50→319 cycles, while surface roughness measured with AFM also increases, with a dramatic increase in roughness between 50 and 319 cycles. SIMS and STEM EELS show a layered composition of SEI, with C-rich species at the surface SEI and O, Li, and F located in the inner SEI.

Effect of Water Concentration in the Electrolyte on the Thickness and Composition of the Silicon/Electrolyte Interface

The concentration of water in an electrolyte significantly affects the stability of the silicon/electrolyte interface (SiEI) and the subsequent electrochemical performance of a cell because water is known to react with $LiPF_6$ salt in carbonate-based electrolytes to generate corrosive HF [16], which further reacts with Si and SiO_2. To understand how the presence of water in the system affects the interfacial chemistry and evolution of the Si anodes, we evaluated the electrochemical performance of a model Si wafer electrode in Gen2 electrolyte (1.2 M $LiPF_6$ in ethylene carbonate (EC): ethyl methyl carbonate (EMC), 3:7 wt%) with 50 ppm of water. The custom three-electrode O-ring cells were potentiostatically held at four different voltages, determined from the dQ/dV plot that shows redox behaviors of the electrolytes, to investigate the surface chemistry changes and evolution within SiEI at selected specific voltages. The mechanistic analysis of formed and evolved SiEI was performed using a variety of analytical techniques including AFM, SSRM, XPS, time-of-flight SIMS (ToF-SIMS), FTIR spectroscopy, and gas chromatography-mass spectrometry (GC-MS). From these measurements, we report the thickness and composition of the SiEI layers formed at different voltages and how it changes when water is added to the electrolyte.

Electrochemical Performance

Potentiostatic hold experiments were performed using a previously described (FY19 Q3) custom three-electrode O-ring cell. The working electrode was a Si wafer (675 µm thick, 0.001–0.005 Ω cm, p-type (B), 1.2-nm native oxide on the surface) and both reference and counter electrodes were Li metal foils. The working electrode was held at 1.0, 0.5, 0.2, or 0.01 V (*vs.* Li/Li$^+$, hereafter) for 10 hours after 2 hours rest at the OCV. The cells were immediately disassembled after the 10 hours of voltage hold to minimize the dissolution of the SiEI layer. The Si wafers were soaked in 1 mL of DMC for 60 seconds to remove residual electrolyte from the surface and further dried under dynamic vacuum for 30 min prior to being analyzed. All measurements were carried out under Ar atmosphere.

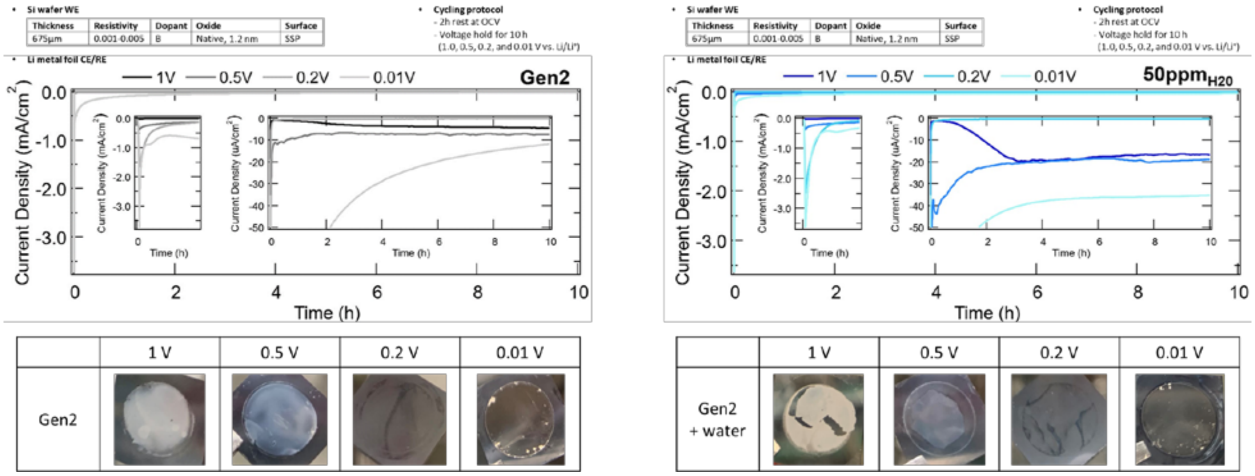

Figure 21. Changes in the current density over time during the potentiostatic hold at 1.0, 0.5, 0.2, and 0.01 V (vs. Li/Li+) in Gen2 (left) and Gen2 + H_2O $_{50\ ppm}$ (right). Corresponding images of the Si wafers after the potentiostatic hold are shown below each Current Density vs. Time plot.

In Figure 21, changes in the current density during the potentiostatic hold are presented along with the images of electrochemically treated Si wafers. First, looking at the initial current spike immediately after applying the voltage, a larger reductive current is observed when a lower voltage is applied in both Gen2 and Gen2 with 50 ppm of added H_2O ("Gen2+H_2O_{50ppm}"). The steady-state current also follows the same trend (i.e., a larger current at a lower voltage)—except for 0.2 V, where the current decays to near zero. Such behavior indicates that a surface layer is formed between 0.5 and 0.2 V that successfully inhibits further electrolyte reduction, and additional reactions may not occur because the crystalline wafers cannot be lithiated at 0.2 V. On the other hand, at 0.01 V, we observed a large current flowing mostly due to the lithiation of the silicon. Another interesting observation is that the steady-state current is greater in Gen2+H_2O_{50ppm} than that observed in Gen2 at the same voltage. This additional charge can be attributed to the side reactions taking place in the presence of water starting at about 1.0 V. The images of the Si wafers clearly show different surface layers formed at different voltages (Figure 21). To understand the nature and properties of these SiEI layers, we performed a series of surface chemistry and property analysis.

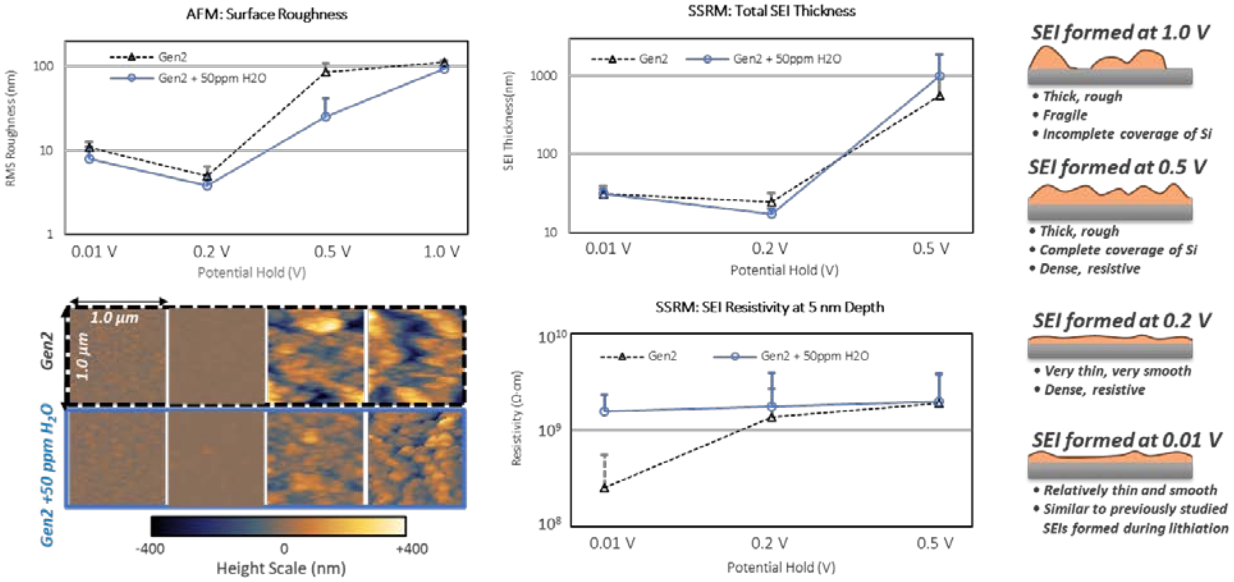

Figure 22. Roughness, thickness, and resistivity of the SiEI measured with AFM and SSRM. Mean results are plotted and the standard deviations are shown as error bars. Schematic diagram of the SiEI layer formed at different voltages is shown on the right.

Roughness, Thickness, and Resistivity of the SiEI

AFM and SSRM measurements were conducted to analyze the roughness, thickness, and resistivity of the SiEI layer. The measurements were carried out three times on freshly prepared 24 samples (6 samples—3 without water and 3 with water—for 4 voltage conditions) to validate the results and provide error bars (Figure 22). The root-mean-square (RMS) surface roughness values measured with AFM, and the corresponding images, show that the SiEI formed in the presence of water is smoother at all voltages tested. As a function of voltage, the SiEI layers that formed at 1.0 and 0.5 V are significantly rougher than those formed at 0.2 and 0.01 V (for both Gen2 and Gen2+ H_2O_{50ppm}). Further, the SSRM results show that the thickness of the SiEI also dramatically changes between 0.2 and 0.5 V, showing that the 0.5 V layer is significantly thicker, ~700–1,000 nm (*vs.* ~20–40 nm at 0.2 V). Such behavior can be correlated to the electrochemical performance (Figure 21) where the electrolyte reduction, and resulting SiEI buildup, was successfully hindered at 0.2 V. It is quite challenging to perform SSRM measurements in contact mode for the 1.0 V samples because the SiEI layer is too fragile. The SiEI formed at a higher voltage is more resistive in Gen2, whereas the resistivity does not change much among the SiEI formed at different voltages in the presence of water. At 0.01 V, we measured the SiEI resistivity to be significantly greater (almost an order of magnitude) in the presence of water. This can be explained by the fact that more charges are consumed by the side reactions in the presence of water and less lithiation of silicon occurs. The AFM and SSRM results are summarized in a schematic diagram shown in Figure 22.

Chemical Composition of the SiEI

To understand the chemical composition of the SiEI, we used spectroscopic techniques. First, XPS spectra were collected to look at Si 2p, O 1s, C 1s, F 1s, P 2p, and Li 1s core levels (Figure 23). Si 2p spectra in both Gen2 and Gen2+H_2O_{50ppm} show the same trend upon changing: the voltage where strong signals from Si^0 (~99 eV) and SiO_x (~104 eV) are observed at 1.0 V and the signals vanish at 0.5 V. The high intensity of Si 2p peaks at 1.0 V can be correlated to the AFM results, where the SiEI formed at 1.0 V exhibited high roughness and incomplete coverage of Si. At 0.5 V, the SiEI is thicker and there is complete coverage of Si, which induces no Si signal detection from the XPS spectra. At 0.2 V, the SiEI is thinner and more compact; thus, the Si core levels are observable, and at 0.01 V, lithiated Si species (Li_xSi at ~97 eV and Li_ySiO_x at ~102 eV) are detected. Another voltage-dependent trend is observed in the C 1s and O 1s spectra. In both Gen2 and Gen2+H_2O_{50ppm}, the SiEI formed at 0.5 V has a large amount of C-H species and fewer C-O species. These findings are corroborated using ATR-FTIR measurements (Figure 24): strong $-CH_3$ and $-CH_2$ stretching modes are observed in the 0.5 V sample spectra between 2850 and 2950 cm^{-1}. In addition, the peaks at 1655 cm^{-1} and 910 cm^{-1} suggest the presence of alkene species. The ATR-FTIR spectra also reveal vibrational modes from carboxylate, ester, and ether species in 1.0 V and 0.2 V samples and not in the 0.5 V samples, in agreement with the XPS results.

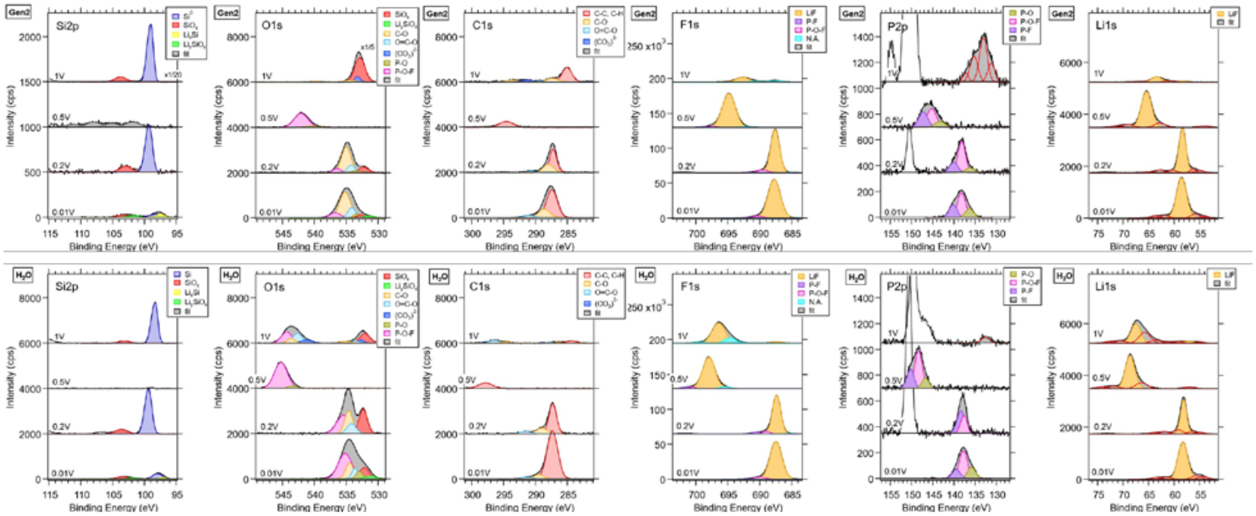

Figure 23. XPS spectra of the SiEI layers formed in Gen2 (top) and Gen2+H_2O_{50ppm} (bottom) at 1.0, 0.5, 0.2, and 0.01 V as indicated in the figure. Si 2p, O 1s, C 1s, F 1s, P 2p, and Li 1s core levels are presented.

Looking at other elements in Figure 23, a significant amount of LiF (~58 eV and ~688 eV in Li 1s and F 1s core levels, respectively) is detected in all samples. Further, higher concentration of fluorophosphates are detected in the SiEI formed in Gen2+H_2O_{50ppm}. Specifically, significant amount of charging is observed (~9 eV) in the white layer of SiEI (Figure 21) formed at 1.0 V as a byproduct of the reactions involving the water in the system. The layer consists of fluorophosphates, LiF, and C-O-containing species. In addition, GC-MS measurements of the electrolytes salvaged from the disassembled cells confirm the presence of fluorophosphates in the 1.0 V sample. Fluorophosphates are known reaction products in the hydrolysis of PF_6^- (Figure 24). This agrees well with XPS results, where the effect of water in the electrolyte is maximized at 1.0 V, because not many reactions occur in Gen2 at this voltage except extensive side reactions from water.

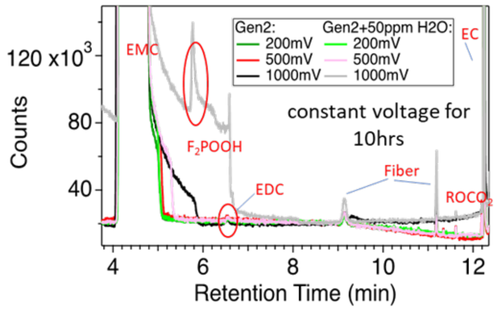

LiPF$_6$ hydrolysis

$LiPF_6 \rightleftharpoons LiF + PF_5$

$PF_5 + H_2O \rightarrow POF_3 + 2HF$

$POF_3 + H_2O \rightarrow HPO_2F_2 + HF$

Figure 24. ATR-FTIR spectra of the SiEI layers formed in Gen2 and Gen2+H_2O_{50ppm} at 1.0, 0.5, 0.2, and 0.01 V.

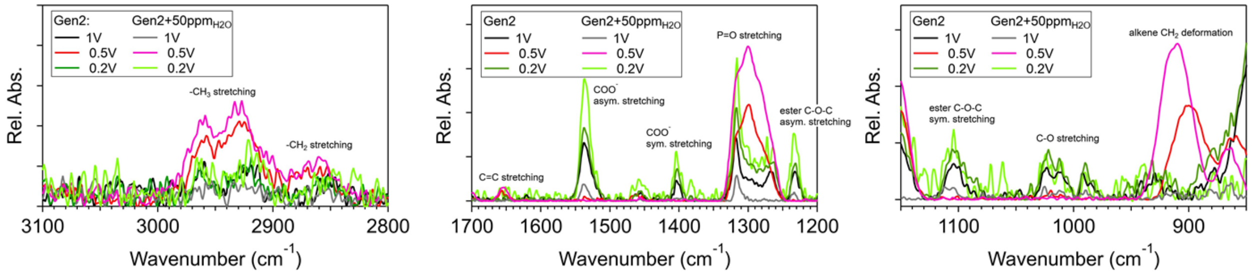

Figure 25. Gas chromatograms of electrolytes recovered from the cells after the potentiostatic holds (left) and the chemical equations of the $LiPF_6$ hydrolysis reaction (right).

Three-Dimensional Elemental Maps of the SiEI

To further analyze the elemental distribution of the SiEI, we obtained ToF-SIMS 3D tomography images on selected voltages, 0.2 V and 0.5 V, as shown in Figure 26. The SiEI layers formed at 0.2 V are relatively thin, in both Gen2 and Gen2+H_2O_{50ppm}, which agrees with the thickness measured with SSRM (Figure 22). In addition, a similar distribution of F^- and Li^- indicates the existence of LiF, which was also observed from the XPS results (Figure 23). One major difference is that the SiEI formed in Gen2+H_2O_{50ppm} shows a pitted structure in Si, possibly due to the reactions of Si and SiO_2 with HF formed from the $LiPF_6$ hydrolysis. In the case of 0.5 V, relatively thicker SiEI layers are formed—again, in agreement with the SSRM results—and the intensity of LiF is highest right on top of the Si substrate. It is obvious that more inhomogeneous layers are formed in the presence of water.

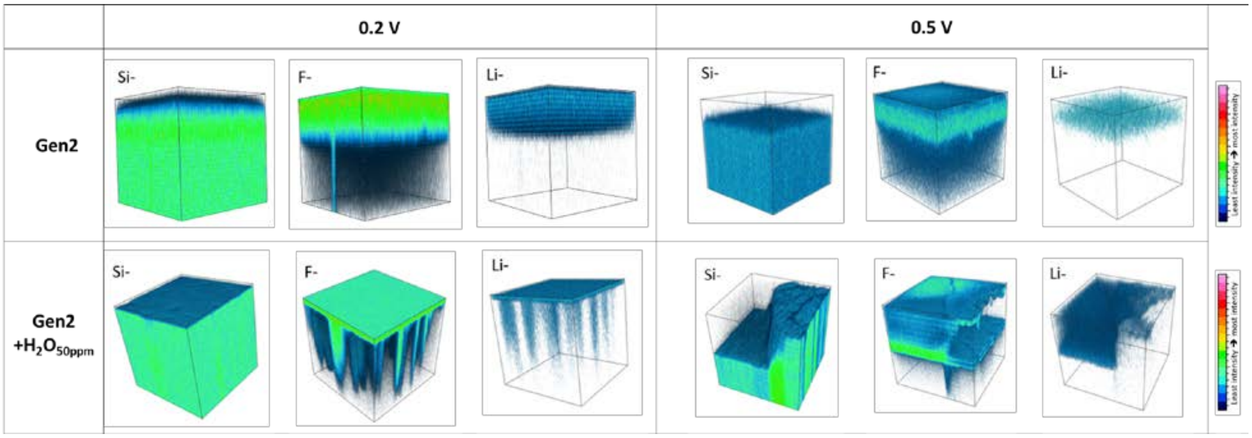

Figure 26. High-resolution elemental maps of SiEI layers formed at 0.2 V (left) and 0.5 V (right) in Gen2 (top) and Gen2+H_2O_{50ppm} (bottom). The intensity is on a blue-to-red color scale, with red being the highest intensity.

In summary, detailed analysis of the SiEI layers formed at different voltages (1.0, 0.5, 0.2, and 0.01 V *vs.* Li/LI^+) was performed using a variety of techniques including AFM, SSRM, XPS, ATR-FTIR, GC-MS, and ToF-SIMS. The effect of water concentration in the electrolyte (50 ppm) on the thickness and composition of the SiEI was also studied. The SiEI layers formed at both 1.0 V and 0.5 V show a thick and rough texture, but the SiEI formed at 1.0 V has a porous structure whereas the SiEI formed at 0.5 V exhibits a complete coverage of Si. Between 0.5 V and 0.2 V, the thickness and the roughness of the SiEI dramatically decreased, possibly due to the formation of a layer that successfully hindered further electrolyte decomposition and subsequent SiEI formation. The SiEI formed at 0.5 V had more C-H and less C-O species than the SiEI formed at all the other voltages. When 50 ppm of water is added to the electrolyte, the formed SiEI has more fluorophosphates generated during the $LiPF_6$ hydrolysis and the Si has pitted structures with an inhomogeneous SiEI. Such behavior can be attributed to the reaction of Si and SiO_2 with HF, a product of the $LiPF_6$ hydrolysis reaction.

Si Electrode Investigation: Superior Carbon Coating Alters Si Materials Transformation During Electrochemical Process

To address the large volume change and excessive surface reaction of silicon materials during lithiation and delithiation reaction, carbon coating has been widely used as an electric conductive medium and electrolyte insulating buffering layer to encapsulate the silicon particles. Despite the reported improved capacity retention of Si-based material by carbon coating, there is relatively less investigation of the Si material transformation with the carbon coating. Moreover, many different precursors can be used to produce the carbon coatings, which, however, result in the coating having very different chemical and morphological characteristics. Here, we report the drastically different Si solid-state transformation during electrochemical process due to the different types of carbon precursors and carbon coatings on the same Si nanoparticles.

A high-temperature thermal-based carbonization process is used to produce carbon coating on Si nanoparticles. Organic-based precursors are used to form carbon coatings. Different precursors tend to form carbon coatings with different morphologies. Two types of carbon coatings can be formed on Si: one is a highly graphitized and dense coating from a polymer precursor (Si/C-P), and the other is more disordered structures from a sucrose precursor. The Si materials with highly graphitized and dense coating are able to deliver higher gravimetric capacity and stable cycling compared to that of the Si with disordered carbon coating. The dramatic differences come from the Si materials transformation. The Si/C-P materials maintain a two-phase reaction during delithiation in the first 30 cycles, whereas the Si/C-S forms an amorphous structure after the 1st cycle, and it does not form a clear two-phase transformation during delithiation.

A Si/C electrode with compact and ordered carbon coating was prepared with polyvinylidene chloride (Si/C-P electrode), and a Si/C electrode with loose and porous carbon coating was made with sucrose (Si/C-S electrode) for comparison. The cells of the Si/C electrodes were cycled at C/10 between 1.00 V and 0.01 V after a formation step at C/20 (1C = 2,000 mAh g^{-1}). All the reported capacities are based on the total mass of Si/C composites. Figure 27(a) presents the cycling performance and Coulombic efficiency (CE) of Si/C-P and Si/C-S. The initial Coulombic Efficiency (ICE) of Si/C-P (72.7%) is much higher than that of Si/C-S (56.1%). The compact carbon structure in the Si/C-P sample can protect the silicon nanoparticles from direct exposure to the electrolyte, and thus, leads to improved ICE. After the formation step, the CE of the Si/C-P electrode increases to above 99.0% after 10 cycles and to 99.5% after 20 cycles. On the other hand, the CE of the Si/C-S electrode stays below 99.0%. The Si/C-P electrode exhibits a specific charge capacity of 1219.6 mAh g^{-1} with the capacity retention of 98.1% after 20 cycles at C/10, which is higher than those of the Si/C-S electrode, 692.7 mAh g^{-1} and 77.0 %, respectively. At the 25th cycle, the CE of the Si/C-P electrode experiences a sharp decrease, dropping from 99.8% to 98.6%, which is rationalized as a consequence of the fracture of the carbon coating. After the fracture of the carbon coating, the CE of the Si/C-P electrode drops to about 98%, which is very similar to that of the Si/C-S electrode. During the 30th–50th cycle, the Si/C-P electrode presents a gradually decreasing capacity from 1149.5 to 1078.0 mAh g^{-1}, and the capacity retention ratio of the Si/C-P electrode during these 20 cycles is 93.8%. These results indicate that the more compact carbon coating of the Si/C-P material helps to decrease interface reaction and increase cell life. In addition, after the breakdown of the carbon coating on the Si/C-P sample, the interface stability of the Si/C-P sample begins to decay.

To better understand the electrochemical behavior of the Si/C-P electrode during the lithiation and delithiation process, the voltage profiles of the Si/C-P electrode from the 2nd–50th cycles are examined in Figure 27(b). There is a major plateau at 0.43 V for the 2nd–20th delithiation curves, which disappears beyond the 30th cycle where the carbon coating is fractured. The disappearance of the voltage plateau at 0.43 V indicates a significant bulk structure change during lithiation and delithiation processes due to the carbon-coating fracturing. This is the first observation of the influence of compact and ordered carbon coating on bulk Si particle structure transformation during electrometrical process. Figure 27(c) shows dQ/dV plots for the Si/C-P electrode for 2nd–50th cycles. During the 2nd lithiation cycle, three different processes are observed. The first discharge process at ~250 mV is associated with the gradual lithiation of the a-Si to form $Li_{\sim2.0}Si$, a structure that still presents extended Si networks and large Si-Si clusters. The second process at ~80 mV is related to the further lithiation of $Li_{\sim2.0}Si$ to $Li_{\sim3.5}Si$. At this stage, large Si-Si clusters broke into smaller Si clusters and isolated Si anions. The third process at ~35 mV corresponds to the formation of the crystalline phase, c-$Li_{3.75}Si$, from a-Li_xSi. The third process is not observed beyond the 30th cycle. As for the de-lithiation process, there is a strong and sharp peak at ~430 mV for the 2nd–20th cycles, which is associated with the two-phase transition from c-$Li_{3.75}Si$ to Li_xSi (x = 0–2.0). In this case, the x value is approaching 0 to reflect the dominating two-phase transition from $Li_{3.75}Si$ to almost delithiated amorphous Si, with minor transition from Li_xSi to a-Si phase. However, beyond the 30th cycle, where the carbon coating is fractured, two broad peaks at ~280 mV and ~500 mV are observed instead (no sharp peak at ~430 mV), which is an indicator of solid-solution reaction. This observation demonstrates that the formation of c-$Li_{3.75}Si$ is no longer the dominating process and that there is no direct transformation from c-$Li_{3.75}Si$ to amorphous Si particles. To be more specific, the two broad peaks are associated with the delithiation process of Li_xSi (x = 3.5–3.75) to $Li_{\sim3.5}Si$ (~280 mV) and $Li_{\sim3.5}Si$ to $Li_{\sim2.0}Si$ (~500 mV). The compact and unbroken carbon coating can enhance the kinetic property of the Si alloying reaction by improving the conductivity of Si and by promoting the formation of the small Si clusters and isolated Si anions with uniformly dispersed silicon particles. Due to the enhanced alloying kinetics, the Si/C-P electrode can continuously generate c-$Li_{3.75}Si$ during the lithiation process.

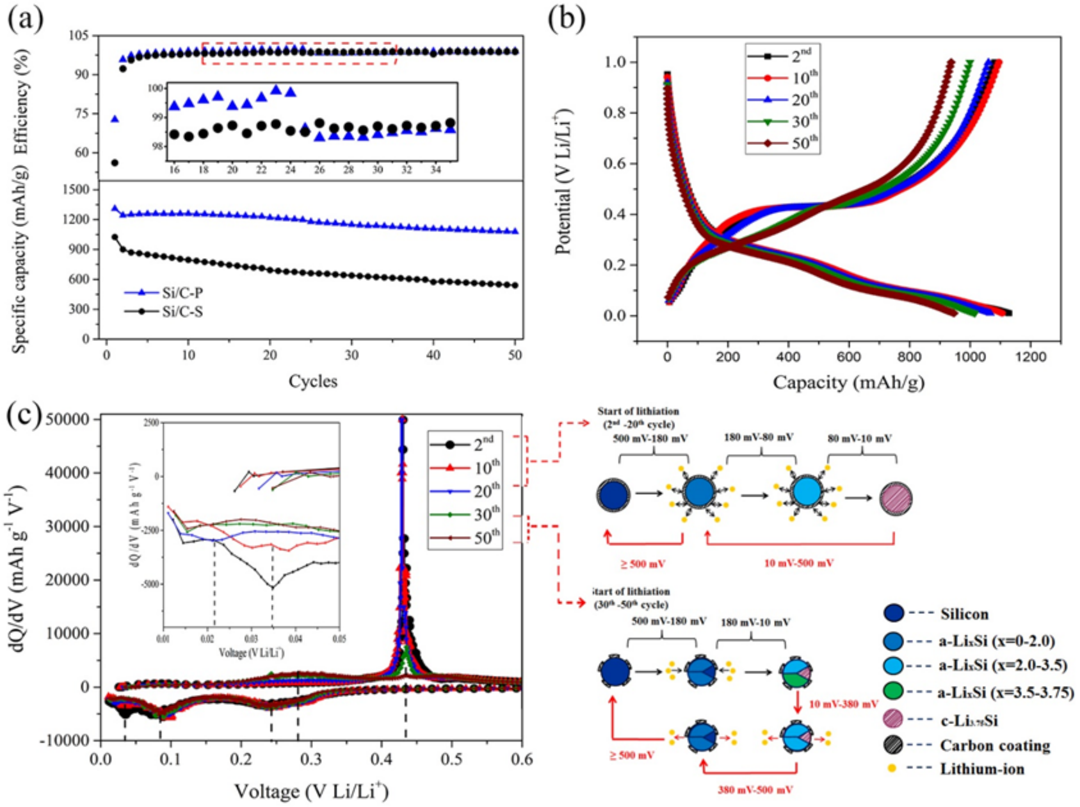

Figure 27. (a) Cycling performances and Columbic efficiencies of Si/C-P and Si/C-S electrodes at C/10, from 1.00 V to 0.01 V; (b) Galvanostatic discharge/charge profiles of Si/C-P electrode from 2nd to 50th cycles at C/10, from 1.00 V to 0.01 V; (c) Differential capacity vs. potential curves of Si/C-P electrode from 2nd to 50th cycles at C/10, from 1.00 V to 0.01 V (1C = 2,000 mAh g^{-1}).

Conclusions

The non-passivating behavior of silicon model electrodes has been analyzed by means of electrochemical protocols specifically designed for these studies. Three model electrodes were used: amorphous Si thin films deposited on Cu, Si wafers, and Si nanoparticles. A suite of techniques were employed to determine the nature of SEI components and its physical characteristics, such as FTIR, XPS, ToF-SIMS, GITT, SSRM, and the newly developed gradient polarity solvent wash (gradient wash) technique.

Clearly, it has being shown that the non-passivating behavior of silicon thin films can be observed independently from the cracking of silicon electrodes caused by the lithiation. The main decomposition products forming the SEI have been studied, as well as the effect on the morphology and physical properties of the SEI. It appears that the composition and morphology of the SEI depends on a number of parameters such as the SOC of the electrode, the lithiation rate (scanning rate in electrochemical cycles), or the presence of contaminants (water). The latter was assessed by adding 50 ppm of water to the electrolyte. The presence of water most likely results in the hydrolysis of $LiPF_6$, which causes a morphologically more inhomogeneous SEI (pitted structure) and an SEI richer in fluorophosphates.

Overall, it appears that the Gen2 electrolyte is not an ideal choice for commercialization of Si-based electrodes because of its continuous decomposition upon cycling. Thus, alternative salts and solvents have been explored, and the beneficial effect of FEC and LiTFSI to improve the SEI stability is proposed in terms of mitigating the silicon corrosion. In addition, our initial studies suggest that, at prolonged galvanostatic cycling, the passivation behavior of the a-Si electrode improves by using glyme electrolyte/LiFSI salts compared to the more traditional Gen2 electrolyte.

Finally, the role of carbon coatings was analyzed. In a potential commercialization of Si-based anode materials, this aspect will also require optimization, because our studies demonstrate that drastically different Si solid-state transformation occurs during the electrochemical process due to the different types of carbon precursors and carbon coatings used on the same Si nanoparticles.

References

[1] E. Peled, J. Electrochem. Soc. 126, 2047–2051 (1979).
[2] M. Winter, Zeitschrift für Phys. Chemie. 223, 1395–1406 (2009).
[3] M.N. Obrovac, V.L. Chevrier, Chem. Rev. 114, 11444–11502 (2014).
[4] K.N. Wood, G. Teeter. ACS Appl. Energy Mater. 1, 4493–4504 (2019).
[5] Yoon et al., J. Electrochem. Soc. 164 (9), A2082 (2017).
[6] Parimalan et al., J. Phys Chem. C 121, 22733 (2017).
[7] Lu et al., ChemElectroChem 4, 2012–2018 (2017).
[8] Phillippe et al., Chem. Mat. 25, 394–404 (2013).
[9] Phillippe et al., J. Am. Chem Soc. 135, 9829–9842 (2013).
[10] J.G. Lee, J. Electrochem. Soc. 162, A1579–A1584 (2015).
[11] N. Azimi, et al, J. Electrochem. Soc. 162 (1), A64–A68, (2015).
[12] X. Ren, et al., Joule 3, 1662–1676, (2019).
[13] J. Miao, C.V. Thompson, J. Electrochem. Soc.165, A650–A656, (2018).
[14] J. Nanda, et al., Joule 3, 2001–2019, (2019).
[15] T. Hou, et al., Nano Energy 64, 103881 (2019).
[16] K. Xu, Chem. Rev. 104, 4303–4417, (2014).

Part 3: (Re)engineering of the Si/Electrolyte Interface via Molecular Interactions

Gabriel Veith (ORNL), Nate Neale (NREL), Jagjit Nanda (ORNL), Guang Yang (ORNL), Zhangxing Shi (ANL), Lu Zhang(ANL), Michael Carroll (NREL), Kae Fink (NREL), Yeyoung Ha (NREL), Sang-Don Han (NREL), Tingzheng Hou (UC Berkeley), Matthew Keyser (NREL), Zhifei Li (NREL), Gregory Pach (NREL), Ryan Pekarek (NREL), Kristin Persson (UC Berkeley), Shriram Santhanagopalan (NREL), Eric Sivonxay (UC Berkeley), Pauls Stradins (NREL),Bertrand J. Tremolet de Villers (NREL), Fernando Urias-Cordero (NREL), and Andriy Zakutayev (NREL), Katie Browning (ORNL), Mathieu Doucet (ORNL), James Brwning (ORNL)

Background

Over the course of this research project it has become increasingly clear that the standard electrolyte used in batteries comprised of a graphite anode, i.e., $LiPF_6$ in mixtures of ethylene carbonate and ethyl methyl carbonate (referred to as Gen2), is not stable with respect to silicon anodes. Furthermore, the variability of silicon with manufacturing processes leads to intrinsic surface instabilities that often mask other problems in cell stability (i.e., gassing, poor polymer adhesion, etc.). As detailed in the previous sections, the standard Gen2 electrolyte forms a non-passivating interface that changes with time and cycling conditions. These changes effectively eliminate the use of this standard electrolyte in future applications with silicon anodes.

As a result of these observations we have executed a series of collaborative studies to (1) understand the bonding and dynamics in standard electrolytes, (2) search for new electrolytes based on what appears to be stable surface moieties (based on chemical analysis), (3) continue developing tools to characterize and understand the interfacial chemistry *of all the components* (i.e., gas, soluble and insoluble species, polymers), and (4) develop new silicon materials with specific surface functionality designed to stabilize to Si particles and improve electrode fabrication (in close collaboration with the Si Deep Dive Consortium led by ANL). In addition, we have performed studies to explore the role of common impurities (i.e., water), which are known to contaminate cells where water-loving binders are used.

Throughout the course of this work, the team has made extensive use of model thin-film electrodes. These electrodes consist of single crystal silicon wafers with well-defined geometries and amorphous silicon films grown on battery-grade copper foil. To reduce the number of variables in the collaborative studies, these single crystal or amorphous silicon films were distributed from central locations (NREL and ORNL, respectively) and used exclusively for these studies. The chemistry of these films is documented in the Fiscal Year 2017 (FY17) and FY18 annual reports for those interested. This section of the SEISTa report is divided into three topical areas, all focused on the development of a predictive understanding of the silicon/electrolyte interface and application of this knowledge to developing new, robust, electrode materials. These sections are:

- Understanding and Designing New Electrolytes
- *In Situ* Understanding of the Growth and Evolution of the SEI on Model Electrodes
- Design of New Si Surfaces Based on Experimentally Validated Stable Chemical Moieties.

The work in these sections was done in collaboration with the results detailed in Parts 1 and 2 and should be viewed as part of the larger collaborative efforts between the teams.

Understanding and Designing New Electrolytes

Solvation Structures of Electrolyte

Based on our previous simulation work on the influence of fluorinated ethylene carbonate (FEC) on the solvation structure of ethylene carbonate (EC) electrolyte, we continue our work to include ethyl methyl carbonate (EMC), as used in the Gen2 electrolyte, to study how linear carbonate additions affect the properties of the electrolyte. Herein, we compare the difference in solvation structures between the EC electrolyte and the Gen2 electrolyte. The influence of FEC additive is also considered and compared between the EC and Gen2 electrolyte.

The solvation structures of EC and Gen2 electrolyte are compared by conducting molecular dynamics simulations for EC (1.2 M $LiPF_6$ in EC) and Gen2 (1.2 M Li in EC:EMC (v/v 3:7)) electrolytes. Figure 37 shows the three representative solvation structures for Gen2 electrolyte, which are solvent-separated ion pairs (SSIP), contact ion pairs (CIP), and aggregates (AGG). For all three structure categories, both EC and EMC participate in the formation of the first solvation shell. Meanwhile, both EC and EMC coordinate with Li^+ ions via the carbonyl oxygen but not the alkoxy oxygen.

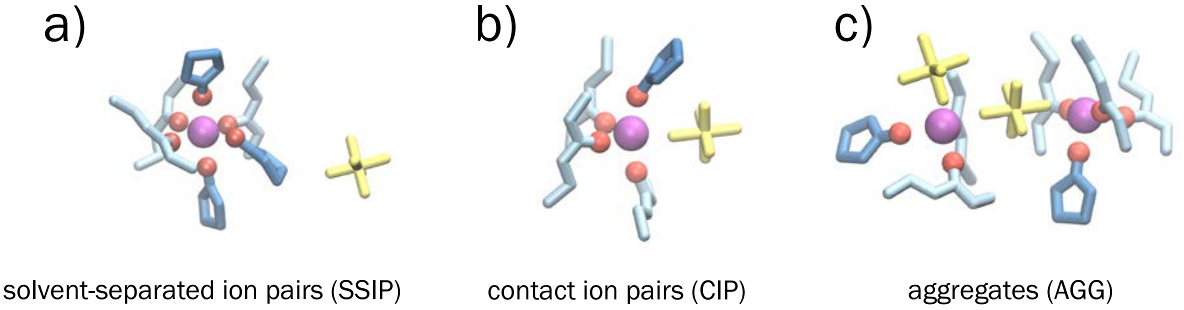

Figure 37. Three representative solvation structures in Gen2 electrolyte: (a) solvent-separated ion pairs (SSIP), (b) contact ion pairs (CIP), and (c) aggregates (AGG). The light blue, dark blue, and light yellow line representations denote the EMC, EC, and PF_6^- clusters, respectively. The purple and red ball representations denote Li ions and coordinating carbonyl O atoms, respectively.

While these three solvation structures also appear in the EC electrolyte, the proportion of each category changes between the 100% EC and Gen2 electrolyte, as analyzed by the molecular dynamic statistics. For the EC electrolyte, 86.95% of the Li ions form SSIP, while in the Gen2 electrolyte, SSIP only comprises 36.81% of the total Li+ ions. CIP and AGG constitute 31.79% and 31.4% in the Gen2 electrolyte, respectively, meaning that in the Gen2 electrolyte the Li^+ cations and PF_6^- anions are more associated, while CIP and AGG represent 11.03% and 2.02% in pure EC, respectively. The higher SSIP population in the EC electrolyte indicates that the EC electrolyte has more ionic conduction carriers than the Gen2 electrolyte.

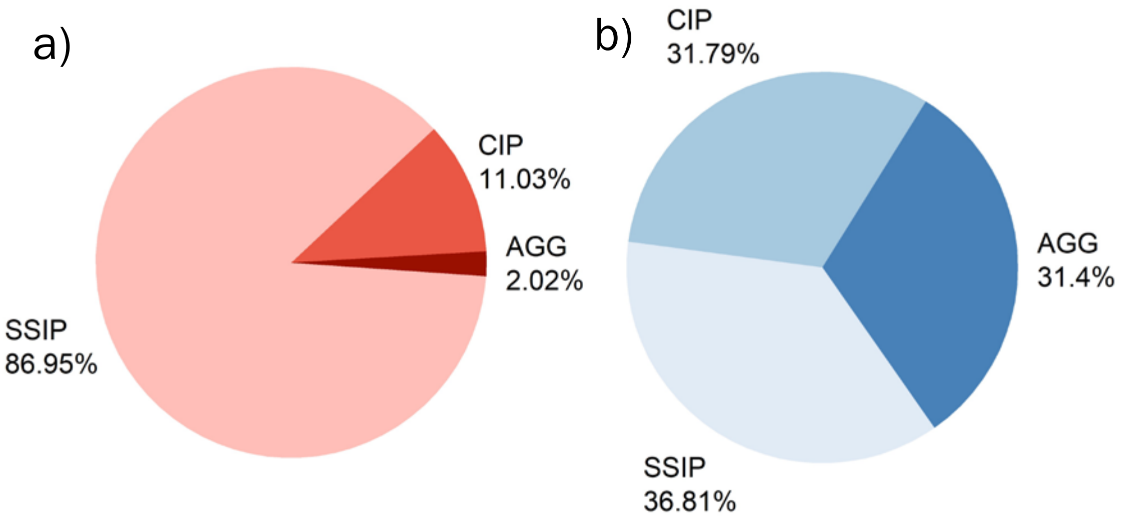

Figure 38. The proportions of SSIP, CIP, and AGG in (a) the EC electrolyte and (b) the Gen2 electrolyte

The averaged solvent coordination numbers for these three species are statistically analyzed. For both the EC and Gen2 electrolyte, the total solvent coordination number decreases as a PF_6^- anion coordinates with Li to form CIP and additional PF_6^- anodes coordinate with Li to form AGG. Interestingly, in the Gen2 electrolyte only the coordination number for EC decreases while that for EMC is preserved between species, indicating that only the EC molecules are substituted by PF_6^-. This may be attributed to the bulky shape of EMC, which results in larger Lennard-Jones forces that confine or stabilize the coordinating structure, and renders EMC-Li^+ a stiffer configuration. More detailed study of this phenomenon will be conducted in the future.

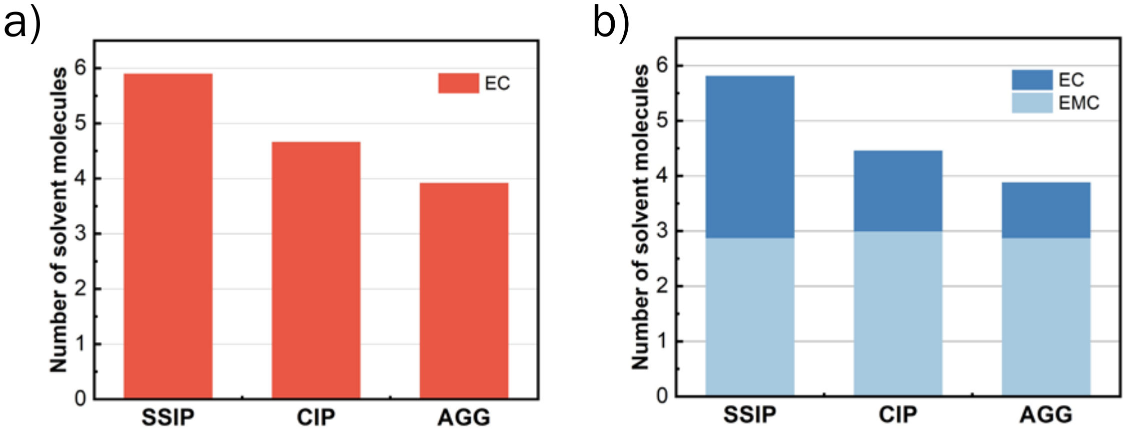

Figure 39. The coordination number of solvent molecules for SSIP, CIP, and AGG species in (a) EC electrolyte and (b) Gen2 electrolyte

The detailed speciation of AGG in the Gen2 electrolyte is further analyzed, as shown in Figure 40. Among the 31.4% of the AGG species, 9% are AGG1 form with 2 Li^+ and 1 PF_6^-, which is +1 charged. Meanwhile, the AGG2 form with neutral charge and the AGG3 form with −1 charge take up 8% and 7%, respectively. The remaining forms, including the AGG4 and AGG5, have a percentage of 7%. Overall, at least 19% of the 31% AGG species are charged species, which will contribute to the ionic conductivity. Subsequently, while the EC electrolyte has a much higher SSIP ratio than the Gen2 electrolyte, more than half of the AGG species in the Gen2 electrolyte narrow the gap of the proportion of ionically conductive solvation species.

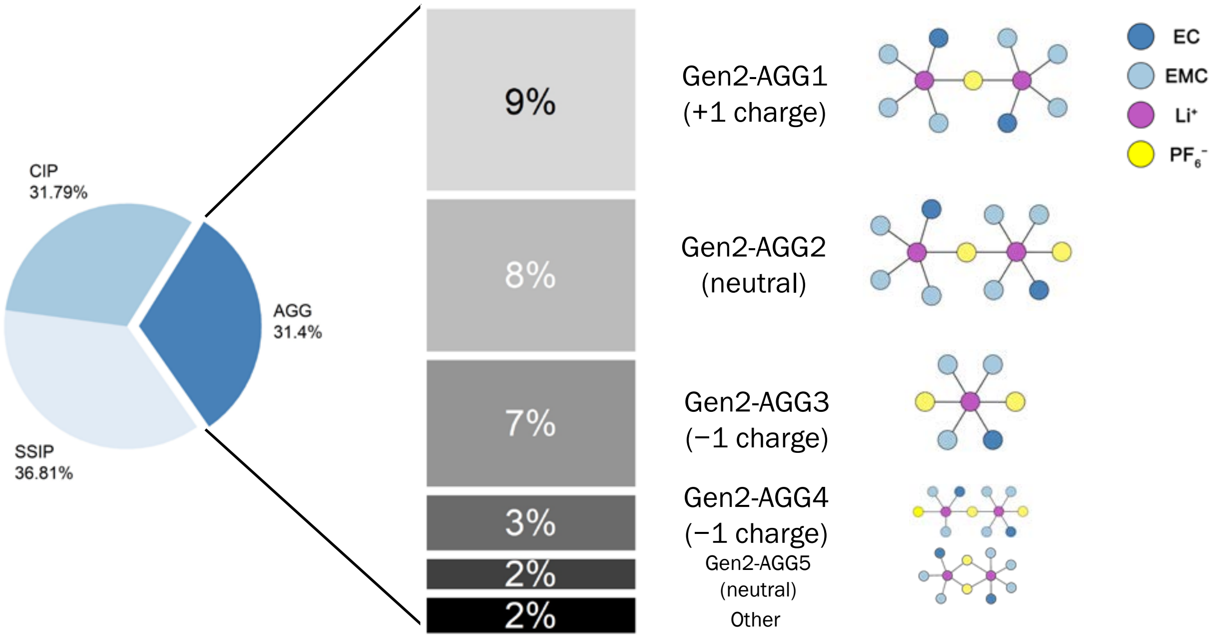

Figure 40. AGG species in the Gen2 electrolyte

To compare the influence of FEC additive on the solvation structure of the EC and Gen2 electrolyte, 10% of FEC are added into the systems which make the ECF (EC + 10 mol% FEC) and the GenF (Gen2 + 10 mol% FEC) model electrolyte. The proportions of CIP, SSIP, and AGG of the ECF and GenF follow the same trend as the EC and Gen2 electrolyte, as shown in Figure 41. For the ECF electrolyte, 84.73% of the Li^+ ions form SSIP, while in the GenF electrolyte, SSIP takes up 38.37% of the total Li^+ ions. The reason why the SSIP ratio decreased in the ECF and increased in the GenF might be attributed to the fact that FEC has a solvating ability that is between EC and EMC. Accordingly, the CIP and AGG ratios of the ECF change to 14.39% and 0.88%, respectively, while those of the GenF change to 34.04% and 27.59%. Consequently, the ionic conduction ability of ECF and GenF is supposed to be similar to the EC and Gen2 electrolyte. Detailed analysis of the conduction and transport properties will be addressed in the future.

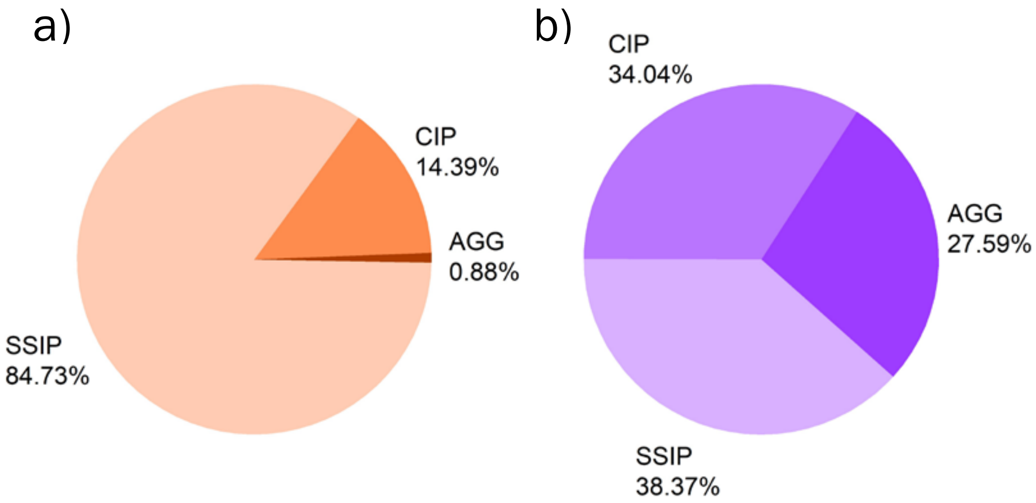

Figure 41. The proportions for SSIP, CIP, and AGG in (a) the ECF electrolyte and (b) the GenF electrolyte

The averaged solvent coordination number for the three species in the ECF and GenF electrolyte are also analyzed. For both the ECF and GenF electrolyte, the total solvent coordination number follows a similar trend as in the EC and Gen2 electrolyte, namely that it decreases when PF_6^- coordinates with Li to form CIP and AGG. Analogously, the EC and FEC molecules are substituted by PF_6^- for both the ECF and GenF electrolyte when forming CIP and AGG, in the sense that EC and FEC have similar structures. Meanwhile, the coordination number of EMC-Li remains ~3 for all the species in the GenF electrolyte.

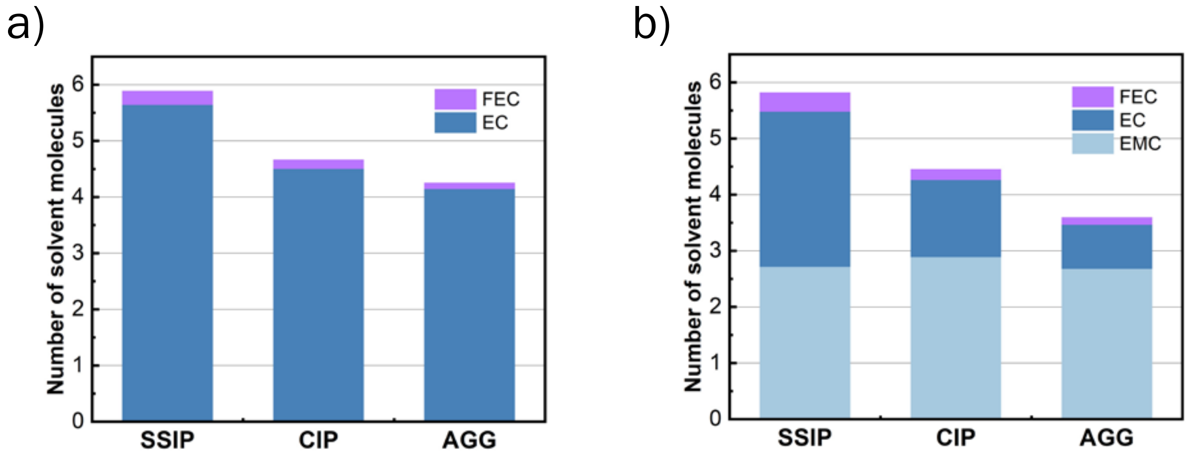

Figure 42. The coordination number of solvent molecules for SSIP, CIP and AGG species in a) ECF electrolyte and b) GenF electrolyte.

In conclusion, using a classical molecular dynamics simulation, we have found that the Gen2 electrolyte favors a much higher CIP ratio (>30%) and AGG ratio (>30%), while the EC electrolyte exhibits nearly 90% SSIP and 10% CIP. Hence, the EC electrolyte presents more ionic conduction carriers as compared to the Gen2 electrolyte. The EC molecule is substituted by PF_6^- for both EC and Gen2 electrolyte when forming CIP and AGG, indicating the EMC solvent forms a more stable binding with Li^+. Further investigations will be conducted to reveal the reason why EMC is favored to coordinate, as compared to, e.g., the PF_6^- anion. One proposed method is to calculate the EMC-Li^+ and EC-Li^+ pair desolvation energy as a function of atomic distance using density functional theory (DFT). The energy difference will be compared to the dissociation constant observed in the molecular dynamics (MD) results. Moreover, the electron density analysis will also be performed to help rationalize the energy calculation.

In Gen2 electrolyte, at least 19% out of 31% AGG species are charged species, which will contribute to the ionic conductivity. Further calculations of the conduction and transport properties of the Gen2 electrolyte will be addressed in the future. The influence of FEC additive on the solvation structure of the ECF and GenF electrolyte is also compared. It is found that FEC will participate in first solvation shell of the GenF electrolyte, as has been found in the ECF. The proportion of FEC in the solvation shell exhibits a similar changing trend as EC when Li coordinates with PF_6^-, which could be explained by their structural similarity.

New Electrolytes for Si Anodes

As noted previously, the Gen2 electrolytes are not stable. One approach to address this issue is to explore solvents and salts other than Gen2 electrolytes that could potentially demonstrate better passivating properties, specifically during early electrochemical cycles. Earlier study by the team investigating solid-electrolyte interphase (SEI) formation on amorphous silicon (a-Si) thin film indicates that polymeric ether components such as poly(ethylene oxide) (PEO) are formed during early galvanostatic cycles (GC) [1], enabling a certain degree of elasticity to buffer the volumetric change of the Si anodes. We thus hypothesize that the glyme-based system can potentially be reduced to polymeric ether-type species during the initial SEI formation, providing better passivation. Initial studies in Q3 showed that glymes have higher parasitic currents, especially during early SEI formation, as compared to their carbonate electrolyte counterpart, Gen2. However, the parasitic currents of glyme and carbonates became comparable at the fifth GC cycle. This motivates us to continue the research on the passivation behavior of the glyme electrolytes on Si at prolonged GC cycles in Q4. For this study, Gen2 and Gen2+FEC electrolytes were used as the benchmark. The 50 nm amorphous (a-Si) thin film was used as the model anode and lithium metal was used as a counter electrode.

Among all electrolytes, Gen2 exhibited the highest discharge capacity during the early GC cycling stage, as shown in Figure 43. This agrees with data indicating that Gen2 had the lowest parasitic current for the first five GC cycles, as reported in Q3. The addition of 10 wt% FEC in Gen2 stabilized the SEI formed on a-Si, as demonstrated by the improved capacity retention (85% as compared to 31% for Gen2) during prolonged GC cycles. $LiPF_6$-DME electrolyte exhibited the overall lowest capacity among all electrolytes, agreeing with its unstable parasitic current as observed in the GC-CA test in Q3. Both the LiTFSI-DME and LiFSI-DME glyme electrolytes exhibited a lower discharge capacity compared with Gen2+FEC. A fluoroether, 1,1,2,2-tetrafluoroethyl-2,2,3,3-tetrafluoropropyl ether (TTE), was further used as an additive in glyme electrolytes. While the addition of a small amount (10 wt%) of TTE didn't seem to stabilize the a-Si well (Figure 43), a special formula of LiFSI-3DME-3TTE (the molar ratio is 1:3:3) performed best among all electrolytes, as it showed the highest specific capacity at prolonged GC cycles, with the largest capacity retention at 92%, indicative of a more robust SEI formation using this special glyme electrolyte formula.

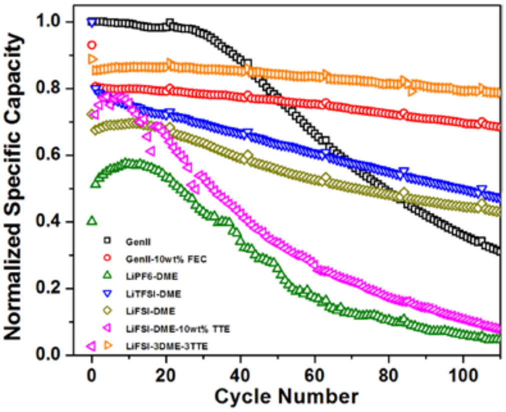

Figure 43. Variation of normalized discharge capacity with cycle number (up to 110 cycles) of the a-Si anodes using multiple electrolytes at a 1 C equivalent current density

We further explored the surface morphology of the a-Si anodes after prolonged cycles using a scanning electron microscope (SEM). The a-Si anodes cycled in Gen2 and Gen2+FEC electrolytes exhibited crack patterns, as shown in Figure 44. For the LiFSI-DME electrolyte, the a-Si surface was covered by a patch-like SEI layer. This may indicate the existence of an underdeveloped passivation layer on the a-Si surface. The a-Si anode cycled in LiFSI-3DME-3TTE glyme electrolyte had a much smoother and crack-free surface after 110 GC cycles, demonstrating a more conformal passivation layer formed on the a-Si surface. This agrees well with the GC cycling performance in Figure 43, indicative of a more stable SEI formation for LiFSI-3DME-3TTE during prolonged GC cycling.

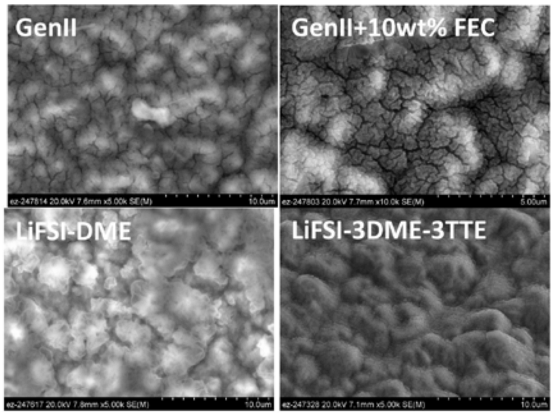

Figure 44. SEM micrograph of the a-Si anodes after 110 cycles

The surface chemistry of the a-Si anodes during early cycles and after prolonged cycles was explored further by using energy-dispersive X-ray spectroscopy. The surface elements in the SEI layer include carbon, oxygen, fluorine, silicon, and sulphur, as shown in Figure 45. Intriguingly, the C-O ratio is close to 2:1 for Gen2 electrolyte after 5 cycles, agreeing with that of the PEO oligomer SEI species on a-Si in an early study [1], as PEO is composed of -CH$_2$-CH$_2$-O repeating units. After prolonged cycles, the C-O ratio for Gen2 and Gen2+FEC is close to 1:1. This may indicate the increased abundance of C=O, agreeing with evidence that carbonate electrolytes have enriched carboxylate SEI species [1]. The existence of Li$_2$CO$_3$ and lithium ethylene dicarbonate (LEDC) cannot be ruled out. In contrast, the C-O ratio for LiFSI-3DME-3TTE glyme electrolyte was increased to 1:2 after prolonged cycling, indicating enrichment of the organic PEO-like SEI species. This observation agrees fairly well with the infrared spectra of various a-Si samples GC cycled in glyme-based electrolytes, as reported in Q3. For glyme-based electrolytes, the abundance of the fluorinated species was not increased upon adding more TTE. This indicates that the resource of the fluorinated species in the SEI layer on a-Si may stem from the decomposition of the LiFSI salt instead of the TTE additive.

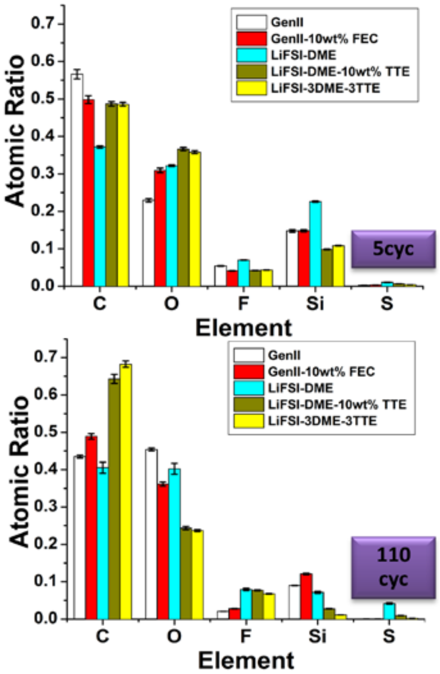

Figure 45. Elemental analysis of the a-Si anodes after 5 cycles and after 110 cycles. Error bars indicate the standard deviations of the three measures on three different locations of each sample.

Future plans for the research include elucidating and consolidating the surface chemistry of the a-Si after the short and prolonged galvanostatic cycling test using X-ray photoelectron spectroscopy (XPS). Exploring the SEI formation mechanisms following different electrolyte reaction paths in different electrolytes is another future focus. The effect of the electrolyte coordination chemistry will be evaluated for the LiFSI-3DME-3TTE using a similar method reported by Persson et al. [2]. Proton nuclear magnetic resonance (NMR) has been measured on various electrolytes after GC cycling at different stages to explore the dissolved SEI species in the electrolytes. Those data are being analyzed and will be reported in due course. In summary, we evaluate the passivation behaviour of glyme electrolytes on a-Si thin-film anodes for prolonged cycles. The galvanostatic cycling profile indicates that LiFSI-3DME-3TTE passivates the a-Si better. The energy-dispersive X-ray (EDX) elemental analysis on a-Si anodes indicate that the GenII electrolyte passivation results in formation of enriched carbonated species such as lithium carboxylate, Li_2CO_3, and LEDC-rich SEI. In contrast, using glyme-based electrolytes leads to the formation of the PEO-like SEI on the a-Si surface.

In Situ Understanding of the Growth and Evolution of the SEI on Model Electrodes

Synthesis of Reference Compounds

Through the course of this work the team has identified the formation of lithium ethylene dicarbonate as an SEI formation product that forms upon lithiation on the Si anode but dissolves into the electrolyte upon cycling. This work is to synthesize the known SEI components such as lithium methyl carbonate (LMC) and lithium ethylene dicarbonate (LEDC), and to characterize their possible roles in the SEI formation process. Specifically, they will be used as additives in the next section ("Design of New Si Surfaces Based on Experimentally Validated Stable Chemical Moieties") and as additives to the electrolyte to drive saturation.

Synthesis of Lithium Methyl Carbonate (LMC)

Approach 1: Lithium methoxide (0.75 g, 20 mmol) and dry methanol (20 mL) were added to an oven-dried Schlenk flask under argon. Excess amount of analytical grade carbon dioxide (CO_2) was then introduced to the solution. The mixture was stirred at room temperature for 24 h, concentrated, and dried in vacuum to give LMC as a white solid (yield: 1.6 g, 97%). The Fourier-transform infrared spectroscopy (FTIR) data matched those reported results, as seen in Figure 47 [3]. The synthesis is summarized in Figure 46.

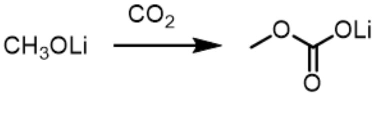

LMC

Figure 46. Synthesis of LMC

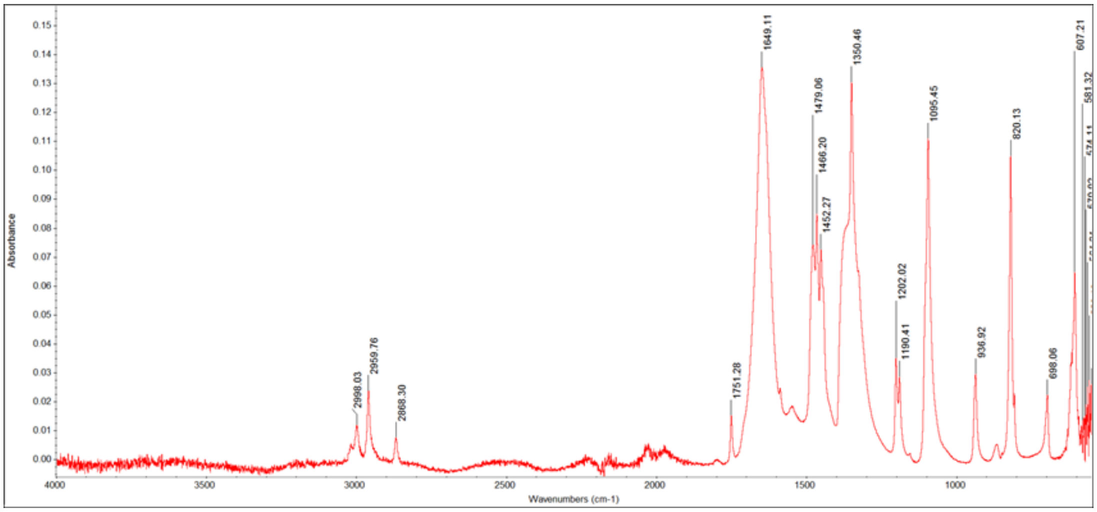

Figure 47. FTIR data collected for LMC

Approach 2: Lithium iodide (0.27 g, 2.0 mmol) and dry dimethyl carbonate (10 mL) were added to a scintillation vial under argon. The mixture was stirred at room temperature for 24 h, filtered, washed with diethyl ether, and dried in vacuum to give LMC as a light yellow solid (yield: 0.048 g, 29%). The characterization data matched those reported for this compound [4]. The synthesis is summarized in Figure 48. However, the yield of this method is very low, and the product might have some iodine contamination.

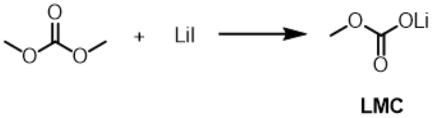

Figure 48. Synthesis of LMC

Synthesis of Lithium Ethylene Dicarbonate (LEDC)

LEDC was synthesized following the procedure in Figure 49. Dry diethyl ether (40 mL) and *n*-butyllithium (1.6 M in hexane, 10 mL) were added to an oven-dried three-neck flask under argon. Ethylene glycol (0.49 g, 7.9 mmol) was then added slowly. The mixture was stirred for 2 h before excess amount of analytical grade CO_2 was introduced. The resulting suspension was then stirred for 1 week under CO_2. The precipitates were filtered, washed with acetonitrile, and dried to give a white solid (yield: 0.63 g, 49%). The characterization data matched those reported for this compound [5]. Resulting FTIR data are shown in Figure 50. However, a recent paper claims that lithium ethylene monocarbonate (LEMC) was formed instead of LEDC when using this method [6].

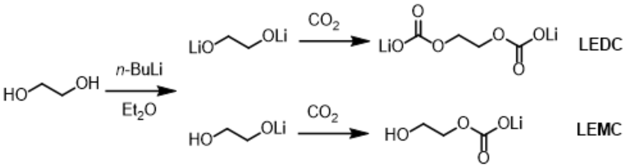

Figure 49. Synthesis of LEDC

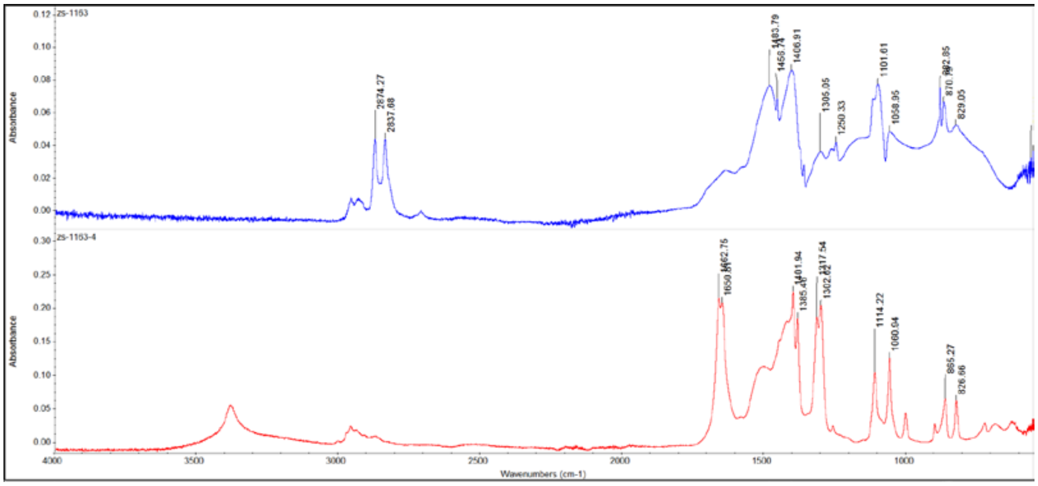

Figure 50. FTIR spectra of the synthesized LEDC, stirred under CO_2 for 1 day (blue curve) and 7 days (red curve)

It should be noted that NMR spectra are not very useful determining the structures, as most of the compounds are not very soluble and are sensitive to water. Trace amounts of water can lead to hydrolysis of the limited amount of compounds dissolved in NMR solutions, which may lead to confusing chemical shift results. These data are presented in Figure 51.

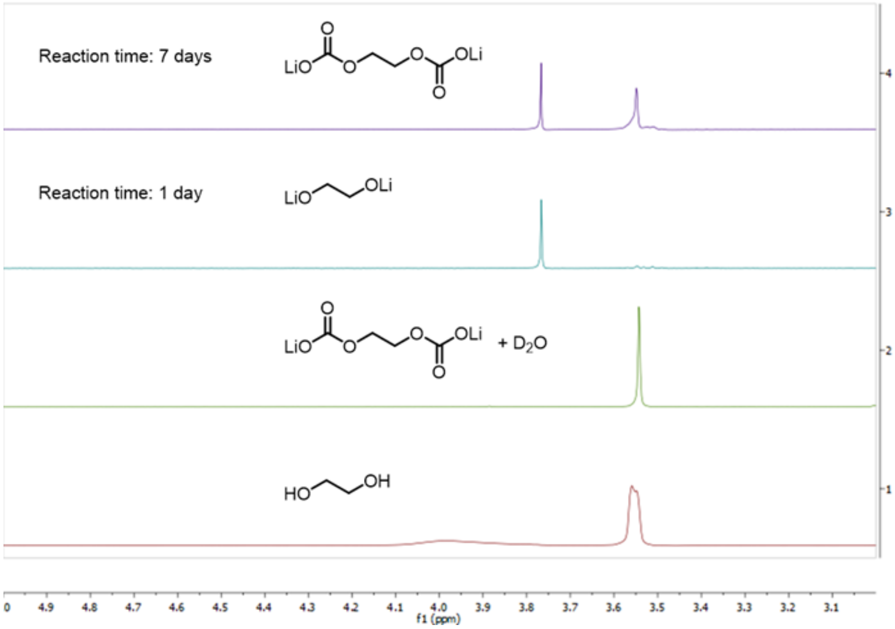

Figure 51. NMR spectra of LEDC compounds under various conditions

Operando ATR-FTIR Spectroscopy

We have continued our development of the operando attenuated total reflectance-Fourier transform infrared (ATR-FTIR) spectroelectrochemical characterization instrument begun in FY18. Prior work in this area by Phil Ross and coworkers [7,8] showed that the components of the SEI vary significantly as a function of applied voltage. In that work, electrolyte composed of 1.0 M $LiPF_6$ in EC:DEC (1:2, v/v) was used in conjunction with native oxide (SiO_x)-covered Si wafer. At 1.3 V, electrolyte reduction (DEC) to diethyl 2,5-dioxahexane dicarboxylate (DEDOHC) was found, whereas at 5 mV, selective electrolyte reduction (EC) to lithium ethylene dicarbonate (LiEDC) occurred [9]. Cycling data showed an SEI composed primarily of DEDOHC. Our goal is to extend this study of SEI dissolution and growth using other model samples (H-terminated Si, native SiO_x-terminated, and molecularly functionalized Si wafers) and eventually extend this to three-dimensional Si NP-based electrodes assembled on the Si wafer substrate.

Our new setup provides significant distinguishing features relative to that of Ross and coworkers, who used several milliliters of electrolyte in their operando experiments. Since it is well known that SEI dissolution and growth is strongly dependent on the electrolyte volume, we designed our ATR-FTIR cell to be effectively that of a coin cell, where a Celgard separator is placed directly on top of the double-polished Si wafer. The Si wafer in this configuration doubles as the ATR crystal *and* the working electrode. A Li metal foil counter electrode is placed on top of the Celgard separator, followed by a stainless-steel plate and rod. The stainless-steel plate and rod apply pressure to the electrode assembly to more closely mimic that of a coin cell battery, as well as to minimize the air gap between the ZnSe ATR prism and the double-polished Si wafer.

Using this new “coin cell ATR-FTIR” configuration, in Q1FY19 we discovered that our cycling data had a significant voltage offset due to poor contact to the Si wafer substrate. We estimate that a 1–2 kΩ resistor owing to this bad contact can account for the ~300 mV offset observed in the voltage profiles for our current density and galvanostatic cycling data (Figure 52).

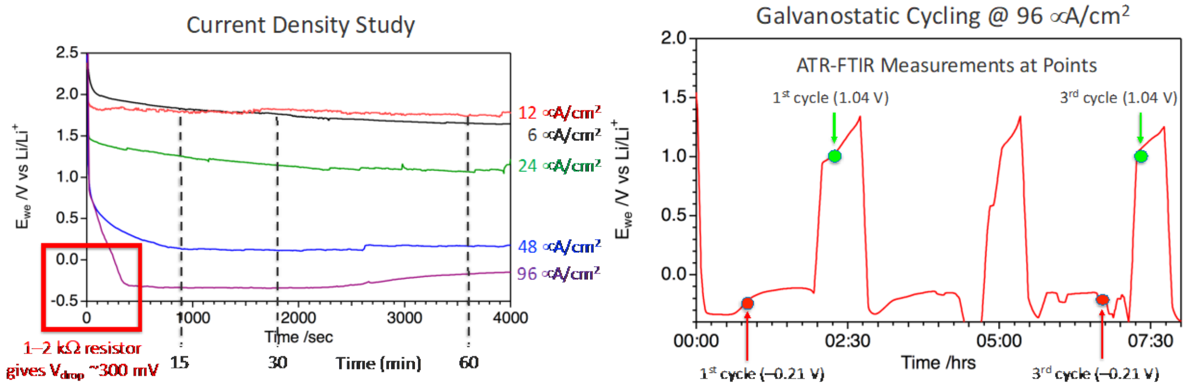

Figure 52. Left: Current density study for 5–10 Ω • cm resistivity Si wafers in the ATR-FTIR spectroelectrochemical cell. A voltage drop of ~300 mV is caused by poor contact to the Si wafer. Right: Cycling behavior of the same cell indicating points where ATR-FTIR spectra were collected (see Figure 38 for ATR-FTIR data).

In Q2FY19 we conducted a further analysis of the 2017 paper by Ross and coworkers describing related experiments [2]. We found that a 5 Ω•cm Si wafer (same doping density as in the 2017 work) results in a large potential drop due to the resistivity of the wafer. When applying sufficiently negative potentials to drive lithiation in the hundreds of μAcm^{-2} range (as seen in the cyclic voltammograms in that paper [9] and Figure 53) and a measured resistivity of ~1 kΩ from the contact to the wafer center (where the IR beam is incident), Ohm’s Law tells us to expect a voltage drop of several hundred mV. This is exactly what is observed experimentally in our system, as shown in Figure 53.

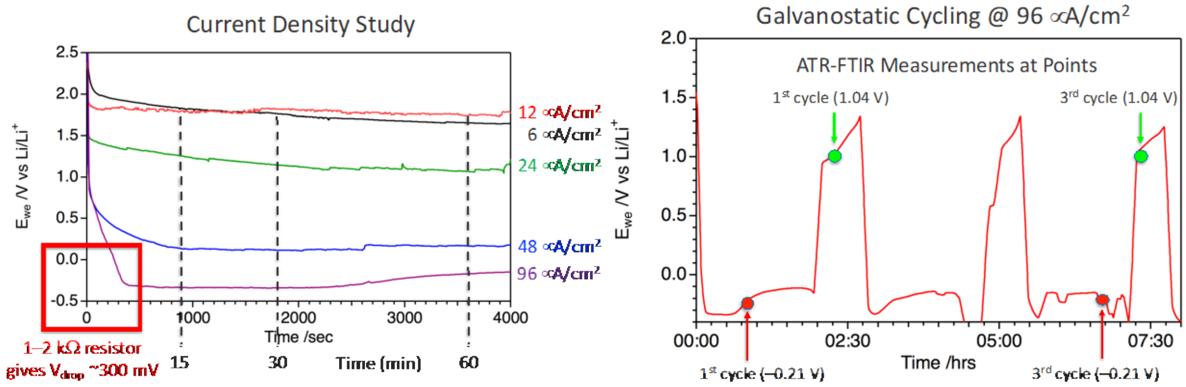

Figure 53. Left: Current density study for 5–10 Ω•cm resistivity Si wafers in the ATR-FTIR spectroelectrochemical cell. A voltage drop of ~300 mV is caused by the resistivity of the low doping density Si wafer. Right: Cycling behavior of the same cell indicating points where ATR-FTIR spectra were collected (see Figure 38 for ATR-FTIR data).

Thus, we worked with our silicon photovoltaic (PV) experts to develop a protocol to selectively surface-dope the crystalline Si wafer. This provided the necessary IR transparency required to collect ATR-FTIR spectra while also allowing excellent electrochemical behavior. Figure 54 displays representative cycling data from 1.5 to 0.01 V, demonstrating the high-quality electrochemical response provided by our critical FY19 breakthrough—the surface p$^+$-doped Si wafer. These data also demonstrate that substantial current is passed prior to the crystalline Si lithiation potential (~115 mV), indicative of SEI growth.

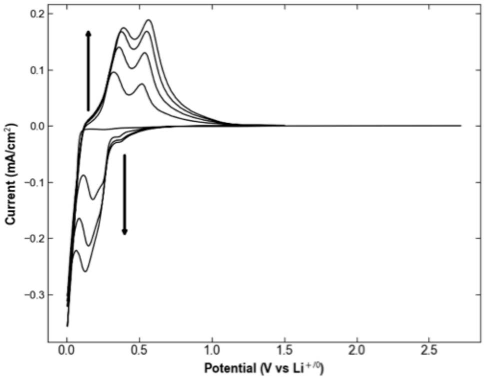

Figure 54. Left: Cyclic voltammograms for heavily surfaced p$^+$-doped Si wafers (bulk resistivity 5–10 Ω•cm) in the ATR-FTIR spectroelectrochemical cell. These surface-doped wafers feature an ~100 nm-deep surface p$^+$ layer (doping density 10^{19}–10^{20} cm^{-3}), resulting in a highly conductive working electrode (<1 mΩ•cm).

Our initial experiments directly targeted the SEISta FY19 Milestones by conducting potentiostatic holds at a range of potentials (open-circuit voltage, 1.0 V, 0.7 V, 0.4 V, 0.15 V, 0.1 V vs. Li$^{+/0}$) on native SiO$_x$-terminated p$^+$-Si wafers. We found that at 0.1 V vs. Li$^+$/Li, lithiation of the Si wafer anode quickly eliminates its reflective nature and the ATR-FTIR signal is lost. Given that cyclic voltammograms of SiO$_x$-terminated Si wafers show minimal current is passed at potentials higher than 0.5 V vs. Li$^+$/Li (Figure 55, left), we focused on the low potential regions of 400 and 150 mV vs. Li$^+$/Li for all comparative studies. Initial experiments in Q3FY19 were conducted on wafer silicon terminated with native oxide (SiO$_x$) by collecting *in situ* FTIR spectra during potentiostatic holds at early SEI growth potentials (400 and 150 mV vs. Li/Li$^+$), and in Q4FY19 we performed the same experiments on hydrogen-terminated silicon surfaces (SiH). Accordingly, this allowed us to discern the effects of surface termination on the near-surface electrolyte composition as a function of early-stage SEI growth.

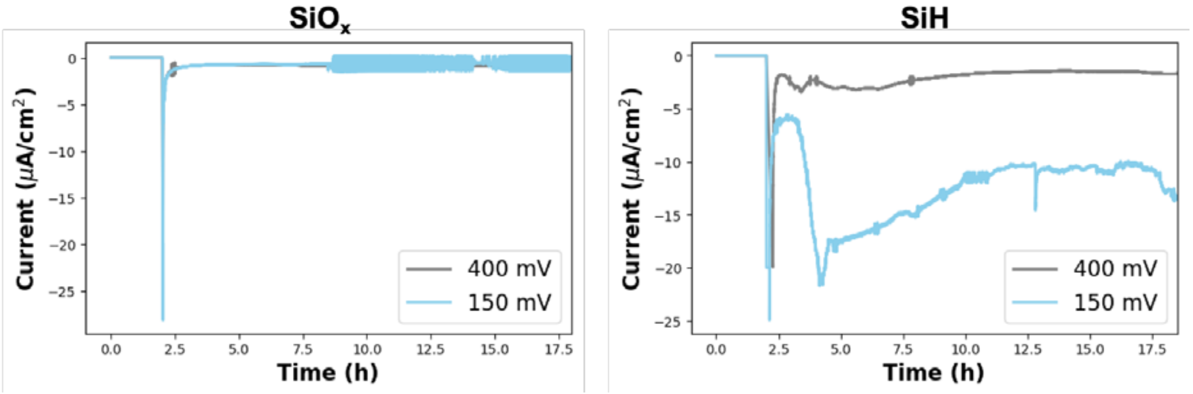

Figure 55. Chronoamperograms of silicon wafers with native oxide (left, SiO_x) and hydrogen terminated (right, SiH) at 400 and 150 mV vs. Li/Li$^+$ (gray and blue, respectively). The wafers used in this experiment feature a highly p$^+$-doped surface layer (doping density = 10^{19}–10^{20} cm^{-3}) to allow for high conductivity and IR transparency. The chronoamperograms show the greater reactivity of the SiH samples compared to SiO_x.

Comparing the chronoamperograms for SiO_x- and H-terminated Si wafers shows that the SiH surface is far more reactive (shown in Figure 55), consistent with our prior chemical reactivity studies. For the SiO_x-terminated wafers (Figure 55, left), the current quickly decays to –1 µA/cm^2 in the first 30 min for both 400 and 150 mV vs. Li/Li$^+$. In stark contrast, the SiH-terminated surfaces (Figure 55, right) show larger currents over the entire 18 h in each experiment, signaling a much greater reactivity. The current of the SiH sample held at 400 mV vs. Li/Li$^+$ decays to –2.5 µA/cm^2 in the first 30 min of the potentiostatic hold, then decreased over the 18 h. At lower potentials (150 mV vs. Li/Li$^+$), the SiH sample exhibits a strikingly different current profile. In the first 30 min, the current density reaches –8 µA/cm^2, but instead of decaying gradually, as occurs at 400 mV, the current instead *increases* before decreasing and reaching a steady-state current of approximately –14 µA/cm^2. The results highlight the greater reactivity and slower passivation of the etched SiH surface relative to the SiO_x-terminated surface, and further confirms the major FY19 SEISta project conclusion that both SiH and SiO_x are bad actors in Si anode SEI stability.

Finally, in Q3 we determined that the *in situ* ATR-FTIR experiment in its present configuration is probing near-surface changes to the electrolyte, *not* the SEI itself. In Figure 56 we show ATR-FTIR spectra of the C=O stretching region of the SiH samples corresponding to the potentiostatic holds depicted in Figure 55. We highlight the C=O region as it contains signatures of the carbonates in the electrolyte where significant changes are observed. These data show that uncoordinated EMC is preferentially lost (as compared to coordinated EMC or uncoordinated/coordinated EC) in the near-surface electrolyte region. It is unclear whether this is due to direct decomposition of uncoordinated EMC or the result of Li$^+$-coordinated EMC and subsequent equilibration (where uncoordinated EMC replaces lost Li$^+$-coordinated EMC due to Le Chatlier's principle). Further, in the 150 mV vs. Li/Li$^+$ sample we observe an *increase* in the Li$^+$-coordinated EC peak, which may be the result of a similar equilibrium process. This exciting result reveals the components of the Gen2 electrolyte that contribute to early-stage SEI growth, where it is clear that EMC is more reactive with the silicon surface and likely is a greater constituent of the early-stage SEI than EC. Future work will add additional components to this experimental configuration: (1) we will attempt to develop a similar experiment on a three-dimensional electrode composed of Si nanocrystals (NCs), thereby increasing signal to noise of the SEI relative to the background electrolyte signal; and (2) introduce additives to the electrolyte (FEC, MgTFSI, etc.) to explore how these species modify the electrolyte decomposition reactions resulting in the early-stage SEI.

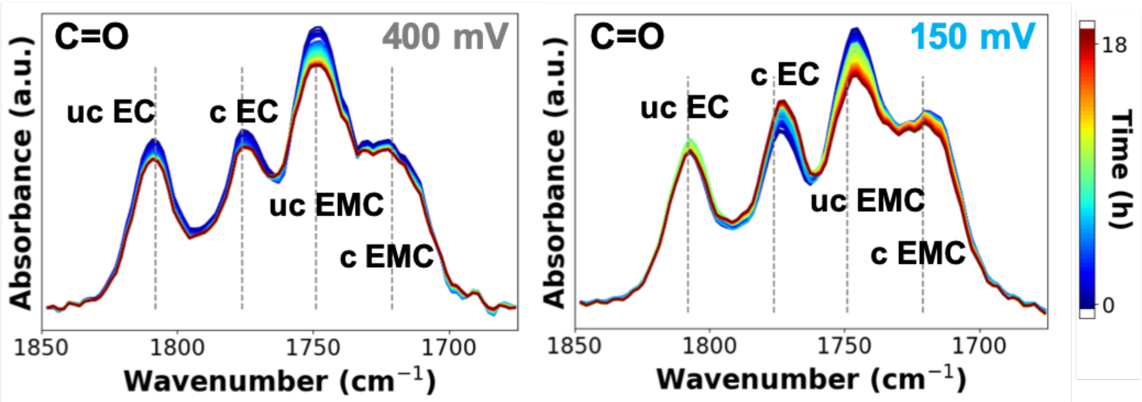

Figure 56. Carbonyl region of FTIR spectra corresponding to the chronoamperograms shown in Figure 52, showing loss of uncoordinated (uc) EMC relative to other electrolyte components during the 18-hour potentiostatic holds.

Electrolyte Characterization via *In Situ* Raman

Raman spectroscopy is a powerful tool for studying both electrodes and electrode-electrolyte interphase (EEI), as it provides both structural and chemical information. In addition, it is a nondestructive analysis and can characterize many types of samples including an amorphous thin film [9,10]. In this study, we report an *in situ* surface-enhanced Raman spectroscopy (SERS) technique with a modified cell configuration, which enabled us to successfully monitor the reversible electrochemical behavior of the Si anode and newly formed alkyl carboxylates (R-COO$^-$), possibly resulting from electrolyte decomposition within the silicon-electrolyte interphase (SiEI).

Reference Spectra and Peak Assignment

To aid our analysis of the *in situ* Raman measurements, we first constructed a reference library of Raman spectra for components of the Gen2 electrolyte—1.2 M lithium hexafluorophosphate ($LiPF_6$) in ethylene carbonate (EC):ethyl methyl carbonate (EMC) (3:7 wt%,)—used in this study. Detailed peak assignments for the electrolyte components and their coordination with Li$^+$ cations in a standard Gen2 electrolyte are presented in Table 4.

Table 4. Raman Peak Assignments

Raman Band Center (cm^{-1})	Assignment	Species of Origin	Reference(s)
380		EMC	this work
401		EMC	this work
513		EMC	this work
530		EMC	this work
716	o, O-C-O	EC	[11,12]
729	o, O-C-O	EC···Li$^+$	[11,12]
741	υ, P-F	PF_6^-	[11,13]
838		EMC	this work
877		EMC	this work
892	β, C-C	EC	[11,12]
904		EC···Li$^+$	[3]
932	δ, O-C-O	EMC	[5], this work
938	δ, O-C-O	EMC···Li$^+$	[5], this work

Raman Band Center (cm^{-1})	Assignment	Species of Origin	Reference(s)
973	υ, C-C	EC	[2,3]
1008		EMC	this work
1070	υ, C-C	EC	[2], this work
1092		EMC	this work
1116		EMC	this work
1164		EMC	this work
1201		EMC	this work
1225	τ, CH_2	EC	[2], this work
1275		EMC	this work
1304		EMC	this work
1455		EMC	this work
1483	δ, CH_3	EC	[2]
1748	υ, C=O	EMC	[5], this work
1771	υ, C=O	EC	[2]
1795		$\text{EC}\cdots\text{Li}^+$	this work
1802	υ, C=O	EC	[2]
υ = stretching; δ = bending; o = ring breathing; β = ring deformation; τ = twisting			

Electrochemical Performance and Corresponding SERS Spectra

The *in situ* electrochemical cell (ECC-Opto-Std, EL-Cell GmbH) was assembled with a Si working electrode (amorphous Si (a-Si) thin film deposited on a Cu substrate) and a Li metal foil as counter/reference electrodes in a coin-type cell configuration. The cell was then filled with a Gen2 electrolyte. After two hours of rest (for enough wetting of Si electrodes with the electrolyte) at the open-circuit voltage (OCV), the cell was cycled galvanostatically at the current of 15 μA in the voltage range of 0.01–1.5 V (vs. Li/Li$^+$, hereafter). During cycling, Raman spectra were collected at specific voltages (based on previous voltage profile studies) using a Raman microscope equipped with a 632.8-nm He-Ne laser. The results of electrochemical cycling profiles (the 1st and 2nd cycles) and corresponding Raman spectra are presented in Figure 57 (b).

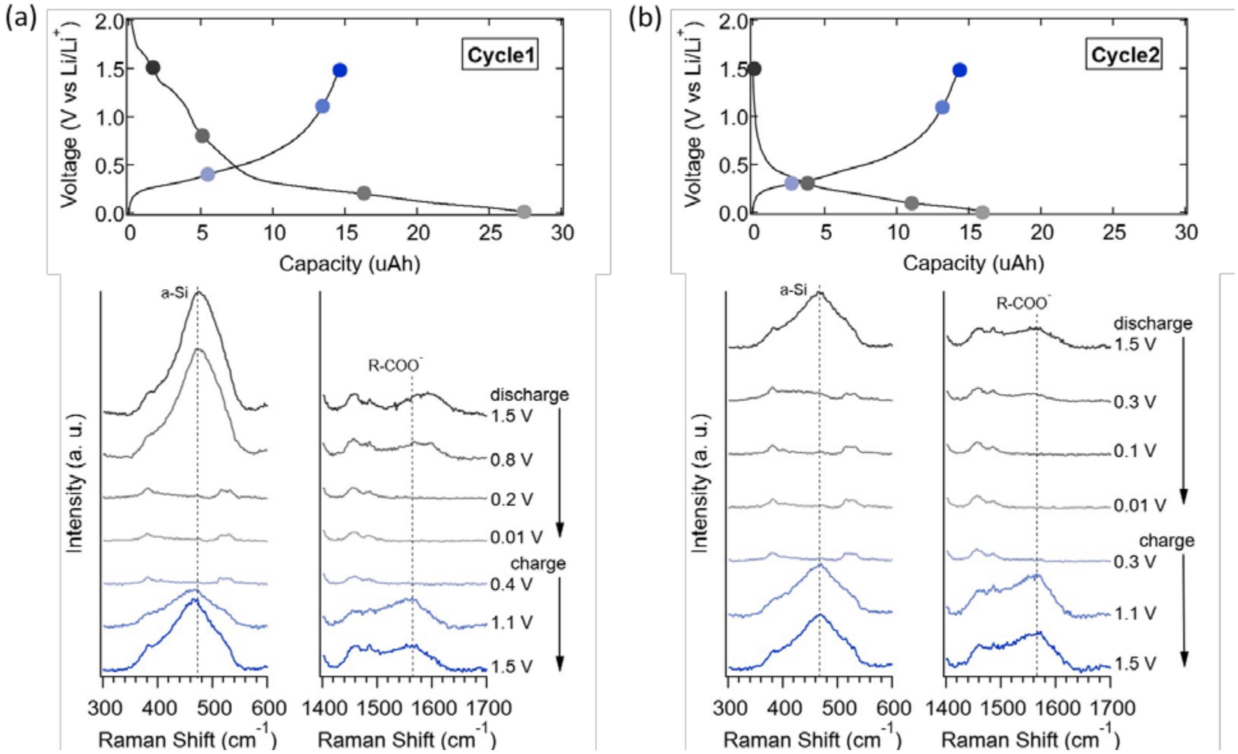

○ Figure 57. Galvanostatic cycling voltage profiles and corresponding *in situ* Raman spectra collected at specific voltages: (a) the 1st cycle and (b) the 2nd cycle. The spectra were obtained with a 632.8-nm He-Ne laser, and all spectra were baseline corrected.

The electrochemical behavior of the Si thin-film electrode agrees well with the reported literature [6], where the lithiation starts at around 0.3 V and continues until the assigned cutoff voltage (0.01 V). In addition, a significant amount of irreversible capacity loss is observed after the first delithiation, primarily due to the electrolyte reduction and subsequent SiEI formation. In the second cycle, the irreversible capacity loss is much less compared to that of the first cycle, likely due to the formation of SiEI in the first cycle, which prevents further electrolyte reduction.

In situ SERS spectra collected during the first and second cycles exhibit reversible peak intensity changes upon lithiation and delithiation. Specifically, the strong a-Si peak observed at 470 cm^{-1} prior to the lithiation disappears as the Si is lithiated (at 0.2 V) and reappears after the Si is delithiated (at 1.1 V). The same reversible behavior is observed in the second cycle. Another interesting feature is a new peak at 1,565 cm^{-1}, which evolves during the galvanostatic cycling. This 1,565 cm^{-1} peak first appears at around 0.8 V, which corresponds to the electrolyte reduction voltage [14,15], and the peak intensity change synchronizes with that of the a-Si peak upon cycling. This peak at 1,565 cm^{-1} is assigned to the asymmetric COO^- stretching mode [9]. Additionally, according to the previous *in situ* FT-IR study by Shi et al., this peak is likely from lithium propionate [8]. To find additional new peaks possibly attributed to decomposed species of reduced electrolytes and/or formed SiEI components, we tried additional cycling (up to 10 cycles) and lowering the applied current ($I = 7.5\ \mu A$) to increase the probability of electrolyte reduction and SiEI formation reactions. No additional new peaks, however, were observed during 10 cycles, and *in situ* SERS spectra with a lower current demonstrated almost the same spectral features as before. One possible explanation for limited peak detection is that it is challenging to collect Raman signal from decomposed species and/or formed SiEI components due to relatively too-strong Raman signal from both Si anode and electrolyte components. Furthermore, many of the SiEI species are soluble in the electrolyte, so they may go into solution and move away from our Raman measurement excitation volume [10,11].

We successfully developed a novel spectroscopic technique for *in situ* studies of the electrode-electrolyte interphase (EEI). *In situ* measurements show the reversible changes in the a-Si peak intensity upon lithiation and delithiation. Moreover, alkyl carboxylate species were detected as a significant SiEI component that possibly incorporated into the Si electrode surface during cycling. Our experimental setup showed a reproducible and reliable electrochemical and spectroscopic performance over multiple cycles. This method thus provides valuable information regarding the surface chemistry changes and evolution of the SiEI, which can be useful for detailed understanding (and stabilization) of the SiEI layer for the development of next-generation lithium-ion batteries. Finally, we emphasize that this technique is applicable to other battery systems and the EEI contained within.

In Situ Evaluation of the SEI in the Presence of a Binder

Binders, particularly polyvinylidene fluoride (PVDF), are an industry standard used in composite electrodes to bind active materials and additives such as C black to the metal current collector and to promote particle-to-particle cohesion. Though the final architecture of the binder matrix is not fully understood, there are interactions between the surface of the Si and the binder. This leads to the question of how the addition of an insulating polymeric binder, added to mitigate the effect of Si expansion in composite slurries, affects the SEI formation.

We know the binder has a role in the electrochemistry regardless of the anode [16,17]. For example, the commonly used binder PVDF doesn't work in silicon-based chemistries, but the use of polyacrylic acid (PAA) does [18,19,20]. PAA is composed of carboxyl groups that form a covalent bond to the hydroxyl groups present on the Si surface due to the native oxide layer [19]. Very little is known about how PAA or any other binder affects the composition and formation of the SEI. For instance, how does the insulating nature of the PAA change or alter Li conduction pathways? Or, if the Si nanoparticle is completely coated by PAA, how does the electrolyte interact with the active material? Lastly, does the SEI form on the surface of the polymer or the surface of the Si?

In addition to materials like PAA there has also been interest in electronically conductive binders in order to eliminate the need for conductive additives such as C black. One such example is Poly(2,7-9,9-dioctylfluorene-co-2,7-9,9-(di(oxy-2,5,8-trioxadecane))fluorene-co-2,7-fluorenone-co-2,5-1-methylbenzoate ester) (PEFM), which was designed to incorporate different functional groups to create an n-type conductive polymer modified to uptake electrolyte and maintain mechanical stability [21]. Similar questions exist as to how this material works and what functionality could be utilized to develop designer interfaces.

To answer these questions, we applied spin coating to prepare model electrodes with well-defined binder layers and probed their chemistry using neutron reflectometry. The absence of charge of a neutron gives rise to a deeply penetrating particle, allowing for their use as a probe to study materials in complex environments. Because of their wavelike nature they can be reflected and/or refracted off of surfaces, separating materials of different indices of refraction in a way analogous to electromagnetic radiation—that is, neutrons obey Snell's Law. This gives rise to a neutron-scattering technique sensitive to surfaces and interfaces known as neutron reflectometry (NR). Reflectometry is an elastic scattering technique, i.e., there is no energy exchange when neutrons or x-rays interact with matter. In the case of neutrons, unlike electromagnetic radiation, the indices of refraction of most materials is less than one. As a result of neutron interaction with the nucleus as opposed to the electrons, the technique is not limited by Z number. This is of particular importance in materials for energy storage due to the presence of Li and H. In addition, neutrons are sensitive to isotopes, which can be exploited to allow for contrast variation within a single experiment.

The specular reflection of neutrons off different layers of a material results in the wave vector transfer (Q) described by the following term:

$$Q = k_{f,z} - k_{i,z} = \frac{4\pi}{\lambda}\sin\vartheta$$

Equation 1. Wave vector transfer

where θ is the angle of incidence and λ the neutron wavelength. Probed length scales range from 1–500 nm with sub-nm resolution. Reflectivity (R) is a measure of the ratio of reflected neutrons to those that fall incident on the surface. Data collection results in a plot of R vs. Q. Through a fitting routine, the thickness, roughness, and/or diffuseness of the layers is determined. However, the most important parameter determined is the scattering length density (SLD), which gives information on the composition of the measured layer as defined by:

$$SLD = \beta = \frac{\rho N}{M}\sum_i b_i$$

Equation 2. Scattering length density

where ρ is the materials density, N is Avogadro's number, M is the molar mass, and b_i is the scattering length of each individual scatter within the molecular volume. Modeled data results in an SLD plot, a one-dimensional representation of the heterostructures of the system separated by the interfacial roughness between the layers. Figure 58 shows a schematic representation of the cell and electrode configuration used for these experiments, along with an image of the cell on the beam line.

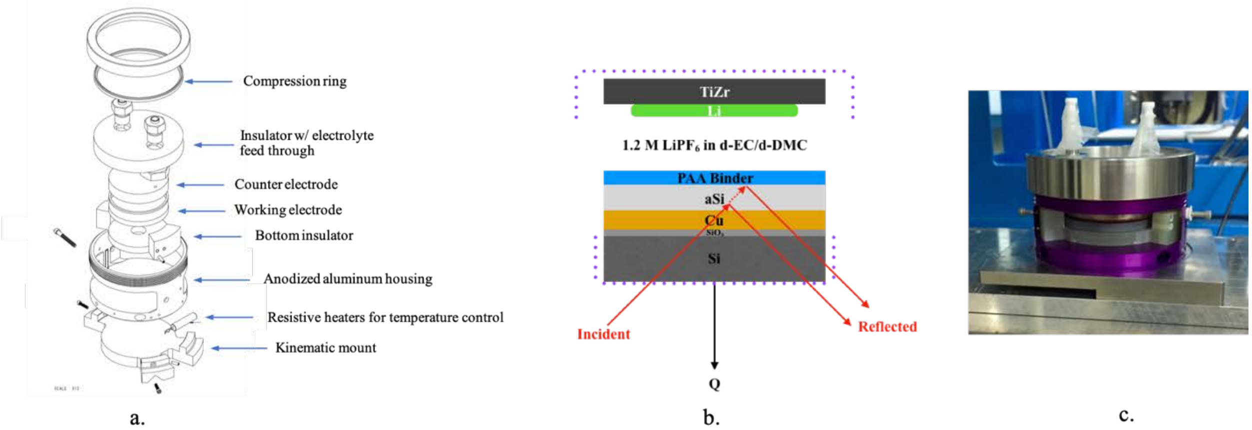

Figure 58. Schematic (a), scattering orientation (b), and photo (c) of the *in situ* electrochemical cell

Interfacial Chemistry of PAA Binders on Amorphous Silicon

The processing conditions for the PAA layer are crucial to the cyclability of the anode. The first attempts at electrode fabrication utilized a 5 wt% solution of M_w=450,000 PAA, spin cast, and dried at 200°C for various amounts of time. At 200°C the PAA crosslinks and forms an anhydride [22], resulting in the PAA layer being impermeable and preventing lithiation of the a-Si (Figure 59. ***This suggest that when casting anodes from composite slurries, the polymer binder does not fully coat Si nanoparticles' surfaces as this would prevent any cycling.*** In order to introduce the polymer to a thin-film architecture that allowed for cycling, we evaluated different processing conditions. After trying different molecular weights and drying temperatures it was determined a M_w=1,800 PAA dried at 140°C prevented crosslinking and enabled anode lithiation.

Figure 59 shows the reflectivity data collected for these samples as a function of the cell potential versus $Li^{0/+}$. Figure 60 shows the scattering length density profile measured from the fits of the reflectivity data. We constrained the parameter space for fitting the NR data by measuring the as-prepared heterostructures of the vapor-deposited layers in air. The Cu and a-Si layer thicknesses were determined to be 17.0 nm ± 0.01 nm and 58.80 nm ± 0.04 nm, with an SLD of 6.58 ± 0.01 and 1.76 ± 0.02, respectively (the SLD unit $\times 10^{-6}$ Å^{-2} will be kept off for simplicity). These values agree with uniform dense layers of Cu and H incorporating into the a-Si layer (presumably during the sputtering process). It is important to note that the SLD is a summation of each of the individual scatterers within a layer. As such, the incorporation of an element with a large scattering cross-section, such as C (6.6 fm), D (6.6 fm), P (5.13 fm), and/or F (5.7 fm) will increase the overall SLD as a result of these elements' large neutron cross-sections. Likewise, in the case of Li or H incorporation (-1.90 and -3.7 fm, respectively), a decrease in the SLD would be expected. In order to prevent water contamination, the PAA-coated sample was placed directly into the glovebox while still hot from drying. To determine the thickness and the SLD of the spin-cast PAA, witness samples were made using the same spin-coating and drying procedures directly onto the single-crystal Si substrate, which were promptly measured by NR. The PAA thickness averaged around 30 nm with an SLD of 1.8, which is slightly lower than the theoretical SLD of PAA of about 1.96, assuming a density of 1.41 $g\times cm^{-3}$. The SLD of the Si substrate was 2.07 and had a thin oxide layer with an SLD of 3.5, which provided contrast to the PAA layer.

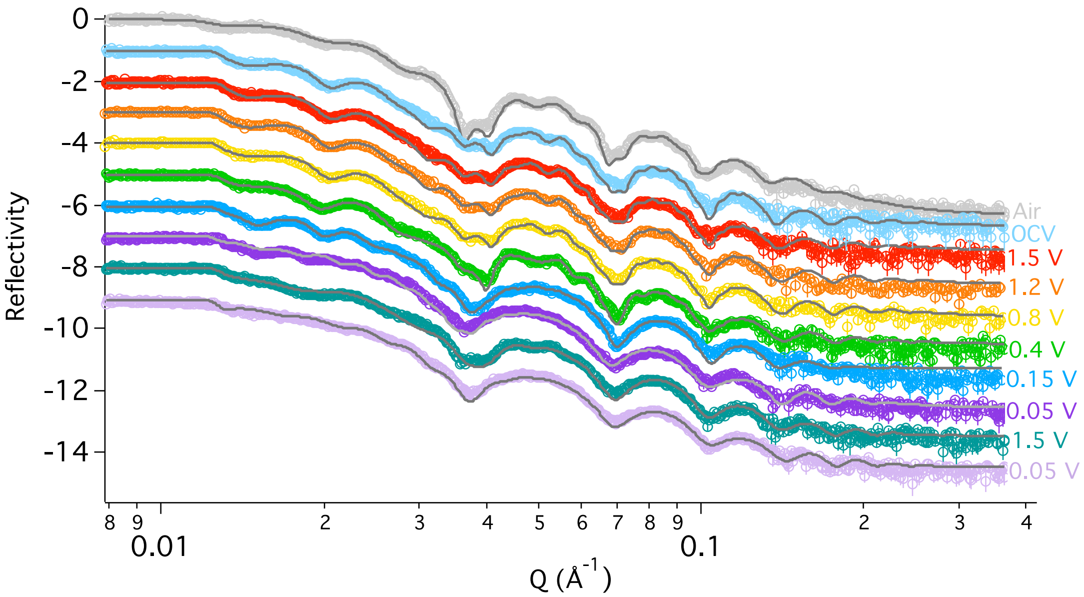

Figure 59. Neutron reflectivity curves (open circles) and fits (grey line) for PAA on a-Si thin film anode at different states of charge (curves offset for clarity)

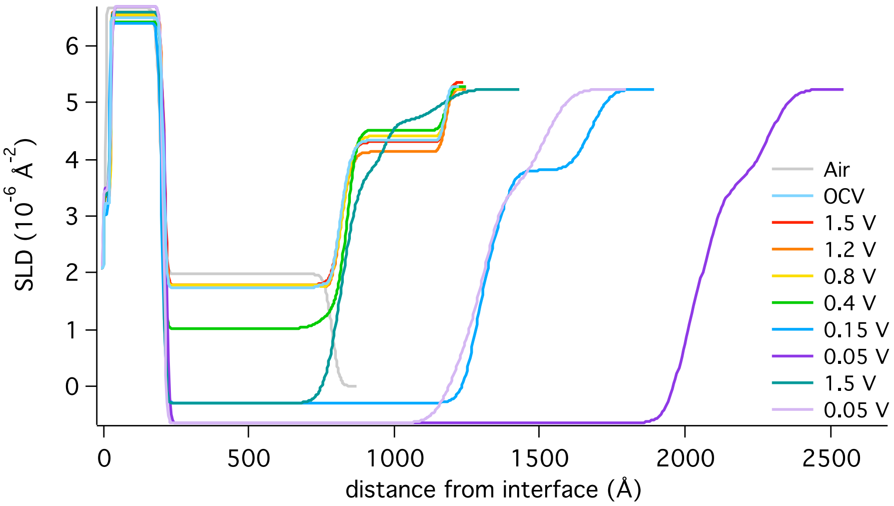

Figure 60. The resulting SLD plots from reflectivity fitting routine representing a one-dimensional view of the film heterostructures separated by interfacial roughness.

Upon cycling there are no significant changes within the system at 1.5 V, as expected. No change is evident in the PAA layer. The a-Si layer remains at 56.54 nm ± 0.15 nm with an SLD of 1.79 ± 0.03. At 1.2 V minimal changes were observed in the NR data, and all layers' thicknesses and SLDs remain unchanged statistically. Figure 61 highlights the stability within the three layers, in both the SLDs and thicknesses, up to 0.8 V. Typically, at potentials more negative than 1.2 V, electrolyte reduction and SEI formation occurs [23]. This was not seen in the NR at 0.8 V; in fact, the calculated scattering profile remains unchanged.

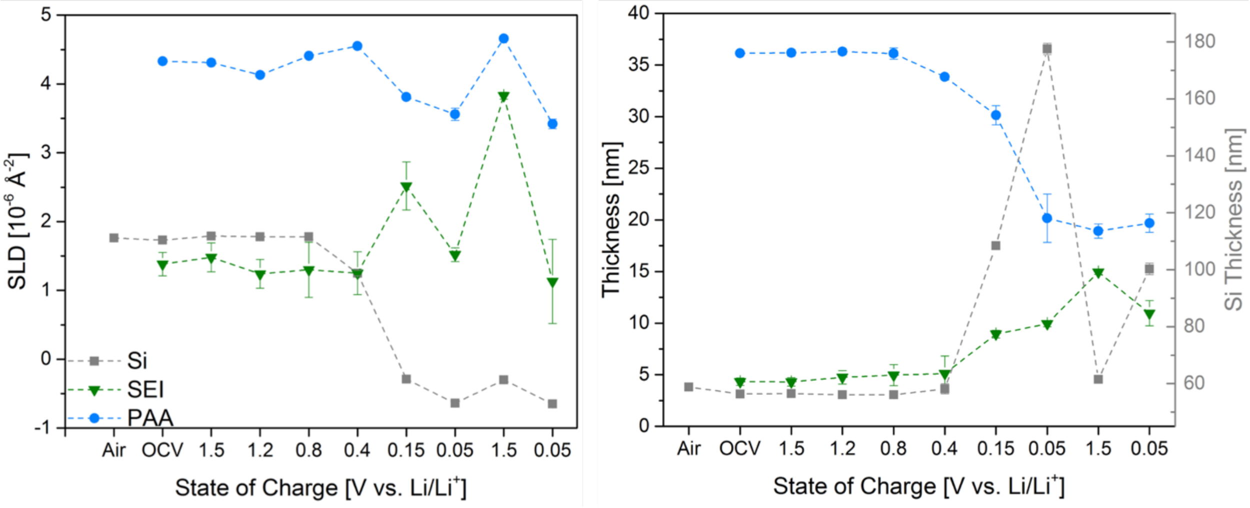

Figure 61. A summary of the SLD (left) and thickness (right) values obtained from NR refinements

At 0.4 V the PAA layer thins down to 33.9 nm while maintaining its SLD at 4.55 ± 0.02. There is a 2-nm increase in the a-Si layer (56 to 58.2 nm ± 1.8 nm) with a decrease in the SLD from 1.76 to 1.25 ± 0.04 (Figure 61), indicating the beginning of lithiation of the sample, as Li is a negative scatterer. However, NR implies little lithiation from thickness changes, but electrochemically the Li to Si ratio is estimated to be $Li_{0.2}Si$. At 0.15 V the NR profile drastically changes. Here, fringes between 0.04 Å^{-1} and 0.1 Å^{-1} are smoothed (Figure 59, dark blue), indicating changes in layer thicknesses and compositions. The a-Si layer swells to 108.4 nm ± 0.51 nm with an SLD of -0.29 ± 0.04, suggesting composition of $Li_{1.6}Si$ for the a-Si layer from the refined NR data. Assuming 100% Faradaic efficiency, the electrochemically derived composition is around $Li_{2.3}Si$. SEI is most likely being consumed to form the SEI layer. The oxide layer on the surface of the electrode increases in SLD from ~1.3 to 2.52 ± 0.35. The increase in the SLD suggests a heavier scatter such as C, D, O, F, or P incorporating into the oxide film, as opposed to Li. *These components are all from the electrolyte, suggesting electrolyte decomposition products in the oxide layer, resulting in the formation of the SEI.* The PAA layer at the electrolyte interface continued to thin, settling at 33 nm ± 0.1 nm from 36 nm, and decreasing in SLD from 4.3 to 3.81 ± 0.04. Due to the polarization of the cell at 0.15 V, a significant amount of Li is being diffused into the Si and the lowering of the PAA SLD is the result of Li incorporation into the PAA layer.

Upon further lithation the PAA layer has thinned by 10 nm at 0.05 V (30.1 nm to 20.2 nm), in addition to a change in the SLD to 3.56 ± 0.09 (from 3.8 at 0.15 V). The thinning of the PAA from the start of 0.4 to 0.05 nm would suggest the PAA is dissociating into the electrolyte and is changing in composition at the beginning of lithiation (x>1). This could be attributed to Li exchange within the PAAH to LiPAA. The SEI layer decreases in SLD to 1.52 ± 0.1 compared to 2.52 at 0.15 V, suggesting more Li in the film. The silicon is lithiated to $Li_{3.8}Si$, which results in a thickness of 177.54 nm ±2 nm and SLD of -0.64 ± 0.04. Upon delithiation to 1.5 V, the SEI layer grows to 15 nm ± 0.2 nm with an increase in the SLD to 3.8 3± 0.05 (from 1.52), reflecting a change in the chemistry of the layer as a result of the delithiation of the anode. The increase in the SLD and thickness would be from the incorporation of solvent molecules such as C, O, and D. The PAA layer increases in SLD to 4.66 ± 0.03. The Si layer thins but the SLD (-0.3) indicates the anode was not fully delithiated, and from the electrochemistry the Li:Si ratio is estimated to be $Li_{0.9}Si$. The second lithiation sees the PAA layer remain ~20 nm; however, the SLD returns to around 3.4 as in the first lithiation. The SEI layer shrinks to 11 nm with a decrease in the SLD to 1.13 (as opposed to 1.52 after the first lithiation). Both the SEI layer and PAA change in chemical composition and thickness based on the state of lithiation or delithiation.

The above data detail the thickness and composition of the SEI layer that forms beneath a perfect PAA binder coating. Initially, the PAA uptakes solvent within the layer, but there is no evidence of the chemical reaction between the Si and the electrolyte. This is in contrast to previous NR experiments which observed a lithium-rich layer segregating to the a-Si surface upon exposure to the electrolyte, indicating that the PAA is protecting the silicon surface at OCV [24,25,26,27,28]. Instead, under the PAA layer we observe the hydrogen-terminated oxide layer grown on the a-Si from the reaction with the atmosphere. This suggests the PAA preferentially adsorbs the solvent, excluding the salt, which will play a role in the initial SEI formation and Li transport during lithiation.

There are few changes to the thickness and composition of the interfacial layers down to 0.4 V vs. Li/Li^+. This indicates that the PAA is effectively acting as an SEI by suppressing electrolyte decomposition while still allowing solvent to approach the silicon surface. This is in contrast to measurements collected on an amorphous silicon electrode, which revealed the formation of a 25-nm thick inorganic-like SEI layer [25,27]. This data indicates a well-defined PAA layer prevents electrolyte decomposition above 0.4 V, which may be beneficial to other intermetallic anodes such as antimony. Below 0.4 V there are significant changes observed at the Si-PAA interface. At 0.15 V, lithium-containing species have diffused to the silicon surface where they react (beneath the PAA layer), resulting in an inorganic-like SEI layer, Li_2O and LiF, that is about 10 nm thick and the silicon electrode begins to lithiate. Simultaneously, the PAA is thinning/decomposing and uptaking lithium within the PAA layer, leading to a lithiated PAA-like composition. This inorganic SEI layer is similar to the surface measured without the PAA [25,27]. Indeed, the composition is similar based on scattering length density (2.5 vs. 2.9), but the PAA layer is much thinner: 9 nm vs. 19 nm, respectively [25,27]. This indicates the polymer is acting as an artificial SEI while still enabling the formation of a lithium-containing SEI [29]. These data are consistent with reports which claim that after PAA is electrochemically reduced to form LiPAA, a protective layer of binder reduction products prevents the reduction of the carbonate-based electrolyte and forms a relatively thin and more stable SEI [30]. Similar effects on graphite anodes that contain PAA have been observed, where the binder suppressed the first lithiation decomposition of the electrolyte as a result of the PAA binder coverage [31,32]. Upon further lithiation below 0.05 V vs. Li/Li^+, the SEI continues to change in composition as evident by the decrease in the SLD from 2.5 to 1.5. Interestingly, the thickness remains constant at 9 nm.

Interfacial Chemistry of PEFM Binders on Amorphous Silicon [28]

The a-Si anode used in the NR studies was initially measured in air to determine the as-prepared structure of the sample. The refinement of the data (Figure 62) results in an SLD plot (Figure 62) which represents the heterostructure of the thin-film layer versus the SLD and is separated by interfacial roughness between each layer as schematically shown on the SLD plot on the bottom of Figure 62. From the refinement, the Si layer was determined to have a thickness of ~463 Å with an SLD of 2.07, which is in good agreement with the theoretical SLD of Si (2.07), indicating a uniform and dense a-Si film. There was no evidence for an oxide layer on the a-Si surface as there has sometimes been reported, or if present, was contrast matched and wasn't evident by NR [25]. The Cu film was approximately 200 Å thick with an SLD of 6.54, which is in good agreement of the theoretical value of 6.59, while the native oxide layer present on the substrate was ~17 Å thick. The PEFM polymer binder was spin coated to a thickness of 43.5 Å, which was ideal in order to allow lithiation and prevent creation of an insulating layer. The fit resulted in an SLD of 1.57. The SLD value of the density and areal density for the PEFM binder layer were calculated to be 0.35 g cm^{-3} and 0.15 µg cm^{-2}, respectively.

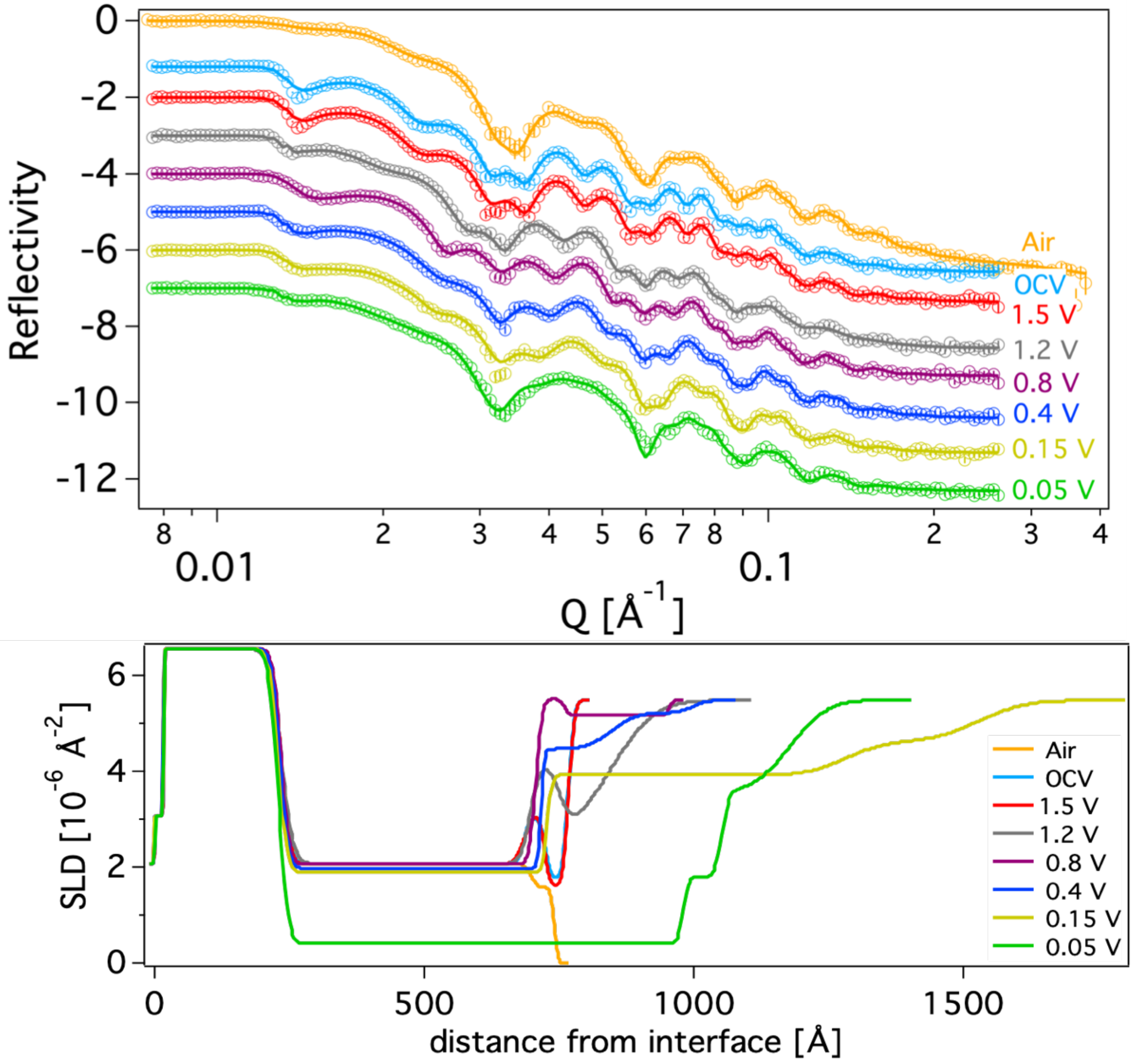

Figure 62. Neutron reflectivity data with open holes representing collected data and the fit, shown as a solid line (top). The SLD profile from resulting fit (bottom).

After the cell was constructed and alignment complete, the electrolyte was in contact with the anode for ~30 min and the OCV equilibrated to 2.8 V (vs. Li/Li$^+$) before data collection. Figure 62 shows NR data collected for the sample in the cell (top) and resulting SLD/thickness profiles (bottom). Changes in the reflectivity from air to OCV are evident, with the resulting fit indicating a decrease in the Si layer thickness (462 to 450 Å) and the addition of a new layer on the surface of the anode. The new film is attributed to a reaction layer that forms as a result of the chemical reactivity of the active Si surface with the electrolyte, and is approximately 41 Å thick. The SLD value was 3.01, significantly lower than the electrolyte SLD (5.46), indicating the incorporation of a component with a low coherent scattering length needed to lower the SLD. Given the elemental makeup of the electrolyte components, i.e., D, O, F, and P (6.6, 5.8, 5.1, and 5.6 fm, respectively), which have relatively high scattering lengths, the reaction layer is most likely Li rich, which has a bound coherent scattering length of -1.90 fm, coming from the $LiPF_6$ salt.

Refinements of the 0.8 V NR data indicate two distinct structures: the SEI layer on the surface of the anode and the PEFM on top of the SEI, depicted in Figure 62 (purple SLD profile). The interface between the SEI and PEFM are distinct and well defined, unlike what was observed at OCV, 1.5 V, and 1.2 V, which did not show distinct interfaces between the reaction layer on the surface of the anode and the polymer layer on top of the reaction layer. The most likely explanation is binding of Li to the PEFM, which is designed to be cathodically doped in a reducing environment where Li will attach to the F group of the polymer. In addition, at 0.8 V the reduction of the EC begins and the reaction layer becomes a true SEI layer. Interestingly, NR shows no increase in thickness for the SEI (from the previous potential), however there is a significant increase in the SLD from 4.09 at 1.2 V to 5.50, indicative of a significant change in chemistry of the SEI layer on the surface of the Si due to the reduction of the EC at this potential.

The lithiation of the a-Si layer begins at 0.4 V vs. Li/Li^+, as indicated in the NR refinements with the increase in the Si layer from 472.4 to 484.9 Å, coupled with the lowering of the SLD to 1.97, indicating the incorporation of Li as it has a low scattering cross-section which lowers the average SLD. From previous work the extent of lithiation was estimated to be $Li_{0.05}Si$, a very small Li content within the Si [13]. Other Li is becoming incorporated in the SEI layer on the silicon, as a significant decrease in the SLD, from 5.5 to 4.5, was observed as well as a swelling of the layer by over 70 Å (compared to the 0.8 V thickness). There is evidence of a more intermixed layer between the polymer and SEI forming, as indicated by the SLD profile (Figure 62) in which the distinct polymer layer seen at 0.8 V is no longer evident at 0.4 V. The SLD profile indicates a diffuse interface between the SEI and polymer layer. The large uptake of electrolyte results in a contrast match as the layers' SLDs become close to that of the electrolyte. By 0.15 V, the PEFM and SEI layers result in a gradient where the interface between the two layers is no longer distinguishable. Interestingly, the SLD of the PEFM layer has decreased from 5.21 to 4.61, similar to the SEI layer which sees the SEI settle to 3.91 (as compared to 4.46 at 0.4 V). As the potential is decreasing and more Li is moving through the system, it is most likely becoming incorporated in the PEFM as well as being consumed in the SEI, leading to the small Li:Si ratio, $Li_{0.09}Si$, being observed. The Si layer has only slightly changed in both thickness and SLD, further supporting small lithiation of the anode.

At 0.05 V the layer has been lithiated to $Li_{0.7}Si$. Due to low Li:Si ratio, the Li was most likely consumed in both the SEI and PEFM layers, which is further evidenced by a decrease in the SLD of the SEI (3.91 to 1.79) and the PEFM (4.61 to 3.55). The SEI and PEFM layers appear to swell significantly at 0.15 V; however, at 0.05 V a distinct 72.1 Å SEI layer forms on the surface of the lithiated Si with an SLD of 1.79 (Figure 62). This would indicate a fairly Li-rich SEI due to the significant decrease in SLD from the previous two voltage states. Lithiation is also indicated by an increase in the Si layer settling to 750.8 Å and lowering of the SLD to 0.40, indicative of Li incorporation.

In summary, a distinct reaction layer forms on the surface of the a-Si anode while the PEFM stays on top of the reaction layer, and even though there is not a sharp interface between the two layers they are distinguishable up until 0.8 V (Figure 62, bottom). The PEFM is a dynamic layer, changing in both SLD and thickness as the cell is polarized to lower potentials (vs. Li/Li^+). A large gradient between the SEI (after 0.8 V) and the PEFM occurs at 0.4 V and 0.15 V, whereas there is no true distinction between the polymer at the electrolyte interface and the SEI on the surface of the anode. Once the cell is polarized to 50 mV, there is enough of a driving force to push the trapped Li in the binder into the anode, resulting in a reordering of the SEI and PEFM. The PEFM shrinks by ~126 Å (247 Å at 0.15 V to 121 Å at 0.05 V), forming well-defined interfaces between the SEI and binder layer (Figure 62, bottom, green SLD plot). However, the PEFM is no longer the same chemistry as the as-prepared sample, as evidenced by changes in the SLD, most likely being a chemical makeup of decomposition products and reactants leading to an intermixed layer as summarized in Figure 63. The PEFM binder was designed to swell in electrolyte solutions, similar to PVDF, and shown to incorporate upwards of 50 wt% of solvent within its structure [6,14]. The PEFM layer does not inhibit the electrolyte from contacting the a-Si surface, as evidenced by the documented formation of a reaction layer, akin to a pre-SEI observed at OCV (Figure 62), and in the 12-Å decrease in the Si layer (from in air) when in contact with the electrolyte [9,11]. From OCV to 1.2 V there is distinct separation between the reaction layer on the surface of the Si and the PEFM on top of the reaction layer, as evidenced in the SLD plot in Figure 62. After polarization of the cell to 0.8 V vs. Li/Li^+, the significant change in SLD from 1.57 in air to 5.15 indicates a larger incorporation of the electrolyte into the layer.

From the NR it is evident that the polymer layer is continuously changing with higher states of lithiation through interactions with the electrolyte. The large amount of electrolyte uptake within the PEFM inhibits the bulk electrolyte from contacting the Si surface. The most likely explanation for the diffuse layers, i.e., a lack of distinct interfaces and more of a gradient from the electrolyte/PEFM/SEI interfaces observed at 0.4 V and 0.15 V, is the result of electrolyte decomposition within the polymer and SEI layer altering the electrolyte composition that is interacting with the Si. The 0.05 V (vs. Li/Li^+) SLD plot showed a distinct SEI with a low SLD (1.79) form on the surface of the Si, but is not purely LiF, which has a theoretical SLD of 2.30. This SEI layer is relatively thin at 72.1 Å. The polymer layer is most likely a composition of electrolyte decomposition products as the SLD settles to 3.55 and is no longer PEFM. The layer is 126.3 Å thick, compressing from 0.15 V (247.3 Å), which would indicate products moving out of the binder layer into the SEI or silicon.

Comparison of Binders and Binderless Electrodes [24,25,27,28]

Figure 63 graphically summarizes the structure of the SEI under the various binders, along with representative thickness and composition data measured at the same states of charge for cells with PAA and PEFM binders and cells without binders using only Gen2 electrolyte with and without FEC. Through an analysis of this data several trends can be ascertained:

1. The SEI formed on electrodes with a binder grows beneath the binder layer. Furthermore, if a binder is too “homogeneous,” then no lithium will transport through the binder coating. This is significant as it would indicate the binder needs to be heterogeneous on the silicon to enable lithiation. This points to the need to identify the “best” conditions with binder coverage to give optimal binding but still allow Li transport.

2. In all cases the SEI chemistry is dynamic. Previously we have described this effect as “breathing,” where part of the SEI is dissolved upon delithiation resulting in changes in the SEI chemistry due to loss of SEI components (e.g., LEDC). The extent of this breathing is likely correlated with capacity fade and loss of cyclability/increases in interfacial resistances. These data point to the need to design an electrolyte/SEI layer that forms insoluble species upon reduction or has strong bonding with the silicon surface to avoid dissolution.

3. The choice of solvent and binder has a dramatic influence on the SEI chemistry and composition. Figure 63, bottom, shows representative SLD and thickness data collected for the various samples evaluated using neutron reflectivity. Several trends are observed. First, at 0.4V, after lithiation has begun, the SEI using the PAA and FEC is thin (60–99 Å), whereas samples with PEFM or no FEC have a much thicker SEI (130–250 Å). These data indicate that the choice of chemistry results in less SEI and therefore less electrolyte consumption.

4. The data collected at 0.15 V, after the start of deep lithiation, show significant changes in the thickness and composition as a function of the electrolyte/binder. Specifically, the FEC SEI is dense and has a lower SLD (2.3), indicating that it is predominantly inorganic in nature (LiF-like). The PAA has a slightly higher SLD (2.5) and thickness (89 Å) than with the FEC. Without a binder or FEC, the SEI has a higher SLD (2.9) and larger thickness (187 Å), while the PEFM has an SLD of 3.9 with a thickness of 556 Å. Following this trend, the FEC and PAA give a thinner, more inorganic SEI, while the Gen2 and PEFM lead to a thicker, more organic SEI layer. This is significant as there is more loss in structural thickness and composition for the SEI grown as a more organic composition compared to the more inorganic composition. The significance of this is that the SEI needs to be more inorganic to be stable. This points to the need to prevent the dissolution of species like LEDC.

5. There are indications that the binders are playing a role in the selective transport of electrolyte species. When compared across one another it appears that the PAA is acting to concentrate the Li ions needed

to form a dense inorganic SEI, as evident by the lower SLD of the SEI layer. The PEFM appears to be acting to concentrate the solvent (as evident by its high SLD) at 0.4 V and 0.15 V. This will lead to a higher organic-content electrolyte that more readily dissolves, as evident in the loss of SEI thickness at maximum lithiation (0.05 V). The significance of these data is that it might be wise to investigate binders that act as Li^+ transport membranes.

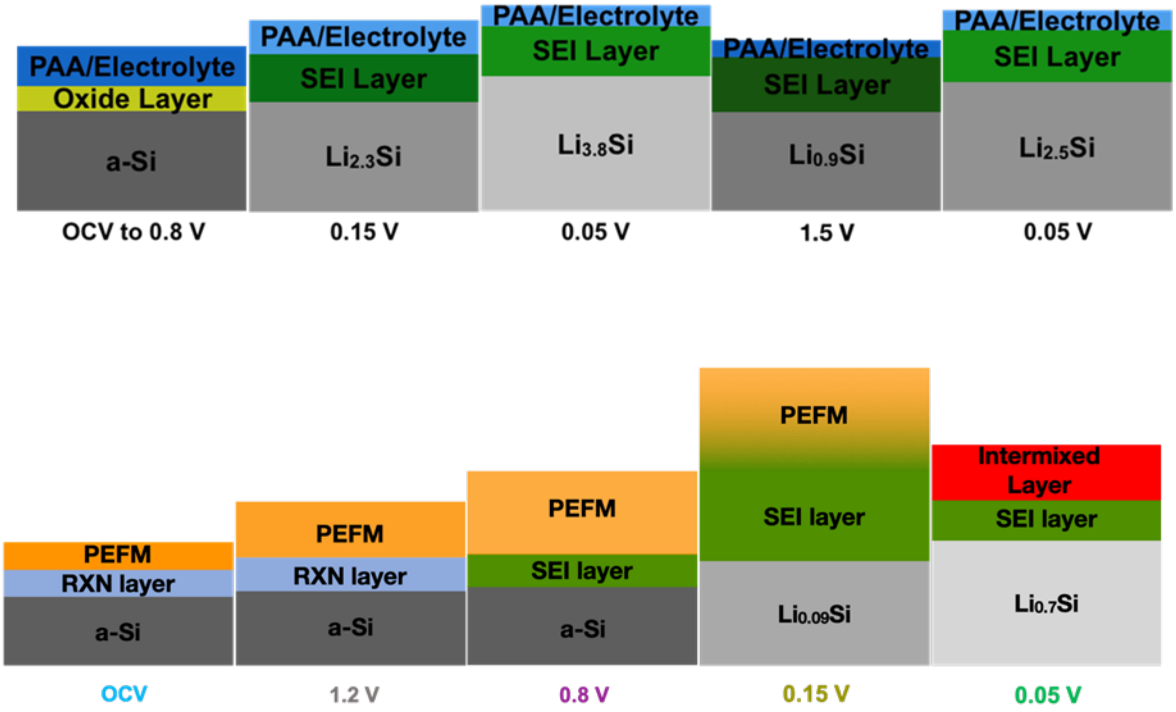

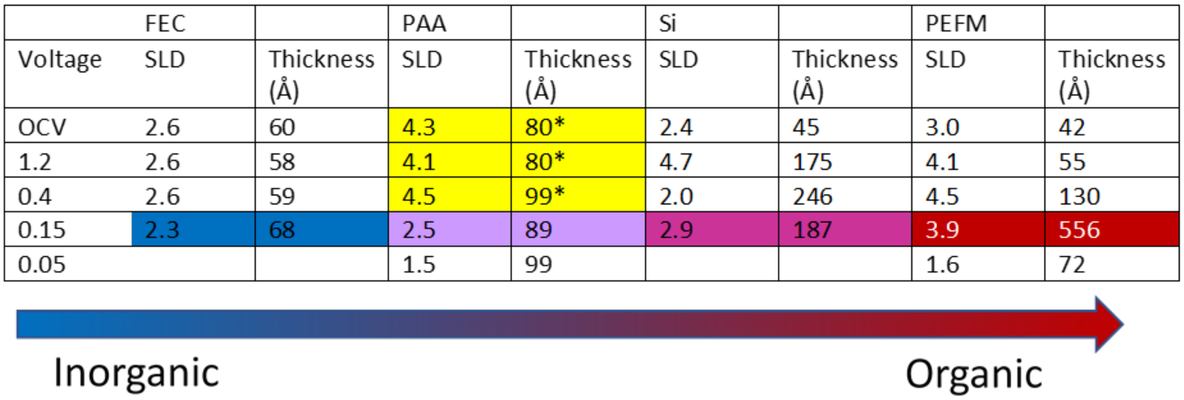

	FEC		PAA		Si		PEFM	
Voltage	SLD	Thickness (Å)	SLD	Thickness (Å)	SLD	Thickness (Å)	SLD	Thickness (Å)
OCV	2.6	60	4.3	80*	2.4	45	3.0	42
1.2	2.6	58	4.1	80*	4.7	175	4.1	55
0.4	2.6	59	4.5	99*	2.0	246	4.5	130
0.15	2.3	68	2.5	89	2.9	187	3.9	556
0.05			1.5	99			1.6	72

*= Estimated based on swelling of binder in solvent

Figure 63. Schematic of the SEI chemistry with various binders (top) and a schematic representation of the relative fraction of inorganic versus organic SEI components (bottom)

This work can be related to composite electrodes and the processing needed to make such electrodes. As is clear from this work, a fully coated Si particle behaves differently than one that has patchy coverage. If the binder fully encapsulates a Si particle and is cross-linked at high temperature from drying procedures, there will be no Li^+ transport. These data would support the need to make a heterogenous PAA/Si structure to allow some Li transport. The challenge would therefore be related to ensuring a minimally exposed silicon surface (which would react to form larger amounts of SEI) while maintaining some pathways for electrolyte to interact with the silicon surface. It would also explain why FEC works well with PAA-based composite electrolytes, in that it is resulting in the polymeric protective layer while maintaining Li-transport pathways.

Headspace Solid-Phase Microextraction GC-MS

Gas chromatography-mass spectrometry (GC-MS) is an analytical technique widely used to study degradation mechanisms in Li-ion batteries. This technique has been used by others in the past to study electrolyte degradation and elucidate probable decomposition mechanisms [1]. Here we attempt to use GC-MS to identify SiEI components that dissolve in the electrolyte during cycling. We present three case studies: (1) silicon anode coin-cell galvanostatic cycling vs. OCV rest, (2) the effect of 50 ppm of water added to Gen2 electrolyte, and (3) Gen2 electrolyte recovered from a Si-anode lithium half-cell that was held at elevated temperature. These studies provide guidance to stabilizing the SiEI, providing mechanistic explanations of surface chemistry and various reactions/interactions within the SiEI.

It is known that lithium salts, such as lithium hexafluorophosphate ($LiPF_6$), are destructive to the gas chromatography column; therefore, direct liquid injection of Gen2 electrolyte samples should be avoided. We are developing methods for extracting molecular species present in the electrolyte (e.g., electrolyte solvents, degradation species, soluble SiEI components, etc.) without the uptake of the potentially hazardous $LiPF_6$ salt. Recently, we have employed the technique of headspace solid-phase microextraction (HS-SPME), which has already been shown to work for electrolyte analysis of aged commercial Li-ion batteries [1]. In HS-SPME, volatiles present in the headspace of a vial are diffused from the sample to the headspace, where they are adsorbed onto a polymer-coated fiber with a high affinity for the target compounds. The fiber is then transferred to the injection port of the gas chromatography column, where the volatiles are desorbed for analysis (Figure 64). Preventing the gas chromatography column from exposure to corrosive $LiPF_6$ salt allows for a longer functional lifetime.

In our experiments, an 85-μm polyacrylate fiber (Supelco) was used for HS-SPME. Headspace extraction time was 10 min at room temperature. Sample analysis was performed by manual injection into an Agilent 7890B Gas Chromatograph coupled to an Agilent 5977B single quadrupole mass selective detector. We used a split ratio of 100:1 for Case Study 1, and a splitless column injection for the other two studies. Molecular species were determined by searching the mass spectra within a National Institute of Standards and Technology (NIST) database (MassHunter software).

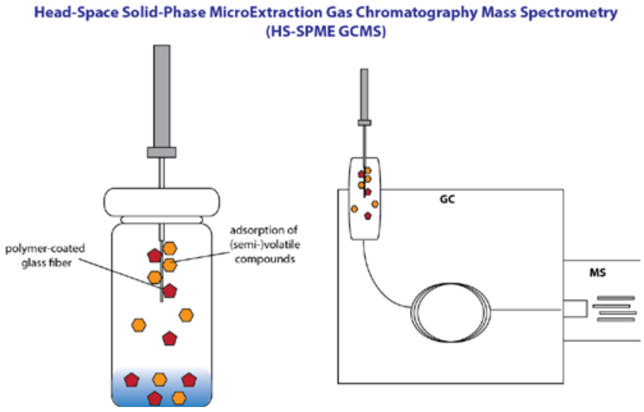

Figure 64. Headspace Solid-Phase Microextraction Gas Chromatography Mass Spectrometry (HS-SPME GC-MS)prevents injection of $LiPF_6$ salt into the gas chromatographer while still providing detection of electrolyte solvents, decomposition products, and soluble SiEI components

Case Study 1: Ten Galvanostatic Cycles vs. OCV Rest. For our initial SP-ME GC-MS study, we used approximately 6.5 × 6.5 mm^2 pieces of monocrystalline silicon wafer (675 μm thickness; boron-doped, 0.005 Ωcm) as the working electrodes. The counter electrodes were Li-metal foil. Celgard 2325 and Whatman GF/F glass microfiber were used for the separators. The Gen2 electrolyte consisted of 1.2 M LiPF$_6$ salt dissolved in a mixture of EC:EMC (3:7 wt%), and 30 μL was used. Half of the samples were left at OCV. After an initial 2-hr OCV rest, the others were galvanostatically cycled with an applied current of 30 μAcm^{-2} between voltage limits of 0.1 V and 1.5 V vs. Li/Li$^+$ and 2-hr half-cycle time limits. After 10 cycles all cells were carefully disassembled. The separators were placed in 10-mL glass vials and then caps with polytetrafluorethylene (PTFE) septa were crimped onto the vials to seal them for subsequent HS-SPME.

Figure 65 (b) shows the gas chromatographs of a cycled cell and one left at OCV. For comparison, we also used the same SPME method to sample the headspace above a vial containing 200 μL of just Gen2 electrolyte. All three samples yield similar results: a large EMC signal at a retention time around 4.1 min, a large EC signal around 12.3 min, and a smaller DEC signal around 6.4 min. The presence of DEC is not surprising as it is a known byproduct of EC reduction in the presence of EMC. The inset of Figure 65 (b) shows a zoom-in of the chromatographs between 10 and 14 min. There appear to be some small differences between samples, but the signal intensities are too low for us to confidently identify them at this time. It is likely that 10 cycles was insufficient to create enough soluble SiEI species for our detection. This led us to think about how we might increase the probability of chemical side-reactions in the cell, for example by adding a small amount of water to the Gen2.

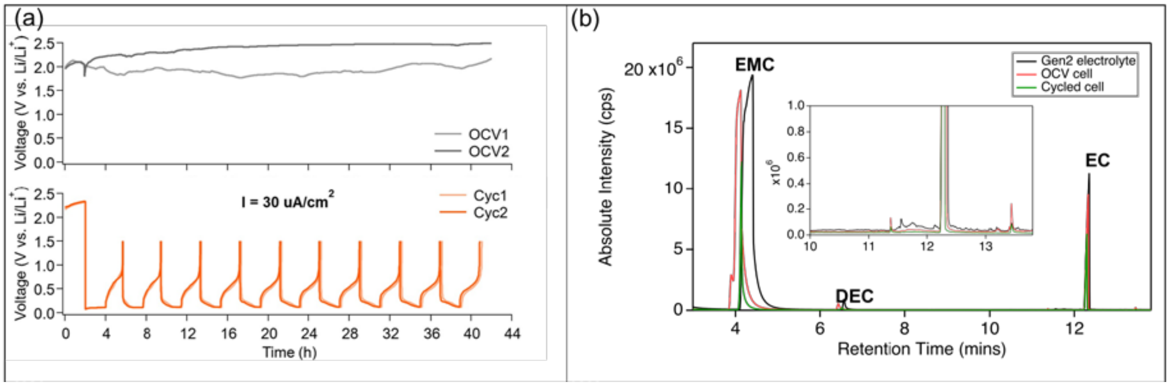

Figure 65. (a) Electrochemical performance of coin-type cells (with Si wafer vs. Li metal): Half of the samples were rested at OCV, while the other half were galvanostatically cycled between 0.1 and 1.5 V at an applied current of 30 μA/cm^2. (b) Gas chromatograms using HS-SPME to sample the headspace above the separators (red and green lines) and pristine Gen2 electrolyte for comparison (black line); inset in part (b) is a zoom-in at retention times between 10 and 14 minutes.

Case Study 2: Effect of 50 ppm Water Added to Gen2 Electrolyte. To understand how the presence of water in the system affects the interfacial chemistry of the Si anodes, we evaluated the electrochemical performance of Si anodes in Gen2 (1.2 M LiPF$_6$ in EC/EMC (3:7, wt/wt)) with 50 ppm of water. The Si-wafer electrodes were held at 3 different voltages: 1, 0.5, and 0.2 V vs. Li/Li$^+$ for 10 hours. Afterwards the cells were disassembled and the electrolyte was transferred into a 1-mL polypropylene vial with a PTFE-liner crimp cap.

Figure 66 shows the gas chromatographs of the electrolytes recovered from the potentiostatic experiment. For the sample with 50 ppm of H_2O in Gen2 held at 1 V there is a large signal corresponding to fluorophosphates. These species are known products of the hydrolysis of PF_5. A small but interesting signal present in every sample appears at 6.53 min retention time, corresponding to ethylene decarbonate (EDC). LiEDC has been detected by others as the primary electrochemical reduction product of ethylene carbonate (EC) during battery operation. Furthermore, we observed ethyl-hexyl carbonate at 11.6 min retention time. Alkyl carbonates can be formed by radical species originating from the reduction of EC that then react with other radical fragments.

Interestingly, in this case we see a greater signal intensity for 0.5-V samples, where side reactions with the electrolyte are favored. Almost no signal is detected from the 1-V sample without water.

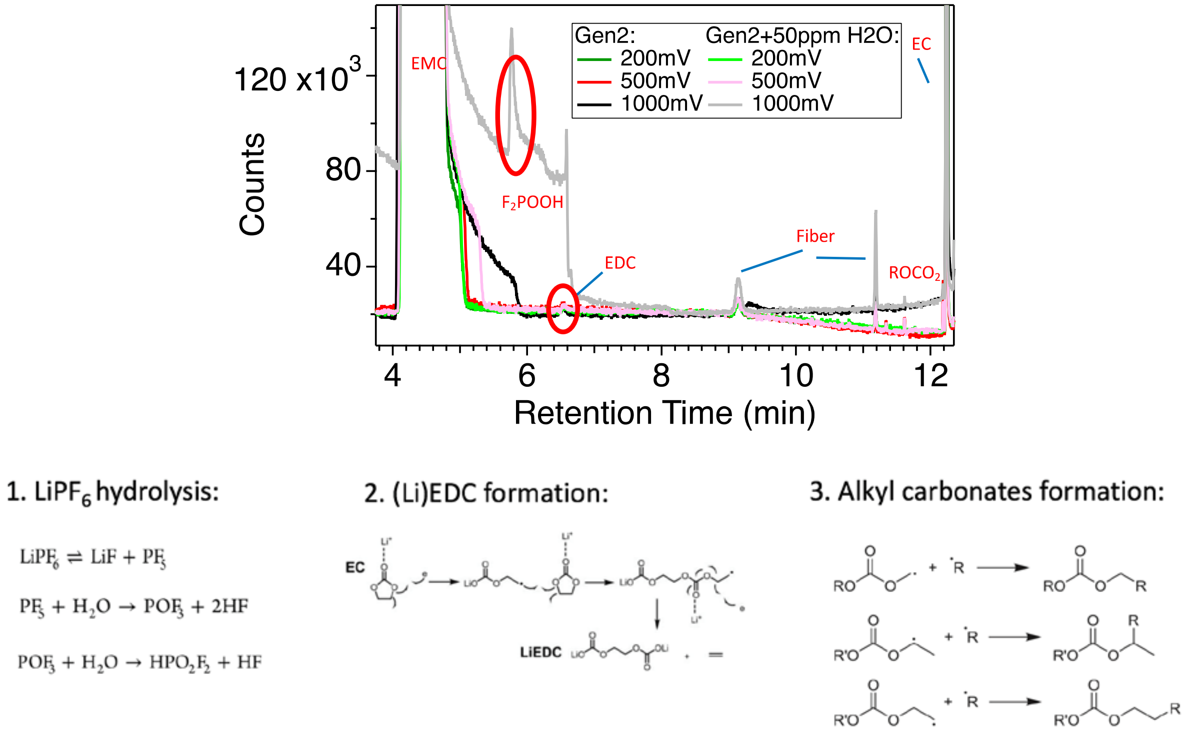

○ Figure 66. (top) Comparison of GC-MS gas chromatographs of the recovered electrolyte from potentiostatic holds at 1, 0.5, and 0.2 V for 10 hrs. (bottom) Reaction mechanism for some of the soluble SiEI species detected in the GC-MS.

Case Study 3: Temperature-Dependent Decomposition of Gen2. In our third study, we investigated the behavior of an a-Si anode in a lithium half-cell with Gen2 electrolyte at an elevated temperature of 60°C. The cell was held at OCV (~3.2 V vs. Li/Li$^+$, at 60°C) for approximately 30–60 min. Afterwards, the cell was disassembled and the Gen2-soaked separator was sampled with HS-SPME and run through the GC-MS. Figure 67 shows a comparison of the gas chromatographs of pristine Gen2 and the electrolyte species sampled by the HS-SPME. Gen2 electrolyte components are abundant in both cases: EMC (4.1 min) and EC (12.2 min). However, the heated electrolyte has many more peaks. Many of these peaks correspond to reactions between fluorophosphic acid (from PF_5 hydrolysis) and silicon oxygen species, for example methanephosphonofluoridic acid. Further studies of silicon anodes in $LiPF_6$-based electrolytes at elevated temperatures are ongoing.

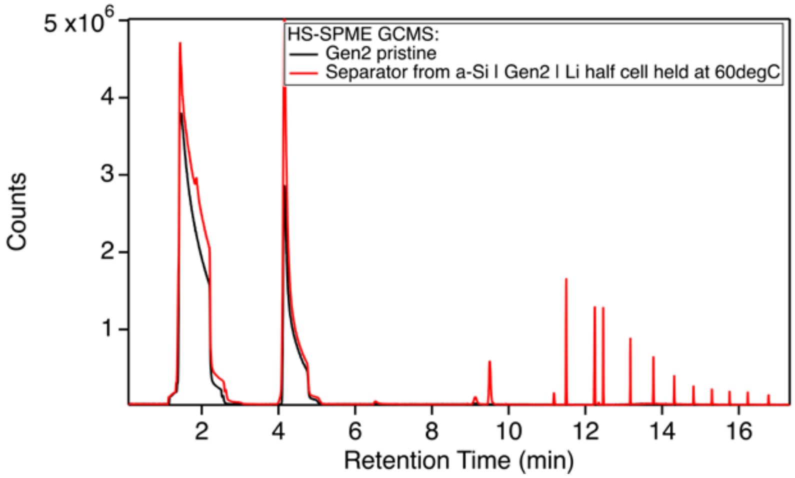

○ *Figure 67*. Comparison of GC-MS gas chromatographs of pristine Gen2 electrolyte and the electrolyte from a half-cell containing silicon, lithium, and Gen2 held at 60°C

In conclusion, the idea to detect soluble SiEI components with GC-MS remains promising. We show here that it is possible to analyze the volatile molecular components present in the electrolyte after battery cycling. Moving forward, we must continue to refine conditions for both the volatiles extraction (SPME time and temperature) and the GC detection (split ratio and heating). We seek to minimize the overwhelming EMC and EC solvent signals, but still detect soluble SEI species. In addition, we plan to combine our liquid analysis with gas GC-MS, as well as with analytical spectroscopy such as FTIR, to piece together a fuller picture of the SiEI formation and evolution during battery cycling. This technique will help evaluate some of the strategies emerging from other efforts in the project towards SiEI stabilization, such as silicon surface chemical modification.

Design of New Si Surfaces Based on Experimentally Validated Stable Chemical Moieties

Understanding the Role of Hydrophobic and Hydrophilic Surface Ligands on Si Nanoparticles

The SEI is important for reversible lithiation and charge storage in silicon anodes and may lead to better cycle performance. The ability of Li^+ ions to reach the Si NP surface, the electrical contact between the conductive carbon matrix and the Si surface, and the kinetics of alloying (hysteresis of alloy/dealloy) are all critical parameters which are controlled by the SEI. Therefore, it is important to systematically deconstruct the individual components of the SEI to judge their relative impact on the overall device performance. Generally, components of the SEI can be broken into two categories: inorganics (SiO_x, Li_xCO_3, and Li_xSiO_y) and organics ($C_xH_yO_z$). In Part 1 of this report we describe our efforts to quantify the effects of inorganic layers on the Si NP surface. Here, we probe the effect of the organic surface layer hydrophobicity on the electrochemical cycling of Si NPs. To do this, we leverage our nonthermal plasma synthesis method that produces exclusively SiH_x-terminated Si NCs and covalently bind hydrophobic dodecyl ligands to the Si surface. We measure the effect of this surface functionalization against nonfunctionalized (as-prepared SiH_x-terminated NPs) in composite half-cell anode configuration.

The electrochemical cycling data for the first 16 cycles, as well as the dQdV plot for dodecyl-functionalized and unfunctionalized silicon, are shown in Figure 68. From the cycling data for the unfunctionalized silicon (blue dots) shown in Figure 68 (a), these anodes display typical cycling behavior observed for these SiH_x-terminated NPs: low reversible first-cycle capacity (~50% coulombic efficiency) followed by delithiation capacities around 2,000 mAhr/g_{Si}. The dQdV plot for dodecyl-functionalized silicon NPs, however, displays significant differences. There is no measurable delithiation capacity at any point in the first 16 cycles. The minimal measured capacity shown in the black trace of Figure 68 (a) is due to the conductive carbon (Timcal

C65) lithiation/delithiation. We therefore can conclude that the organic component of the SEI can effectively eliminate the ability of silicon to store energy under standard cycling conditions.

Deactivation of these silicon NPs for lithiation is due to at least one of several possibilities: (1) the Si NPs are electrically insulated whereas the C65 does not form electrical contact with Si; (2) the Si NPs are ionically insulated against lithiation; (3) the composite electrode hydrophobicity inhibits GenF electrolyte from percolating through the composite network; or (4) the slurry properties of the dodecyl-functionalized Si NPs are poor and result in agglomeration and isolation of the Si. To test these hypotheses, we derived dQdV plots for the first cycles of electrochemical cycling. The SiH$_x$-terminated silicon, represented by the blue trace, displays the typical features for first-cycle lithiation. At ~1.2 V vs. Li/Li$^+$, a sharp feature corresponding to SiH$_x$ reduction is present which is followed closely by SEI formation (electrolyte reduction) at ~1 V. Crystalline Si lithiation is apparent by the steep feature at ~0.2 V. Upon delithiation, the Si undergoes amorphization, indicated by the two features at 0.3 V and 0.5 V. The dodecyl-functionalized Si NPs display some of the same character, but important differences exist. The feature-attributed SiH$_x$ reduction (residual SiH$_x$ surface species are always present after surface functionalization, as characterized by FTIR [33] and solid-state NMR spectroscopy [34]) and electrolyte reduction are both present, which indicate that the dodecyl-functionalized silicon is electrically contacted to the conductive carbon matrix, but the lithiation and delithiation features are both absent from the trace. These data indicate that the engineered hydrophobicity allows electrical contact but inhibits ionic conductivity. This important result provides critical information about the thickness (~1 nm) of hydrophobic coatings that will shut down (sterically block) Li$^+$ ion transport to the Si surface.

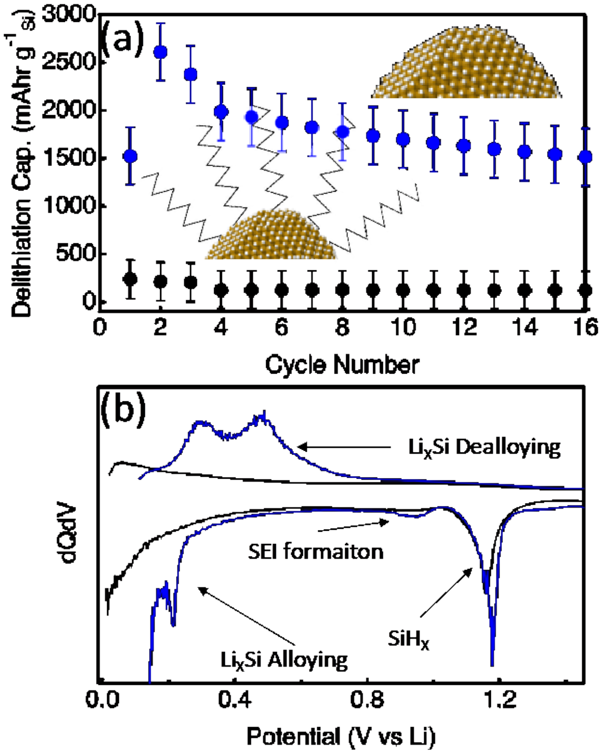

Figure 68. (a) Cycle data for *d* = 30 nm SiH$_x$-terminated (black) and dodecyl-terminated (blue) in a half-cell configuration. The first three cycles are at a C-rate of C/20, and the latter 13 are C/5. The error bars represent ± 1 σ from the mean of three electrodes. (b) Plots the dQdV of the first cycle for the same *d* = 30 nm SiH$_x$-terminated (black) and dodecyl-terminated (blue) samples.

We conclude that too-thick hydrophobic organic components can effectively turn off reversible lithiation of Si. From the dQdV plots, these organic moieties of the SEI affect the ionic conductivity much more than the electrical conductivity, as evidenced by the SiH$_x$ reduction without the corresponding Li$^+$ alloying. These initial Q4FY19 results will be followed up with a more comprehensive investigation which probes the magnitude of the ionic insulation by varying: (1) the length of the hydrophobic chain and (2) the identity of the surface functionalization (polyethylene oxide in place of the dodecyl, etc.).

Synthesis of Functionalized Si Through Milling

It is clear that the surface functionalization of silicon will be important to forming stable electrodes as well as interface chemistry. In the above section we discussed using Plasma-enhanced chemical vapor deposition (PECVD) -grown silicon particles and reacting them in solvent to form a silicon surface. In this section we are focused on crushing boules of silicon in the presence of a sacrificial solvent. This solvent will bind to the newly exposed Si surface sites.

Figure 69 shows representative SEM data collected for samples milled in various solvents. These materials have the same particle sizes and morphologies as the commercial silicon sources used in the Deep Dive program. More importantly, they behave fundamentally differently from the silicon materials used in the Deep Dive with respect to their surface chemistry. This is reflected in Figure 70, which shows the zeta potential data measured for the Deep Dive silicon materials and the zeta potential for the milled silicon synthesized by the team. The Deep Dive silicon all have low zeta potential values (<20 mV), which indicates that they do not form stable suspensions. In contrast, the milled silicon materials in solvents have high zeta potentials (>30 mV), pointing to the ability to form stable suspensions in solution during electrode processing.

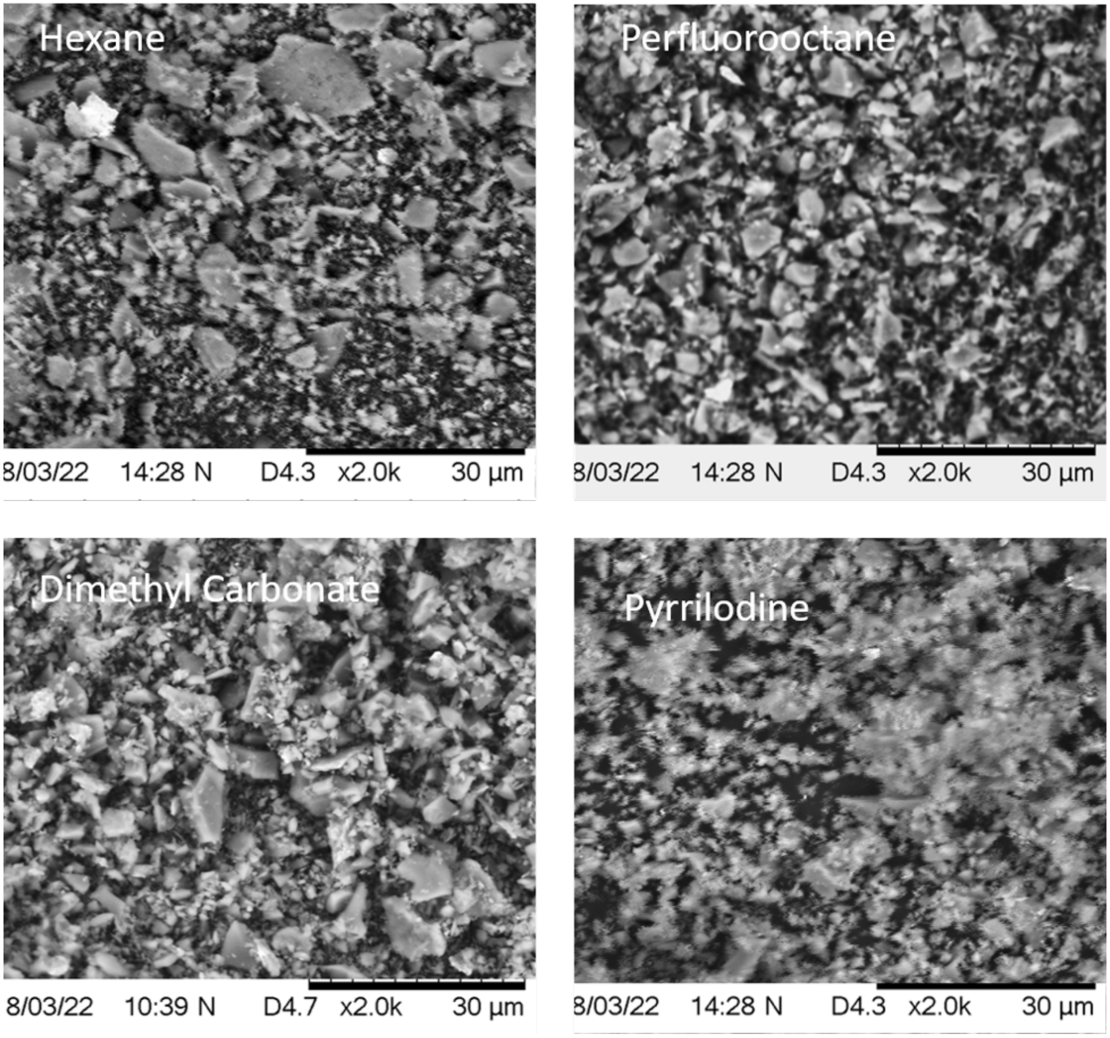

Figure 69. SEM images of milled silicon powders

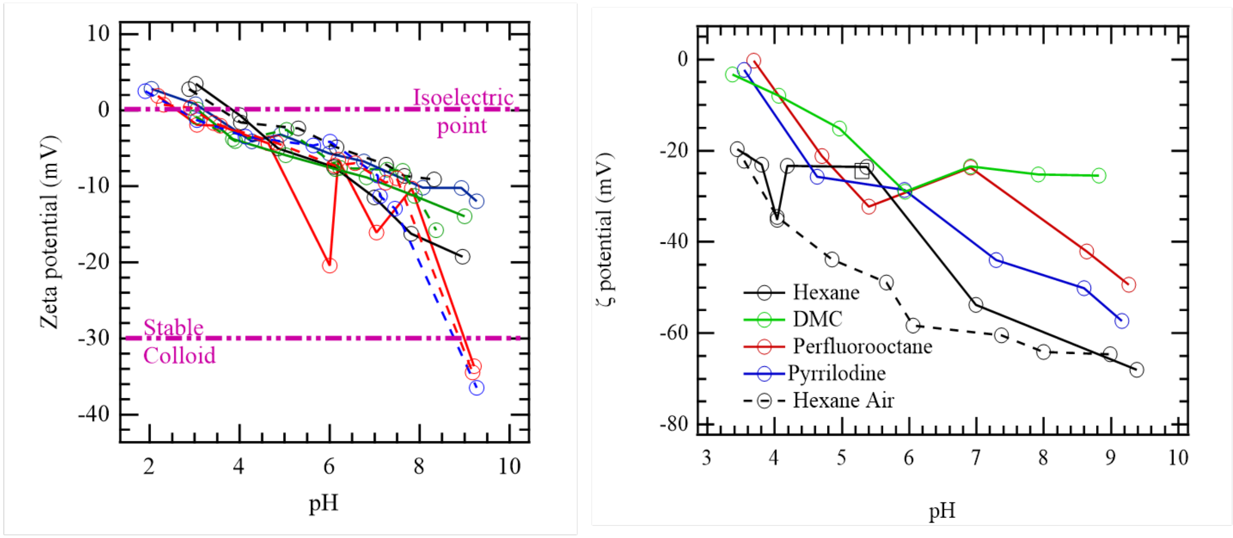

Figure 70. Zeta potential of Deep Dive silicon (left) and milled silicon powders (right)

The resulting materials were incorporated within a cell using 80% Si, 10% carbon black (CB), and 10% binder (PAA). The cycling results are shown in Figure 71. These data show variation in capacity retention but clearly significant changes due to changes in the surface chemistry. These changes will be explored in the future. Furthermore, the materials will be investigated using the tools and techniques discussed above.

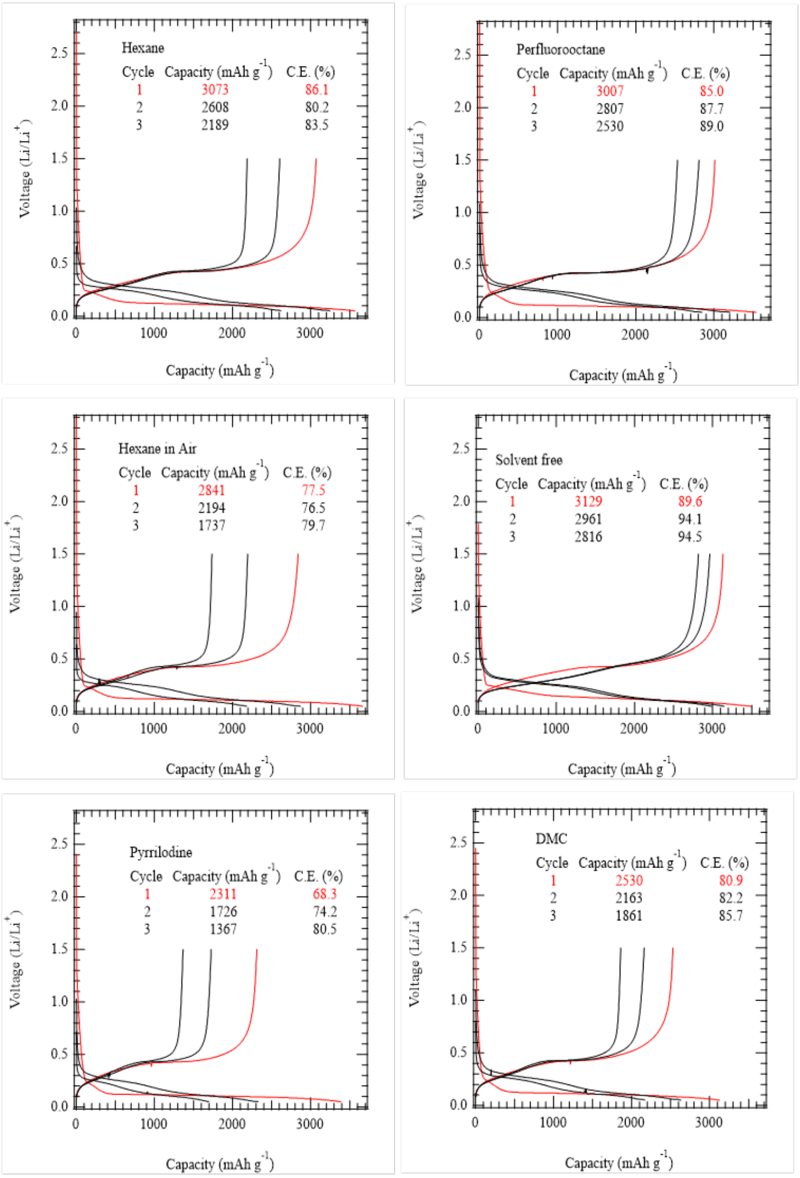

Figure 71. Representative cycling data measured for milled silicon electrodes

Conclusions

The above data demonstrate a dynamic SEI that differs depending on the electrolyte composition, surface chemistry of the electrodes, and electrolyte additives. The data show a set of complex correlations that are beginning to be unraveled using model electrodes, theory and simulation, and state-of-the-art characterization studies. The data point to the need to design new Si interfaces with electrolytes that will lead to more stable SEI layers. These are topics that are currently being pursued with new electrode chemistries that will provide avenues of research to stable Si electrodes and enable high energy-density electrodes (>350 Wh/kg).

References

[1] J. Nanda, G. Yang, T. Hou, D.N. Voylov, X. Li, R.E. Ruther, M. Naguib, K. Persson, G.M. Veith, A.P. Sokolov, Unraveling the Nanoscale Heterogeneity of Solid-Electrolyte Interphase Using Tip-Enhanced Raman Spectroscopy. Joule 3, 2001–2019 (2019).

[2] T. Hou, G. Yang, N.N. Rajput, J. Self, S.W. Park, J. Nanda, K.A. Persson, The Influence of FEC on the Solvation Structure and Reduction Reaction of $LiPF_6$/EC Electrolytes and its Implication for Solid Electrolyte Interphase Formation. Nano Energy 64, 103881 (2019).

[3] G.V. Zhuang, H. Yang, P.N. Ross, K. Xu, T.R. Jow, Lithium Methyl Carbonate as a Reaction Product of Metallic Lithium and Dimethyl Carbonate. Electrochemical and Solid-State Letters 9, A64–A68 (2006).

[4] H. Liu, X. Wang, H. Zhou, H.D. Lim, X. Xing, Q. Yan, Y.S. Meng, P. Liu, Structure and Solution Dynamics of Lithium Methyl Carbonate as a Protective Layer For Lithium Metal. ACS Applied Energy Materials 1, 1864–1869 (2018).

[5] G.V. Zhuang, K. Xu, H. Yang, T.R. Jow, P.N. Ross, Lithium Ethylene Dicarbonate Identified as the Primary Product of Chemical and Electrochemical Reduction of EC in 1.2 M $LiPF_6$/EC:EMC Electrolyte. Journal of Physical Chemistry B 109, 17567–17573 (2005).

[6] L. Wang, A. Menakath, F. Han, Y. Wang, P.Y. Zavalij, K.J. Gaskell, O. Borodin, D. Iuga, S.P. Brown, C. Wang, K. Xu, B.W. Eichhorn, Identifying the Components of the Solid–Electrolyte Interphase in Li-Ion Batteries. Nature Chemistry 11, 789–796 (2019).

[7] F. Shi, P.N. Ross, H. Zhao, G. Liu, G.A. Somorjai, K. Komvopoulos, A Catalytic Path for Electrolyte Reduction in Lithium-Ion Cells Revealed by In Situ Attenuated Total Reflection-Fourier Transform Infrared Spectroscopy. J. Am. Chem. Soc. 137, 3181–3184 (2015).

[8] F. Shi, P.N. Ross, G.A. Somorjai, K. Komvopoulos, The Chemistry of Electrolyte Reduction on Silicon Electrodes Revealed by In Situ ATR-FTIR Spectroscopy. Journal of Physical Chemistry C 121, 14476–14483 (2017).

[9] R. Baddour-Hadjean, J.P. Pereira-Ramos, Raman Microspectrometry Applied to the Study of Electrode Materials for Lithium Batteries. Chemical Reviews 110, 1278–1319 (2010).

[10] D. Liu, Z. Shadike, R. Lin, K. Qian, H. Li, K. Li, S. Wang, Q. Yu, M. Liu, S. Ganapathy, X. Qin, Q.H. Yang, M. Wagemaker, F. Kang, X.Q. Yang, B. Li, Review of Recent Development of In Situ/Operando Characterization Techniques for Lithium Battery Research. Adv. Mater. 31 (2019).

[11] G. Yang, I.N. Ivanov, R.E. Ruther, R.L. Sacci, V. Subjakova, D.T. Hallinan, J. Nanda, Electrolyte Solvation Structure at Solid-Liquid Interface Probed by Nanogap Surface-Enhanced Raman Spectroscopy. ACS Nano 12, 10159–10170 (2018).

[12] J.L. Allen, O. Borodin, D.M. Seo, W.A. Henderson, Combined Quantum Chemical/Raman Spectroscopic Analyses of Li^+ Cation Solvation: Cyclic Carbonate Solvents-Ethylene Carbonate and Propylene Carbonate. J. Power Sources 267, 821–830 (2014).

[13] S.D. Han, S.H. Yun, O. Borodin, D.M. Seo, R.D. Sommer, V.G. Young, W.A. Henderson, Solvate Structures and Computational/Spectroscopic Characterization of $LiPF_6$ Electrolytes. J. Phys. Chem. C 119, 8492–8500 (2015).

[14] V. Etacheri, R. Marom, R. Elazari, G. Salitra, D. Aurbach, Challenges in the Development of Advanced Li-Ion Batteries: A Review. Energy Environ. Sci. 4, 3243–3262 (2011).

[15] A. Wang, S. Kadam, H. Li, S. Shi, Y. Qi, Review on Modeling of the Anode Solid Electrolyte Interphase (SEI) for Lithium-Ion Batteries. npj Comput. Mater 4, 1–26 (2018).

[16] C. Erk, T. Brezesinski, H. Sommer, R. Schneider, J. Janek, Toward Silicon Anodes for Next-Generation Lithium-Ion Batteries: A Comparative Performance Study of Various Polymer Binders and Silicon Nanopowders. ACS Applied Materials & Interfaces 5, 7299–7307 (2013).

[17] S.J. Rezvani, M. Pasqualini, A. Witkowska, R. Gunnella, A. Birrozzi, M. Minicucci, H. Rajantie, M. Copley, F. Nobili, A. Di Cicco, Binder-Induced Surface Structure Evolution Effects on Li-Ion Battery Performance. Applied Surface Science 435, 1029–1036 (2018).

[18] J. Li, R.B. Lewis, J.R. Dahn, Sodium Carboxymethyl Cellulose: A Potential Binder for Si Negative Electrodes for Li-Ion Batteries. Electrochemical and Solid-State Letters 10, A17–A20 (2007).

[19] A. Magasinski, B. Zdyrko, I. Kovalenko, B. Hertzberg, R. Burtovyy, C.F. Huebner, T.F. Fuller, I. Luzinov, G. Yushin, Toward Efficient Binders for Li-Ion Battery Si-Based Anodes: Polyacrylic Acid. ACS Applied Materials & Interfaces 2, 3004–3010 (2010).

[20] B.T. Young, C.C. Nguyen, A. Lobach, D.R. Heskett, J.C. Woicik, B.L. Lucht, Role of Binders in Solid-Electrolyte Interphase Formation in Lithium-Ion Batteries Studied with Hard X-Ray Photoelectron Spectroscopy. J. Mater. Res. 34, 97–106 (2018).

[21] M. Wu, X. Xiao, N. Vukmirovic, S. Xun, P.K. Das, X. Song, P. Olalde-Velasco, D. Wang, A.Z. Weber, L.W. Wang, V.S. Battaglia, W. Yang, G. Liu, Toward an Ideal Polymer Binder Design for High-Capacity Battery Anodes. J. Am. Chem. Soc. 135, 12048–12056 (2013).

[22] J.J. Maurer, D.J. Eustace, C.T. Ratcliffe, Thermal Characterization of Poly(Acrylic Acid). Macromolecules 20, 196–202 (1987).

[23] K. Edström, M. Herstedt, D.P. Abraham, A New Look at the Solid-Electrolyte Interphase on Graphite Anodes in Li-Ion Batteries. Journal of Power Sources 153, 380–384 (2006).

[24] G.M. Veith, L. Baggetto, R.L. Sacci, R.R. Unocic, W.E. Tenhaeff, J.F. Browning, Direct Measurement of the Chemical Reactivity of Silicon Electrodes with $LiPF_6$-Based Battery Electrolytes. Chem. Comm. 50, 3081–3084 (2014).

[25] G.M. Veith, M. Doucet, J.K. Baldwin, R.L. Sacci, T.M. Fears, Y. Wang, J.F. Browning, Direct Determination of Solid-Electrolyte Interphase Thickness and Composition as a Function of State of Charge on a Silicon Anode. J. Phys. Chem. C 119, 20339–20349 (2015).

[26] T.M. Fears, M. Doucet, J.F. Browning, J.K.S. Baldwin, J.G. Winiarz, H. Kaiser, H. Taub, R.L. Sacci, G.M. Veith, Evaluating the Solid-Electrolyte Interphase Formed on Silicon Electrodes: A Comparison of Ex Situ X-Ray Photoelectron Spectroscopy and In Situ Neutron Reflectometry. Phys. Chem. Chem. Phys. 18, 13927–13940 (2016).

[27] G.M. Veith, M. Doucet, R.L. Sacci, B. Vacaliuc, J.K. Baldwin, J.F. Browning, Determination of the Solid-Electrolyte Interphase Structure Grown on a Silicon Electrode Using a Fluoroethylene Carbonate Additive. Scientific Reports 7, 6326 (2017).

[28] K.L. Browning, J.F. Browning, M. Doucet, N.L. Yamada, G. Liu, G.M. Veith, Role of Conductive Binder to Direct Solid–Electrolyte Interphase Formation over Silicon Anodes. Physical Chemistry Chemical Physics 21, 17356–17365 (2019).

[29] Z. Karkar, D. Guyomard, L. Roué, B. Lestriez, A Comparative Study of Polyacrylic Acid (PAA) and Carboxymethyl Cellulose (CMC) Binders for Si-Based Electrodes. Electrochimica Acta 258, 453–466 (2017).

[30] C.C. Nguyen, T. Yoon, D.M. Seo, P. Guduru, B.L. Lucht, Systematic Investigation of Binders for Silicon Anodes: Interactions of Binder with Silicon Particles and Electrolytes and Effects of Binders on Solid Electrolyte Interphase Formation. ACS Applied Materials & Interfaces 8, 12211–12220 (2016).

[31] S. Komaba, N. Yabuuchi, T. Ozeki, K. Okushi, H. Yui, K. Konno, Y. Katayama, T. Miura, Functional Binders for Reversible Lithium Intercalation into Graphite in Propylene Carbonate and Ionic Liquid Media. Journal of Power Sources 195, 6069–6074 (2010).

[32] K. Ui, D. Fujii, Y. Niwata, T. Karouji, Y. Shibata, Y. Kadoma, K. Shimada, N. Kumagai, Analysis of Solid-Electrolyte Interface Formation Reaction and Surface Feposit of Natural Graphite Negative Electrode Employing Polyacrylic Acid as a Binder. Journal of Power Sources 247, 981–990 (2014).

[33] L.M. Wheeler, N.C. Anderson, P.K.B. Palomaki, J.L. Blackburn, J.C. Johnson, N.R. Neale, Silyl Radical Abstraction in the Functionalization of Plasma-Synthesized Silicon Nanocrystals. Chem. Mater. 27, 6869–6878 (2015).

[34] M.P. Hanrahan, Y. Chen, R. Blome-Fernández, J.L. Stein, G.F. Pach, M.A.S. Adamson, N.R. Neale, B.M. Cossairt, J. Vela, A.J. Rossini, Probing the Surface Structure of Semiconductor Nanoparticles by DNP SENS with Dielectric Support Materials. J. Am. Chem. Soc. 141, 15532–15546 (2019).